ABSTRACT OF THESIS

Name of Candidate DAVID ROBERT STUART BOYD

Address PHYSICS DEPARTMENT, JCM BUILDING, MAYFIELD ROAD, EDINBURGH EH9 3JZ.

Degree DOCTOR OF PHILOSOPHY *Date* SEPTEMBER, 1973.

Title of Thesis A K^-p FORMATION EXPERIMENT.

An experiment is described to study the neutral final states produced in K^-p interactions at centre of mass energies between 1570 MeV and 1750 MeV using a 1.2 metre heavy liquid bubble chamber with a 70% γ-detection capability. Total cross-sections are presented for the $\Lambda^0\pi^0$, $\Sigma^0\pi^0$, $\Lambda^0\pi^0\pi^0$, $\Sigma^0\pi^0\pi^0$ and $\Lambda^0\eta^0$ final states together with differential cross-sections for $\Lambda^0\pi^0$ and $\Sigma^0\pi^0$. The formation of strange baryon resonances in the $\Lambda^0\pi^0$ and $\Sigma^0\pi^0$ channels is investigated by partial wave analysis. Comparisons are made with the results of previous experiments.

Use other side if necessary.

A K^-p FORMATION EXPERIMENT

Thesis

Submitted by

DAVID R.S. BOYD, B.Sc.

for the degree of

Doctor of Philosophy

University of Edinburgh

September, 1973.

A K^-p FORMATION EXPERIMENT

ABSTRACT

An experiment is described to study the neutral final states produced in K^-p interactions at centre of mass energies between 1570 MeV and 1750 MeV using a 1.2 metre heavy liquid bubble chamber with a 70% γ-detection capability. Total cross-sections are presented for the $\Lambda^0\pi^0$, $\Sigma^0\pi^0$, $\Lambda^0\pi^0\pi^0$, $\Sigma^0\pi^0\pi^0$ and $\Lambda^0\eta^0$ final states together with differential cross-sections for $\Lambda^0\pi^0$ and $\Sigma^0\pi^0$. The formation of strange baryon resonances in the $\Lambda^0\pi^0$ and $\Sigma^0\pi^0$ channels is investigated by partial wave analysis. Comparisons are made with the results of previous experiments.

CONTENTS

C O N T E N T S (Contd.)

ACKNOWLEDGEMENTS

I should like to thank Dr. D.J. Candlin for his help and for many useful discussions. My supervisor, Dr. G.R. Evans, has been a constant source of encouragement and advice and my thanks go also to Dr. A.T. Goshaw, formerly of CERN, with whom it has been both a pleasure and a most rewarding experience to work on this experiment.

Without the financial support of the Carnegie Trust for the Universities of Scotland I could not have undertaken this work and I express my gratitude to them and to Professor Feather for allowing me to use the facilities of the Physics Department. The Edinburgh contribution to this experiment was financed by a grant from the Science Research Council.

My grateful thanks are due to Mrs. Chester of the Physics Department for rapidly and accurately typing my manuscript and finally to my wife Alison for preparing many of the figures and for patiently sustaining me during the last three years.

CHAPTER I

INTRODUCTION

The Particle Data Group Tables[1] divide the elementary particles into two kinds. First those which are stable with respect to decay by the strong interaction but may decay via the electromagnetic or weak interactions, and second those which do undergo strong decay, generally known as resonances. These resonances have half-lives of the order of 10^{-23} seconds and are further subdivided into baryon and meson resonances, the former being fermions with half-integral spin while the latter are bosons and have integral spin.

Because of their extremely short lifetimes, resonances can never be observed directly and our knowledge of them must be obtained by studying their decay into particles which are stable with respect to strong decay. The properties of the resonances can then be deduced by observing the statistical effects they produce in the distribution of their decay products.

This experiment is an attempt to study some of these baryon resonances, in particular, those with strangeness quantum number -1, charge 0, total isotopic spin 0 or 1, and mass between 1570 MeV/c^2 and 1750 MeV/c^2. These are usually known as Λ and Σ resonances, the former having isospin 0 and the latter isospin 1, and are excited states of the stable $\Lambda(1116)$ and $\Sigma(1193)$ respectively.

The quantum numbers mentioned above are examples of quantities we use to classify the elementary particles and describe their interactions. By stating all its quantum

numbers, we can uniquely identify each particle among the large spectrum of particles so far discovered.

Experiments to create baryon resonances with masses below about 2 GeV/c^2 can broadly be split into two types. In the first type, called formation experiments, a baryon target is struck by a meson projectile of such a momentum that the total centre of mass energy of the baryon-meson system is equal to the rest mass of the resonance to be formed. This is an s-channel process and can be analysed using the technique known as partial wave analysis when the resonance undergoes two-body decay. The present experiment is of this kind. Alternatively, in production experiments, a higher energy meson beam is used and the resonance is produced along with other mesons.

In studying resonances, these two methods supplement each other since some quantities such as the spin and parity of a resonance may be better determined in a formation experiment, while other resonances may be so weakly coupled to the formation channel that they may in practice only be accessible through a production experiment.

The choice of beam and target particles is governed by availability and the various conservation laws which hold for the strong interaction. In our particular case, since we want to form neutral Λ and Σ resonances, a beam of K^- mesons was used with protons as targets. The ensuing K^-p system has equal amplitudes in the isospin 0 and 1 channels from SU(2),

$$|K^- p\rangle = \frac{1}{\sqrt{2}} |I_o\rangle + \frac{1}{\sqrt{2}} |I_1\rangle$$

where $|I_o\rangle$ and $|I_1\rangle$ are the isospin 0 and 1 states respectively.

The formation of Λ and Σ resonances in $K^- p$ interactions at centre of mass energies between 1570 MeV and 1750 MeV has already been extensively studied using hydrogen bubble chambers in those cases where the resonances undergo charged decay[2,3,4]. In general, the charged decay channels are a mixture of isospin 0 and isospin 1 amplitudes, and pure isospin amplitudes can only be obtained by looking at more than one channel. The channels involving neutral final states on the other hand, with the exception of the charge-exchange reaction

$$K^- p \rightarrow \overline{K^o} n,$$

are all pure isospin 0 or isospin 1. These neutral $K^- p$ reaction channels constitute the following interactions where we have indicated the isospin of each channel

$K^- p \rightarrow \Lambda^o \pi^o$	$I = 1$	(i)
$\Sigma^o \pi^o$	$I = 0$	(ii)
$\Lambda^o \pi^o \pi^o$	$I = 0$	(iii)
$\Sigma^o \pi^o \pi^o$	$I = 1$	(iv)
$\Lambda^o \pi^o \pi^o \pi^o$	$I = 1$	(v)
$\Lambda^o \eta^o$	$I = 0$	(vi)

Attempts to study the neutral final states (i) - (vi) in the

above energy range with hydrogen bubble chambers[2,3,4] have come up against the problem that the γ's produced by the decay of the Σ°, π° and η° do not interact in the chamber and so are not detected with the result that missing mass analyses must be used for channels (ii), (iii), (iv) and (v).

The missing mass distribution for the reaction

$$K^- p \rightarrow \Lambda^\circ X^\circ$$

where X° represents undetected neutral particles, is shown in Figure 1. Even with perfect resolution it can be seen that only the $\Lambda^\circ\pi^\circ$ channel can be uniquely identified. In practice, however, the $\Sigma^\circ\pi^\circ$ background in this channel can never be reduced below about 4°/o. For the other channels the problem of ambiguities is more serious, making the evaluation of even total cross-sections difficult.

The present experiment has been designed to overcome this problem by using a heavy liquid bubble chamber to enable the γ's to be detected giving well-constrained fits in all these channels. Potentially severe problems usually associated with heavy liquid experiments such as the large measurement errors due to scattering in the liquid, the background of interactions of the required types on protons in heavy nuclei and the presence in the chamber of a large number of extraneous γ's from other interactions, were all overcome by kinematical fitting and the subsequent application of cuts as we shall describe. This has allowed us to make an accurate measurement of the total cross-section for each of

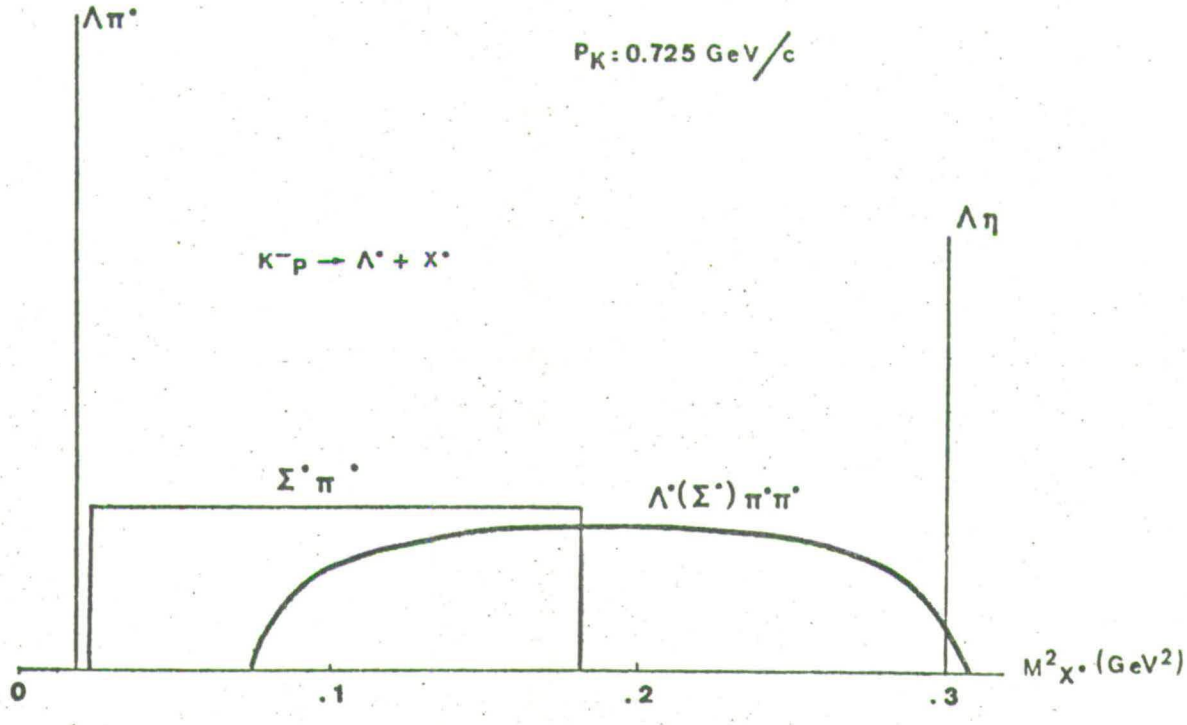

Fig. 1. Missing mass distribution for the reaction $K^-p \rightarrow \Lambda^o + X^o$ where X^o represents undetected neutral particles.

the above channels and of the differential cross-section for channels (i) and (ii). A partial wave analysis of channels (i) and (ii) has, in turn, led to a determination of the properties of the $\Lambda(1670)$, $\Lambda(1690)$, $\Lambda(1750)$, $\Sigma(1620)$, $\Sigma(1660)$ and $\Sigma(1750)$ resonances. It is hoped that we have shed some light on what several recent reviews[5] have indicated is a very confused region of baryon spectroscopy.

In Chapter II we describe the analysis of the data up to the calculation of total and differential cross-sections. This is followed in Chapter III by an explanation of the method and results of the partial wave analysis of the $\Lambda^{\circ}\pi^{\circ}$ and $\Sigma^{\circ}\pi^{\circ}$ final states.

CHAPTER II

DATA COLLECTION AND ANALYSIS

II.1 Experimental Procedure

The experiment, which was a collaboration between groups from CERN, Edinburgh, Orsay, Ecole Polytechnique, Turin and Brookhaven, involved injecting an electrostatically separated secondary beam of K^- mesons from the CERN proton synchrotron into a heavy liquid bubble chamber of diameter 1.2m and depth 1.1m containing a 50°/o propane, 50°/o freon mixture by volume. The propane supplied free protons for the K^-p interactions while the freon reduced the radiation length to 22 cm, thereby enabling us to observe the conversion of about 70°/o of the γ's produced. The typical composition of the liquid by weight was:

CF_3Br	:	0.790 ± 0.001
C_3H_8	:	0.200 ± 0.001
$C_2H_6 + C_4H_{10} + N_2$	:	0.0100 ± 0.0001

giving a working density of 0.986 ± 0.005 g.cm^{-3}.

Three runs at different beam momenta were used. The momenta, energies and number of usable exposures in each run are shown in Table 1. The range of momentum over a run was due to the energy loss by ionisation of the K^- in the liquid. The momentum spread of the beam about the nominal

Run	K^- momentum at entry window (MeV/c)	K^- momentum in fiducial volume (MeV/c)	Centre of Mass Energy (MeV)	Number of usable exposures
1	775	500 - 724	1563 - 1664	~300,000
2	870	609 - 833	1611 - 1715	~355,000
3	948	720 - 918	1662 - 1755	~300,000

TABLE 1

Beam momenta, centre of mass energies, and numbers of usable exposures in this experiment.

value was 1°/o. The analysis presented here is based on all of run 2 and half of runs 1 and 3.

Each exposure comprised three stereoscopic photographs of the chamber taken during the expansion cycle following the entry of a pulse of K^- mesons. The tracks of any charged particles present were recorded and their curvature in the 26 KG magnetic field in the chamber allowed a subsequent determination of their momenta.

These photographs were then visually scanned for events with the required topology. Each of the reactions (i) - (vi) appears in the chamber as a stopping beam track with no charged secondaries together with an associated two-prong Λ° decay

$$\Lambda^\circ \rightarrow p + \pi^-$$

where the Λ° undergoes non-leptonic charged decay, and from 2 to 6 electron-positron pairs or Compton electrons produced

by γ's from Σ^0, π^0 or η^0 decays. Where a Σ^0 is produced, this decays electromagnetically into a Λ^0 and a γ with a half-life of 10^{-14} seconds and so travels only $\sim 10^{-4}$ cm in the chamber. Similarly the π^0's decay into two γ's with half-life 10^{-16} seconds as do 38°/o of the η^0's with a half-life of less than 10^{-18} seconds. Thus, although an intermediate particle may be involved, the visible decay products will always appear to originate at the K^- interaction vertex which greatly simplifies the scanning. A typical example of the reaction

$$K^- p \rightarrow \Lambda^0 \pi^0$$

is shown in Figure 2.

Each frame with at least 1 but less than 13 entering beam tracks was given two independent scans for events occurring on an acceptable beam track with the K^- interaction vertex inside a cylindrical fiducial volume of diameter 72 cm in the centre of the chamber. An acceptable beam track was defined to be one entering the chamber through the beam window within certain angular limits and having no kinks greater than 10^0 in any view. An event recorded in both scans was accepted while an event only seen in one scan was re-examined and either verified or rejected. If accepted, such an event was then re-scanned for converted γ's so that every event passed to measurement had been subjected to two independent γ-scans.

Events were also recorded if they had the required topology

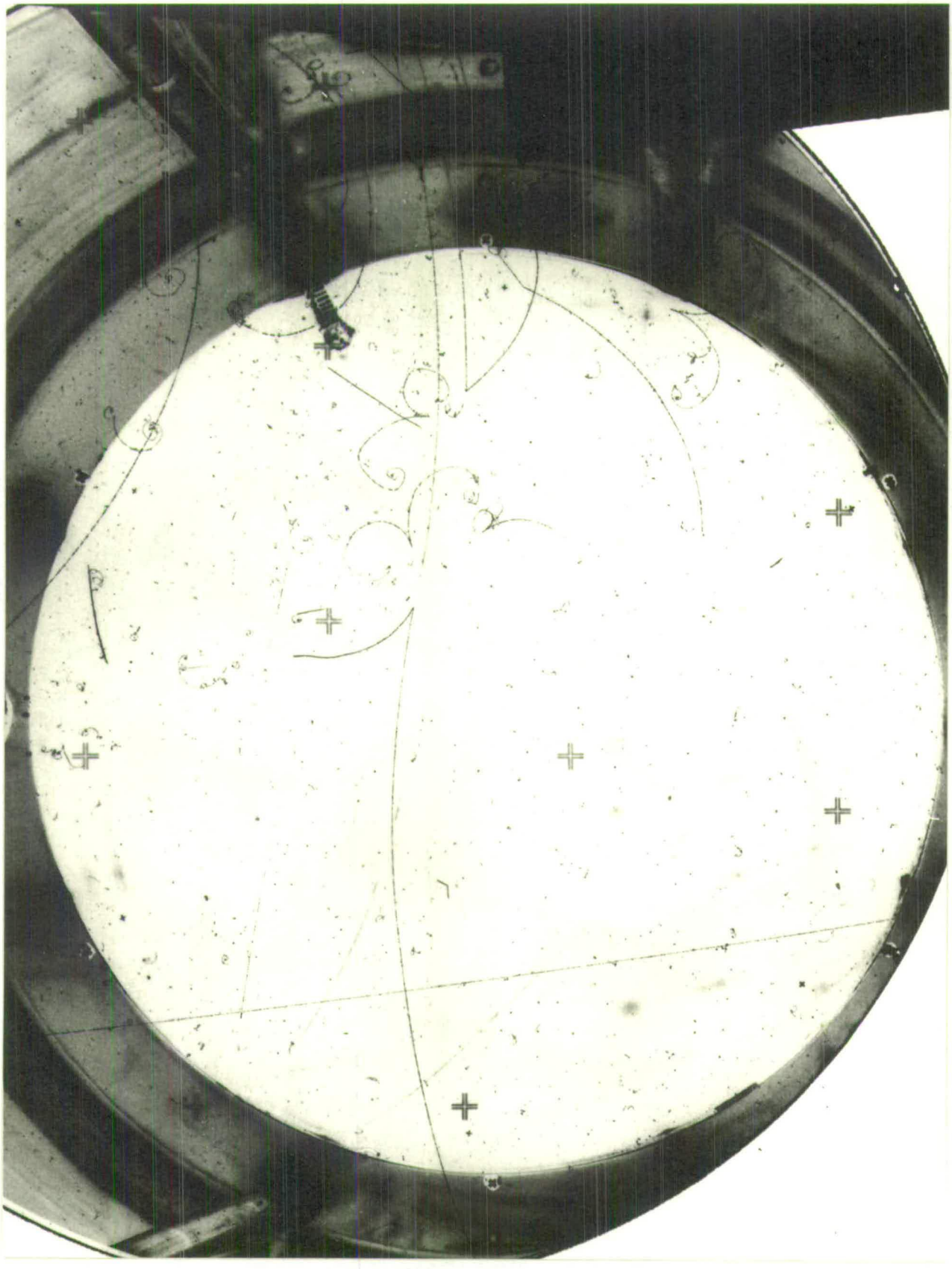

Fig. 2. An example of a $K^- p \rightarrow \Lambda^o \pi^o$ interaction.

but with a blob less than 2mm long on the scan table coming from the K^- interaction. These events were all subsequently re-examined and those in which the blob was considered to be a slow evaporation proton were rejected as being nuclear events, that is, events occurring on a bound nuclear proton. The other blob events were accepted as the blob was only a delta ray or a spurious bubble in the chamber. To check that the number of blob events accepted was reasonable, the number of blobs similar to that on the end of the track occurring elsewhere on the same beam track was counted for each blob event and the probability of getting such a blob at the end of the track calculated. This probability was compatible with the ratio of the number of blob events accepted to the number of clean events.

Events were only passed to measurement if two or more γ's were recorded for the event at scanning. This selection was made because the philosophy was adopted that a fit to a particular hypothesis would only be attempted if all the required γ's had been recorded. In other words, no missing - γ fits were tried.

The film was divided between the various laboratories of the collaboration for scanning and the events which were found were measured using the DOLL geometry system. Each laboratory then processed the measured events with the kinematics program GRIND and produced the results in the form of a Data Summary Tape (D.S.T.) containing all the successful kinematical fits on their allocation of film.

II.2 Kinematical Fitting

The first fits attempted for each event were for the two-prong decay as follows:

(a) $\Lambda^\circ \rightarrow p + \pi^-$ with Λ° origin at the K^- interaction vertex (3c fit).

(b) $\overline{K}^\circ \rightarrow \pi^+ + \pi^-$ with $\overline{K}^\circ$ origin at the K^- interaction vertex (3c fit).

(c) $\Lambda^\circ \rightarrow p + \pi^-$ without Λ° origin (1c fit).

(d) $\overline{K}^\circ \rightarrow \pi^+ + \pi^-$ without $\overline{K}^\circ$ origin (1c fit).

Both Λ° and $\overline{K}^\circ$ fits were tried because of the difficulty in distinguishing between these decays at the scanning table. The $\overline{K}^\circ$'s could be produced in the reaction

$$K^- p \rightarrow \overline{K}^\circ n \pi^\circ \ .$$

Events for which fit (a) was not successful were rejected. Of the remaining 80°/o with a successful Λ° fit (a), some also had a successful $\overline{K^\circ}$ fit. The above interaction producing a $\overline{K^\circ}$ has a relatively low cross-section indicating that these ambiguities were probably Λ°'s. Further evidence of this was obtained by studying the Λ° and $\overline{K^\circ}$ centre of mass decay angle distributions for unambiguous Λ° and $\overline{K^\circ}$ fits and for ambiguous Λ° - $\overline{K^\circ}$ fits. The centre of mass decay angle is the angle in the rest frame of the decaying particle between the directions of the decaying particle and of the outgoing positively charged particle. The ambiguous fits were found to be predominantly those in which the proton or π^+ was produced forwards in the decay

as would be expected since its momentum would then be high and the track curvature small, making identification difficult. The decay angle distributions for both unambiguous Λ° and $\overline{K^\circ}$ fits showed depletions in the forward direction and the ambiguous fits were apportioned in such a way as to make the Λ° and $\overline{K^\circ}$ distributions as flat as possible. The decay angle distribution should be exactly flat for the $\overline{K^\circ}$ and approximately flat for the Λ°. It was found by this procedure that only $1^\circ/o$ of the ambiguous fits were $\overline{K^\circ}$ and by taking all ambiguous fits as Λ°, the total contamination of $\overline{K^\circ}$ in the final sample of Λ° fits was less than $0.2^\circ/o$ and was neglected.

Fits to interactions of types (i) to (vi) were then attempted for events in which a Λ° fit (a) was successful with confidence level greater than 0.01. The input parameters to these fits were the weighted average of the theoretical and measured beam momenta, the Λ° momentum from the Λ° fit, and the measured momenta of the γ's. The energies of Compton electrons, however, poorly determined the momenta of the associated γ's and so were not used. Σ°, π° and η° mass constraints were used where appropriate. For an event recorded at scanning as having n γ's, fits were only tried to those interactions producing n γ's or less, all possible permutations of the recorded γ's being attempted for these fits. Thus the correct fit was always included among those tried for an event in which all the γ's produced in the interaction were recorded. For many events, several successful fits were achieved to

the same type of interaction using different permutations of the available γ's or to more than one type of interaction by rejecting one or more of the recorded γ's. This problem of ambiguous fits for the same event, which must be resolved if accurate cross-sections are to be calculated, is due mainly to the large measurement errors in heavy liquid and to the presence in the chamber of many extraneous γ's from other origins. We shall discuss this in more detail later.

To save time, fits to the $\Lambda^\circ \eta^\circ$ channel were only attempted in runs 2 and 3 as run 1 is below the threshold for this channel at 1664 MeV.

A record was written on the D.S.T. for each event comprising a summary of the measurement data for the event together with the fitted values of the various kinematical quantities involved for each successful fit. The D.S.T.'s produced by each laboratory were then circulated round other members of the collaboration and a study was made of the corrections necessary to take into account the various losses and biases occurring in the detection process. We shall now discuss in detail the cutting and weighting procedure applied to the fitted events on these D.S.T.'s.

The results presented here are based on an analysis of the D.S.T.'s carried out by the CERN, Edinburgh, and Turin (CET) members of the collaboration. A similar analysis was made independently by Orsay and Ecole Polytechnique. Very similar results were obtained by these two groups, which gave us confidence in the procedures adopted, the main

difference being that the French group imposed more severe cuts on the recorded γ's thereby obtaining a cleaner, but smaller, sample of accepted fitted events. In publishing the results of this experiment, it was decided to present the CET results for the $\Lambda^{o}\pi^{o}$ and $\Sigma^{o}\pi^{o}$ channels where the maximum possible number of accepted events was required to enable a partial wave analysis to be made. For the other channels, the results of the French analysis were used as these were considered to give a more effective suppression of the larger background problems in these channels.

This thesis describes the method employed in the CET analysis and therefore concentrates on the $\Lambda^{o}\pi^{o}$ and $\Sigma^{o}\pi^{o}$ channels. Results are, however, also presented for the other channels to show the agreement with the French results in the published paper[6].

II.3 Cutting and Weighting

Events were studied which had a successful 3c Λ^{o} fit with confidence level greater than 0.01 together with one or more fits at the K^{-} interaction vertex of type (i) with confidence level greater than 0.01, or types (ii) to (vi) with confidence level greater than 0.001. For the purpose of weighting, each K^{-} interaction fit was treated separately and cuts were used to exclude fits in areas where the detection process was particularly inefficient or the background high. These cuts were compensated for by weighting each accepted event with the inverse probability that the event survived all the cuts. In general, to find a suitable

value for each cut, it was increased from zero until the total weighted number of events became constant and then fixed at that value. Further weights were applied to correct for detection and processing losses of events passing the cuts. We shall now give a summary of the various cuts for the beam track, the Λ°, and the γ's, and the methods of correcting for them. The fitted values of kinematical variables were used unless otherwise stated.

II.4 Beam Track Cuts

The distributions of dip, of azimuth, and of position in the entry window of the beam tracks in fitted events were plotted and fits in the non-gaussian tails were cut. Also beam tracks suffering elastic scatters greater than 10° or scatters smaller than 10° within 10 cm of the end of the track were cut. The fraction of beam tracks surviving these cuts was parameterised as a linear function of the length of the beam track inside the chamber and a correction applied to each retained beam track during the normalization procedure as described in section II.14.

II.5 Λ° Cuts and Weights

Λ°'s which decay close to the K^{-} interaction vertex can appear as charged secondaries and may be rejected as such during scanning. To remove this area of uncertainty, all Λ°'s decaying in each of the 3 views inside an elliptical cylinder perpendicular to the scan plane with

semi-axes 0.5 cm and 0.3 cm and semi-major axis along the beam direction were cut. Similarly Λ°'s lying outside a cylindrical Λ° fiducial volume concentric with the chamber and 10 cm inside the chamber wall were cut since the scanning efficiency for Λ°'s dropped sharply very near the wall of the chamber. Further cuts removed Λ°'s with projected length of flight on the scan plane greater than 25 cm and with length of flight greater than 5 decay lengths. The decay length, λ_d, for a Λ° of momentum P_Λ is given by

$$\lambda_d = \frac{P_\Lambda \, c \, \tau}{m_\Lambda}$$

where m_Λ is the Λ° rest-mass, c is the velocity of light and τ is the mean Λ° lifetime. These last two cuts, the first of which was applied during scanning and the second during the analysis, eliminated any background of spurious Λ°'s from other origins present at large distances while removing less than 1°/o of good Λ°'s. To compensate for these length cuts, each Λ° seen to decay within the above limits was weighted by a factor

$$\frac{1}{e^{-\frac{\ell_{min}}{\lambda_t}} - e^{-\frac{\ell_{max}}{\lambda_t}}}$$

where ℓ_{min} is the distance along the Λ° line of flight from the K^- interaction vertex to the boundary of the volume common to the three elliptical cylinders described earlier,

and ℓ_{max} is the smallest of (i) the Λ° potential length to the edge of the Λ° fiducial volume, (ii) $25/\cos\delta$ where δ is the Λ° dip and (iii) $5\lambda_d$. λ_t is the total attenuation length for a Λ° of momentum P_Λ and is calculated from

$$\frac{1}{\lambda_t} = \frac{1}{\lambda_d} + \frac{1}{\lambda_i}$$

where λ_i is the interaction length for a Λ° of this momentum in the liquid. This was assumed to be the same as the interaction length for a proton of momentum P_Λ in the same liquid. This in turn is given by

$$\frac{1}{\lambda_i} = \frac{1}{\lambda_i^H} + \frac{1}{\lambda_i^C} + \frac{1}{\lambda_i^F} + \frac{1}{\lambda_i^B}$$

where λ_i^H, λ_i^C, λ_i^F, and λ_i^B are the interaction lengths for protons of this momentum in hydrogen, carbon, fluorine and bromine respectively, each of these interaction lengths being given by the inverse of the product of the density and proton cross-section for the appropriate component of the liquid. The fluorine and bromine cross-sections were obtained by scaling the cross-section for protons on carbon. The justification for the use of proton interaction lengths is given in section II.13 where this is shown to lead to the correct value for the Λ° half-life.

Since Λ°'s which interact in the liquid are almost certainly lost, we must weight those seen to decay to account for this loss. Each Λ° was therefore weighted by a factor

$$\frac{\lambda_d}{\lambda_t}$$

which is the inverse of the probability that a Λ° of momentum P_Λ will decay rather than interact.

A loss of Λ°'s with momentum less than 350 MeV/c and dip angle greater than 45° was observed in some of the data, probably because they were foreshortened and were thus easily missed by the scanners. To correct this loss where necessary, all such Λ°'s which were observed were removed and for each retained Λ° with momentum less than 350 MeV/c, the probability that a Λ° of this momentum would be cut was calculated as follows. The angle α made by the Λ° with the K^- beam direction in the laboratory frame was calculated and the Λ° direction rotated about the beam. If α was less than 45°, no loss could occur and no weight was applied to the Λ°, but if α was greater than 45°, the probability, p, that this Λ° could have a dip greater than 45° and hence be cut was

$$p = \frac{2}{\pi} \cos^{-1}\left(\frac{\cos 45^\circ}{\sin \alpha}\right)$$

and the Λ° was then weighted by a factor

$$\frac{1}{(1 - p)} \quad .$$

Λ°'s which decayed to give protons with a momentum in the laboratory frame less than 154 MeV/c or pions of momentum less than 54 MeV/c were cut since these momenta, which gave proton and pion ranges in the chamber of 0.25 cm

and 0.75 cm respectively, were the lowest that could be accurately measured. To weight for these cuts, we assumed that the distribution of cos θ, where θ is the angle between the Λ° and proton directions in the Λ° rest frame, was isotropic. This was strictly true for all Λ° polarizations in the case of the $\Lambda^\circ\pi^\circ$, $\Sigma^\circ\pi^\circ$ and $\Lambda^\circ\eta^\circ$ channels, and, in the reasonable approximation that the Λ° polarization was small, it was also true for the other channels. For Λ°'s of a given momentum, the values of cos θ corresponding to proton and pion momenta in the laboratory equal to the above cuts were calculated. Representing these by cos θ_p and cos θ_π, each Λ° not cut was weighted by

$$- \frac{2}{(\cos\theta_p - \cos\theta_\pi)}$$

which is the reciprocal of the fraction of the Λ° decay phase space not removed by these cuts.

Λ°'s decaying in such a way that the angle between the proton and pion in the laboratory frame was greater than 140° were often missed by the scanners and so were cut. To correct for this loss, the fraction, f, of the Λ° decay phase space not removed by the proton and pion momentum cuts in which the proton-pion opening angle was less than 140° was calculated for each Λ° retained, and the Λ° was given a further weight,

$$\frac{1}{f}.$$

Protons and pions from Λ° decays which interacted within a short distance of the decay were also difficult to measure and it was necessary to impose a minimum length criterion for the decay tracks. Because of the difficulty of deciding whether short protons and pions stopped or interacted in the liquid, it was decided to make these minimum lengths the same as for the low momentum cuts, namely 0.25 cm for protons and 0.75 cm for pions. Thus all Λ°'s with protons or pions shorter than these lengths were cut. The probabilities of protons and pions of momenta P_p and P_π respectively interacting beyond these cuts are

$$e^{-\frac{0.25}{\lambda_i(P_p)}} \qquad \text{and} \qquad e^{-\frac{0.75}{\lambda_i(P_\pi)}}$$

where $\lambda_i(P_p)$ and $\lambda_i(P_\pi)$ are the interaction lengths in the liquid for protons and pions of these momenta. For a Λ° of a given momentum, the probability that neither the proton nor pion would interact within these minimum lengths was calculated by integrating the product of the above probabilities over the Λ° decay phase space not removed by the proton and pion momentum and opening angle cuts. Each remaining Λ° was then weighted by the inverse of this probability.

During scanning, Λ°'s with a projected proton plus pion length on the scan table of less than 2 cm were not recorded. Since the demagnification of the scan tables was

1.8, this corresponded to a projected proton-pion length cut in the chamber of 3.6 cm. However, Λ°'s surviving all of the above cuts always had a projected proton-pion length greater than 3.6 cm, so this cut caused no additional loss of Λ°'s and no correction was necessary.

A further loss of Λ°'s was observed in the distribution of the angle ϕ where

$$\phi = \cos^{-1}\left[(\hat{Z} \times \hat{P}_{\Lambda}).(\hat{P}_{\Lambda} \times \hat{P}_{p})\right]$$

and $\hat{Z}$, $\hat{P}_{\Lambda}$, and $\hat{P}_{p}$ are unit vectors in the directions of the optic axis, the Λ°, and the Λ° decay proton in the chamber. ϕ is thus the angle between the optic axis and the decay plane of the Λ°, and should be isotropically distributed for all Λ°'s in the chamber. For Λ°'s passing all of the previous cuts with momentum less than 400 MeV/c, a significant loss was observed for $|\phi| < 5^{\circ}$ due to the apparent collinearity of the proton and pion tracks and the resulting difficulty of detection. To correct for this loss, a cut was made to remove those Λ°'s with momentum less than 400 MeV/c and $|\phi| < 5^{\circ}$, and the Λ°'s remaining in this momentum range were weighted by $\frac{90}{(90 - 5)} = 1.059$.

A final cut removed all Λ°'s with laboratory momentum less than 190 MeV/c as these had a very low probability of detection and were also strongly affected by the above cuts. They thus had very high weights which were particularly

sensitive to the exact values of the cuts. In the $\Lambda^\circ\pi^\circ$ channel, this cut removed a portion of the differential cross-section above about + 0.9, resulting in the measured cross-section for this channel being slightly low. The correction for this is described in Section II.15. Where the Λ° came from a Σ° decay, this cut removed a portion of the isotropic Σ° centre of mass decay distribution which was weighted back proportionally.

It was also necessary to eliminate Σ°'s with laboratory momentum under 190 MeV/c because the above Λ° momentum cut removed over half the decay phase space for such low momentum Σ°'s. This had an analogous effect in the $\Sigma^\circ\pi^\circ$ channel to that described above in the $\Lambda^\circ\pi^\circ$ channel and was corrected for in the same way.

Having applied and corrected for all these cuts, those Λ°'s which remained had to be weighted for losses during scanning. Each photograph was given two independent scans for Λ°'s and by counting how many Λ°'s were found in only one scan and how many were found in both scans, the double scan efficiency for Λ°'s could be calculated.

Suppose altogether N_1 Λ°'s were seen once only and N_2 were seen twice, then the average number of Λ°'s seen by one scanner was $\frac{N_1}{2} + N_2$. If ε_1 is the single scan efficiency and N_T is the total number of Λ°'s actually present, which is unknown, then we have

$$\varepsilon_1 N_T = \frac{N_1}{2} + N_2$$

and $$\varepsilon_1^2 N_T = N_2$$

giving $$\varepsilon_1 = \frac{N_2}{\frac{N_1}{2} + N_2} .$$

The double scan efficiency, ε_2, is then

$$\varepsilon_2 = 1 - (1 - \varepsilon_1)^2 .$$

The double scan efficiency for Λ°'s remaining after all of the above cuts was calculated as a function of the following variables:

(i) the Λ° momentum;

(ii) the distance from the K^- interaction to the Λ° decay;

(iii) the distance (ii) projected on the scan plane;

(iv) the total projected proton plus pion length of the Λ°;

(v) the position of the Λ° decay in the chamber,

to see if it depended strongly on any of these factors. The small variation observed was adequately represented by parameterising the double scan efficiency as a quadratic function of the Λ° momentum. The double scan efficiency was everywhere above 97°/o.

Table 2 shows the estimated average losses of Λ°'s due to the causes discussed above.

Reason for loss	Estimated fraction of Λ°'s lost
Λ° minimum length cut	0.142 ± 0.005
Λ° maximum length cut	0.013 ± 0.005
Λ° interactions	0.055 ± 0.020
Λ° dip cut	0.014 ± 0.010
p, π^- momentum and angle cuts	0.092 ± 0.010
p, π^- interactions	0.036 ± 0.010
Λ° decay plane cut	0.027 ± 0.008
Λ° scanning losses	0.014 ± 0.005

TABLE 2

Estimated fraction of Λ°'s lost due to various causes.

Finally each Λ° was weighted by a factor[1]

$$\frac{1}{0.642}$$

to account for unobservable neutral decays

$$\Lambda^\circ \rightarrow n + \pi^\circ \ .$$

As all of these cuts and losses were independent and cumulative, the total weight applied to each retained Λ° was the product of the separate weights described above. The average Λ° weight was ~ 2.3.

II.6 γ Cuts and Weights

The cuts and weights for γ's used in fits are particularly important in this experiment because they constitute a sizeable portion of the total event weight in the channels being analysed. The loss, due to these cuts, of one or more of the γ's in a fit removes that fit, but another fit not using these γ's may still be accepted for the event.

The γ's produced by the decay of Σ°'s, π°'s or η°'s could be seen if they converted to $e^{+}e^{-}$ pairs or produced Compton electrons by collision in the liquid. At the scan table, all detected $e^{+}e^{-}$ pairs with energy greater than 7 MeV, which pointed to the K^{-} interaction, were recorded, as were all detected Compton electrons with energy greater than 7 MeV and emission angle from the line of flight of the γ less than 9°. The 7 MeV cut was imposed by requiring each pair or Compton electron to be larger than a 1 cm diameter circle on the scan table.

Fitted γ's which interacted within a sphere of radius 1 cm round the K^{-} interaction were cut as their directions were very poorly determined, while those which interacted outside a cylindrical γ fiducial volume concentric with the chamber and 8 cm inside the chamber wall were removed as their detection efficiency was low.

The cut at 1 cm also removed Dalitz pairs which were not treated correctly in the kinematical fitting. This loss was corrected for using the known probabilities for Dalitz

pair production in Σ° and π° decays.

The probability of a γ of momentum P interacting beyond a distance L from the K^{-} interaction is

$$e^{-L\rho\sigma_T(P)}$$

where ρ is the liquid density and $\sigma_T(P)$ is the total cross-section in the liquid for a γ of this momentum.

Since every event was doubly scanned for γ's, we can calculate a γ double scan efficiency in the same way as for Λ°'s. The average double scan efficiency for $e^{+}e^{-}$ pairs was 97.5°/o and for Comptons was 86°/o, indicating that these two categories must be dealt with separately. The double scan efficiency for pairs and for Comptons was calculated as a function of

(i) the γ momentum,

(ii) the γ dip,

(iii) the γ azimuth,

(iv) the projected length of flight of the γ on the scan plane, and

(v) the position of the γ interaction point in the chamber.

No variation was found with (ii) or (iii) but the double scan efficiency depended significantly on the other variables. In particular, it dropped for low momentum γ's, for γ's which interacted far from the K^{-} interaction, and for γ's which interacted near the edge of the γ fiducial volume. This last effect was shown to be due primarily to γ's with long projected lengths of flight by recalculating (v) for

γ's with short projected lengths of flight in which case the double scan efficiency remained constant right up to the edge of the γ fiducial volume. The principal factors affecting the γ double scan efficiency were thus deduced to be the γ momentum and the projected length of flight of the γ. This was to be expected as these represented the size of the converted γ and its distance from the K^- interaction as seen on the scan table, the two factors most affecting the visibility of the γ to the scanner.

Pairs and Comptons were then further split into bins of momentum and projected length of flight and the double scan efficiency calculated for each bin. By doing this, the principal objection to the double scan efficiency calculation outlined earlier was overcome. This objection[7] is that the scan efficiency calculation for a group of γ's only gives the correct answer if all the γ's used in the calculation have the same <u>a priori</u> visibility to the scanner. By dividing the γ's as we have done here, we ensure that all the γ's in a particular bin will have equal visibility to the scanner and so the double scan efficiency calculated for each bin will be correct.

It was found that at large projected lengths of flight, the double scan efficiency for pairs and Comptons dropped below 75°/o and could not be calculated very precisely as there were relatively few γ's at large distances on which to base the scan efficiency calculation. In addition, there was known to be an appreciable background of spurious

recorded γ's from other origins at large distances, and for these reasons it was decided to apply a momentum-dependent cut-off to the projected length of flight distributions of both pairs and Comptons where the double scan efficiency fell below 75°/o. This was accomplished by cutting all pairs and Comptons beyond the cut-off and corrected for by setting the double scan efficiency to zero in this region.

A study of the distribution of Compton electrons as a function of their distance from the K^- interaction vertex, which will be described in Section II.12, revealed that, beyond 30 cm from the K^- interaction, there were substantially more Compton electrons than one would expect by the normal law of exponential attenuation with distance. It was therefore decided to cut all Compton electrons further than 30 cm from the K^- interaction as there was no way of distinguishing good Compton electrons from background, and the number of good Compton electrons expected beyond 30 cm was only 1.4°/o of the total number of γ's. The correction for this loss is described below.

Suppose we detect a γ with momentum P, dip δ, and projected length of flight R. If $\sigma_p(P)$ and $\sigma_c(P)$ are the cross-sections for a γ of this momentum to produce an e^+e^- pair of energy greater than 7 MeV, and a Compton electron of energy greater than 7 MeV and emission angle less than 9° respectively; and if $\varepsilon_p(P,R)$ and $\varepsilon_c(P,R)$

are the double scan efficiencies for the γ if it appears as a pair and Compton respectively, then we have the following expression for the probability that the γ was detected by the scanners

$$\frac{\rho\sigma_T(P)}{\cos\delta}\, e^{-\left(\frac{R\rho\sigma_T(P)}{\cos\delta}\right)} \left[\frac{\sigma_p(P)}{\sigma_T(P)}\,\varepsilon_p(P,R) + \frac{\sigma_c(P)}{\sigma_T(P)}\,\varepsilon_c(P,R)\right] .$$

This depends only on the vector momentum and projected length of flight of the γ and is independent of whether the γ was detected as a pair or as a Compton. For the purpose of calculating a weight for the event, however, we only want this probability in terms of the appropriate kinematical quantity, namely the γ vector momentum. Therefore, for each γ, we integrated the above probability with respect to the projected length of flight between the limits $\cos\delta$ and R_{max}, the projected potential length of the γ to the edge of the γ fiducial volume, to get the probability of detecting a γ with this momentum independent of where it converted in the chamber. To account for the Compton 30 cm length cut, the upper limit of integration of that part of the expression for the γ detection probability which gives the probability for detecting the γ as a Compton electron, was taken as the smaller of R_{max} and $30\cos\delta$. Each remaining γ was then weighted by the inverse of this total γ detection probability, giving an average γ detection weight of ~ 1.3. In calculating this weight, fitted values of parameters were used

except for the two parameters, P and R, in the scan efficiency calculation for which measured values were used. It was considered more appropriate to use measured values because these were more directly related to what the scanner actually saw than the fitted values.

A cut was imposed during the analysis to remove γ's with laboratory momentum below 30 MeV/c in an attempt to reduce the background of low energy spurious γ's unconnected with the K^- interactions which nevertheless fit as they contribute little to the energy-momentum balance at the interaction. This cut removed portions of the isotropic centre of mass decay distribution of the π^o's and was weighted for in proportion to the solid angle removed in each case.

Those γ's with a dip angle in the chamber greater than 80° were cut as they were very foreshortened and difficult to measure. This was corrected for analytically by rotating the direction vector of each γ about the beam direction and calculating the fraction, f, of this 2π angle during which the γ direction was inside the double 80° dip cones. Each γ retained was then weighted by

$$\frac{1}{(1 - f)} \quad .$$

For the vast majority of γ's, this weight was 1.0 as these did not pass through the 80° dip cones on rotation about the beam.

Each γ producing an e^+e^- pair in the chamber had

a probability of pointing to the K^- interaction vertex calculated as follows. If both electrons were measured, the dip λ, and azimuth ϕ, of the γ were calculated as

$$\lambda = \frac{\frac{\lambda_1}{(\Delta\lambda_1)^2} + \frac{\lambda_2}{(\Delta\lambda_2)^2}}{\frac{1}{(\Delta\lambda_1)^2} + \frac{1}{(\Delta\lambda_2)^2}} \quad ; \quad \phi = \frac{\frac{\phi_1}{(\Delta\phi_1)^2} + \frac{\phi_2}{(\Delta\phi_2)^2}}{\frac{1}{(\Delta\phi_1)^2} + \frac{1}{(\Delta\phi_2)^2}}$$

where λ_1, $\Delta\lambda_1$, ϕ_1, and $\Delta\phi_1$ were the measured dip, measured dip error, measured azimuth, and measured azimuth error of the first electron with λ_2, $\Delta\lambda_2$, ϕ_2, and $\Delta\phi_2$ the same for the second electron. The error in dip, $\Delta\lambda$, and in azimuth, $\Delta\phi$, of the γ were given by

$$\frac{1}{(\Delta\lambda)^2} = \frac{1}{(\Delta\lambda_1)^2} + \frac{1}{(\Delta\lambda_2)^2} \quad ; \quad \frac{1}{(\Delta\phi)^2} = \frac{1}{(\Delta\phi_1)^2} + \frac{1}{(\Delta\phi_2)^2} \, .$$

Where only one electron was measured because the other was of very low momentum or suffered severe multiple scattering, λ, $\Delta\lambda$, ϕ, and $\Delta\phi$ for the γ were taken to be equal to the same quantities for the measured electron.

Knowing the measured positions of the K^- interaction vertex and the γ conversion point, with associated errors, the dip λ', dip error $\Delta\lambda'$, azimuth ϕ', and azimuth error $\Delta\phi'$ of the γ line of flight direction were calculated.

A χ^2 of pointing of the γ to the K^- interaction

vertex was then calculated by comparing the γ directions, λ and ϕ, as calculated from the electron directions, with the γ line of flight directions λ' and ϕ', thus:

$$\chi^2 = \frac{(\lambda - \lambda')^2}{(\Delta\lambda)^2 + (\Delta\lambda')^2} + \frac{(\phi - \phi')^2}{(\Delta\phi)^2 + (\Delta\phi')^2} .$$

The confidence level for the hypothesis that the γ actually came from the K^- interaction was obtained by integrating the χ^2 probability distribution for 2 degrees of freedom between the calculated value of χ^2 and infinity. We shall refer to this confidence level, which had the form

$$e^{-\frac{\chi^2}{2}}$$

as the pointing probability for the γ. Neglecting the possibility of grossly bad measurements, so that the measured parameters should have gaussian errors, this pointing probability should be uniformly distributed between 0 and 1 for γ's which came from the K^- interactions. However, bad measurements of some electrons giving rise to non-gaussian errors would result in our obtaining a pointing probability distribution with a peak at 0, even for γ's from the K^- interactions. Because of this, it was not possible to apply a cut at low pointing probabilities to all pairs to remove those which did not come from the K^- interactions and so had a low

pointing probability as it would have been impossible to estimate how many badly measured pairs from K^- interactions were also removed by this cut. Instead, a cut on pointing probability was made at 0.005 for the subset of pairs which had two measured electrons with the alignment probability for the two electrons greater than 0.01. This alignment probability was given by the confidence level for the hypothesis that the initial directions of the two electrons were the same, which was calculated from a χ^2 of alignment defined as

$$\chi^2 = \frac{(\lambda_1 - \lambda_2)^2}{(\Delta\lambda_1)^2 + (\Delta\lambda_2)^2} + \frac{(\phi_1 - \phi_2)^2}{(\Delta\phi_1)^2 + (\Delta\phi_2)^2}$$

with 2 degrees of freedom. By demanding good alignment of the electrons, this subset of pairs should not contain badly measured electrons and so should have a flat pointing probability distribution from 0 to 1 for pairs from the K^- interactions. It was in fact found to be flat above 0.005 with a peak below this, presumably due to pairs from other origins. For this reason, the cut was made at 0.005. Those pairs for which the pointing probability test was made and which were not cut were then weighted by

$$\frac{1}{(1 - 0.005)}$$

to account for the fraction of good pairs removed by the

cut. This cut was only made for pairs in the $\Lambda^\circ\eta^\circ$, $\Lambda^\circ\pi^\circ\pi^\circ$, $\Sigma^\circ\pi^\circ\pi^\circ$, and $\Lambda^\circ\pi^\circ\pi^\circ\pi^\circ$ channels as the presence of fitted pairs not coming from the K^- interactions in the $\Lambda^\circ\pi^\circ$ and $\Sigma^\circ\pi^\circ$ channels was taken into account in the Monte Carlo analysis described in Section II.8.

Those γ's which produced Compton electrons could not be tested for pointing as the kinematics of Compton production invalidated the above pointing probability calculation.

Some of the primary γ's from the K^- interactions converting in the chamber produced bremsstrahlung which in turn converted to form more pairs and Compton electrons. In many cases these secondary γ's, which were produced mainly along the line of flight of the primary γ's, pointed well to the K^- interaction vertex and so were recorded by the scanners. They must, however, be eliminated if they are used in fits as primary γ's, and as a first stage in this process, an internal selection was made in GRIND by rejecting as a secondary any γ whose line of flight from the K^- interaction was within 0.1 radians in space of the line of flight of a γ which converted closer to the K^- interaction. Even after this cut, however, the presence of some remaining fitted secondary γ's was shown by plotting the distribution of the space angle between all combinations of two γ's for those γ's used in fits. It was found that there

was a significant peak over phase space below 0.3 radians space angle and because of this a further cut was applied to fitted γ's during the analysis exactly analogous to that in GRIND but with the cut at 0.3 radians.

As well as removing secondary γ's, for which no correction is of course necessary, this cut also removed primary γ's if they lay within 0.3 radians of another primary γ and converted further from the K^- interaction. This resulted in a loss of good events which was corrected for by a Monte Carlo calculation. Two γ's from the same π° or η° could not be within 0.3 radians of each other in the chamber at the momenta involved in this experiment. Thus the problem only arose with γ's from the decay of different particles. In each fit surviving all of the above cuts and involving more than one particle which produced a γ in its decay, the two decay angles for each such γ-producing particle were varied by Monte Carlo over the whole isotropic decay phase space allowed by previous cuts and the probability, p, of the fit being cut because two γ's came within 0.3 radians of each other was calculated. Each such fit was then weighted by a factor

$$\frac{1}{(1 - p)}$$

to correct for the effects of the cut to remove secondary γ's produced by bremsstrahlung. In the $\Sigma^\circ\pi^\circ$, $\Lambda^\circ\pi^\circ\pi^\circ$, $\Sigma^\circ\pi^\circ\pi^\circ$ and $\Lambda^\circ\pi^\circ\pi^\circ\pi^\circ$ channels, the average losses due

to this cut were 0.03, 0.08, 0.16, and 0.28 respectively.

A small additional correction was necessary to account for the possibility of cutting a primary γ in GRIND because it was within 0.1 radians of a closer spurious γ. By the term spurious γ, used here and elsewhere, we mean a γ recorded by the scanners as pointing to the K^- interaction vertex but in fact produced in another interaction somewhere else in the chamber. In practice a recorded γ was defined as spurious if it was not required in the fit finally accepted for the event. This loss was estimated for each event by transforming a cone of half-angle 0.1 radians centred on each spurious γ associated with the event into the rest frame of each decaying Σ^o, π^o, or η^o and calculating the probability that the fit would be wrongly eliminated in GRIND by the bremsstrahlung cut. The fit was weighted by the reciprocal of the probability that it would not be eliminated. In all channels, this loss was less than 0.01.

Finally, a fit was vetoed if a Dalitz pair or γ closer than 1 cm from the K^- interaction vertex was recorded by the scanners but not required in the fit as it was almost certain that the γ was really associated with the K^- interaction and so should be used in a correct fit.

II.7 Ambiguous Fits

Even after applying all these cuts, there still remained the problem of more than one successful fit for the same event. These ambiguous fits were of two types. An event could have more than one fit for the same channel by selecting different permutations of the available γ's, or an event could have fits for more than one channel by rejecting one or more of the recorded γ's.

Ambiguous fits of the first type were found to have virtually the same kinematical parameters such as centre of mass energy and scattering angle, the permuted γ's generally being of low momentum and so not materially affecting these parameters. Thus the fit with the highest confidence level was always chosen.

With ambiguities of the second type, however, the problem was more acute. The philosophy was adopted that the fit involving the fewest number of γ's was correct, the other fits being obtained by including one or more spurious γ's. This choice was shown, by the Monte Carlo analysis described in the next section, to result in the smallest background of incorrectly chosen fits. An exception to this rule was made when a fit with more γ's was five or more times more probable, in which case it was chosen.

The finally accepted fit for an event could be wrong for several reasons. The fit could be in the correct channel but use the wrong γ's, or it could be in the

wrong channel, either because it required fewer γ's than were actually produced in the interaction, or because it used additional spurious γ's.

In the next two sections we describe how the efficiency for making and selecting the correct fit, and the background of incorrectly selected fits were estimated.

II.8 Monte Carlo Analysis of the $\Lambda^0\pi^0$ and $\Sigma^0\pi^0$ Channels

As the $\Lambda^0\pi^0$ and $\Sigma^0\pi^0$ channels were of primary interest in this analysis, a detailed study was made of the processing losses and backgrounds in these channels, using events generated by a Monte Carlo technique.

The generation of $\Lambda^0\pi^0$, $\Sigma^0\pi^0$ and $\Lambda^0\pi^0\pi^0$ Monte Carlo events was based on real events with accepted fits in run 2. The beam track and K^- interaction vertex, together with any spurious γ's, were taken from a real $\Lambda^0\pi^0$ event, it having been verified that the average number of spurious γ's per event was the same for real $\Lambda^0\pi^0$ events and $\Sigma^0\pi^0$ events. Using angular distributions from hydrogen experiments for $\Lambda^0\pi^0$ and $\Sigma^0\pi^0$, and phase space for $\Lambda^0\pi^0\pi^0$, a Monte Carlo simulated interaction of the required type was produced at that point in the chamber complete with converted γ's from the decay of Σ^0's and π^0's. Only events with all γ's detected in the chamber were retained. The Monte Carlo

values of the vector momentum and position of each particle were then distorted within gaussian measurement error distributions whose widths were taken to be the same as the real errors assigned to the same particle when it appeared with similar fitted momentum and position in a real event.

The $\Lambda^{o}\pi^{o}$, $\Sigma^{o}\pi^{o}$, and $\Lambda^{o}\pi^{o}\pi^{o}$ Monte Carlo events were then passed through GRIND in the normal way, each $\Lambda^{o}\pi^{o}$ and $\Sigma^{o}\pi^{o}$ simulated event being supplemented with the spurious γ's from the real $\Lambda^{o}\pi^{o}$ event, and a D.S.T. was written in the usual format for each channel.

By basing the simulated events on real events in this way, it was ensured that the number of spurious γ's in each event was correct and that the dependence of the spurious γ distribution on position in the chamber was properly included.

These Monte Carlo D.S.T.'s were then examined with a view to measuring the efficiency for successfully fitting a $\Lambda^{o}\pi^{o}$ or $\Sigma^{o}\pi^{o}$ event with gaussian measurement errors and for subsequently selecting the correct fit over all other successful fits for the event. In addition, an estimate was obtained of the background in the sample of accepted hydrogen fits due to the selection of the wrong fit for some events, either because the correct fit failed in GRIND, or because it was subsequently rejected. We shall call this the hydrogen-fit background. No significant variation of these quantities was observed

with ω^*, the centre of mass energy of the interaction, but there was some dependence on $\cos\theta^*$, where θ^* is the centre of mass angle between the directions of the K^- and π°. The $\cos\theta^*$ range from -1 to +1 was divided into ten intervals of 0.2 and the fit efficiency and hydrogen-fit background in the $\Lambda^\circ\pi^\circ$ and $\Sigma^\circ\pi^\circ$ channels estimated for each interval. The results are therefore not dependent on the angular distributions used to generate the Monte Carlo events.

First, the set of cuts normally applied to the real events was applied to the undistorted Monte Carlo values of the kinematical variables for all of the Monte Carlo events. The number of these events, N_p, passing the cuts in a given $\cos\theta^*$ interval in each channel was noted. The cuts were then applied to the fitted values of the same variables for all the events and the normal fit selection procedure used to choose one accepted fit for each event. The events with a selected $\Lambda^\circ\pi^\circ$ or $\Sigma^\circ\pi^\circ$ fit, and a fitted value of $\cos\theta^*$ in the given range, were then examined.

It was found that, for all the events, the differences between the undistorted and fitted values of ω^* and $\cos\theta^*$ were gaussianly distributed with standard deviations of ~ 3 MeV and ~ 0.03 respectively. Thus the background in both the $\Lambda^\circ\pi^\circ$ and $\Sigma^\circ\pi^\circ$ channels of events with fitted values of ω^* and $\cos\theta^*$ seriously displaced from the undistorted values was

negligible. Next, the events in which the accepted fit was in the correct channel were examined to see if the γ's used were the correct Monte Carlo γ's or if any of these had been replaced by a spurious γ. The number of events, N_c, with a fit in the correct channel using the correct γ's in the given $\cos\theta^*$ range was noted. The efficiency for successfully fitting and subsequently selecting a fit for an event in the correct channel with the correct γ's in the given $\cos\theta^*$ interval was then $\frac{N_c}{N_p}$. This efficiency was calculated for the $\Lambda^\circ\pi^\circ$ and $\Sigma^\circ\pi^\circ$ channels in each $\cos\theta^*$ interval and accounts for the loss of events with gaussian measurement errors as a result of GRIND failures, fit confidence level cuts, and incorrect fit selection in resolving ambiguities.

The background of fits accepted in the correct channel not using the correct γ's arose from two sources: those events in which all the correct γ's were seen but the accepted fit replaced one of these with a spurious γ, and those events in which one of the correct γ's was not seen but a fit was accepted which used a spurious γ instead. The background from the first source was given by the number of Monte Carlo events with accepted fits in the correct channel which used a spurious γ. The background from the second source was determined by suppressing the correct fit if it was successful for each Monte Carlo event and observing how many fits were then accepted in

the correct channel using a spurious γ. To account for the probability of not detecting one of the correct γ's, each such accepted fit was weighted by a factor $n(\frac{1-P}{P})$, where P is the average γ detection efficiency for the channel and n is the number of ambiguous fits for that event in the correct channel using a spurious γ. The sum of these weighted background events was added to the number of background events from the first source to give the total background of this type in the $\Lambda^{\circ}\pi^{\circ}$ and $\Sigma^{\circ}\pi^{\circ}$ channels, which was then expressed as a fraction of the number of correct fits in each channel.

The next problem was to consider the background in each channel of events from other channels which, for one reason or another, were not accepted in the correct channel. There was a background of events in the $\Sigma^{\circ}\pi^{\circ}$ channel which were really $\Lambda^{\circ}\pi^{\circ}$ but had a successful $\Sigma^{\circ}\pi^{\circ}$ fit using an additional spurious γ which was finally accepted, either because there was no successful $\Lambda^{\circ}\pi^{\circ}$ fit for the event, or because it was five or more times less probable than the $\Sigma^{\circ}\pi^{\circ}$ fit. This background, which was given by the number of Monte Carlo $\Lambda^{\circ}\pi^{\circ}$ events finally accepted as $\Sigma^{\circ}\pi^{\circ}$, was first estimated as a fraction of the number of correct accepted $\Lambda^{\circ}\pi^{\circ}$ fits. This was then multiplied by the ratio of the number of real $\Lambda^{\circ}\pi^{\circ}$ events to the number of real $\Sigma^{\circ}\pi^{\circ}$ events finally accepted in the given $\cos\theta^{*}$ range in run 2, to give the background in the $\Sigma^{\circ}\pi^{\circ}$ channel from $\Lambda^{\circ}\pi^{\circ}$ as a fraction of the number of correct $\Sigma^{\circ}\pi^{\circ}$ fits.

In doing this, it was assumed that the total background from all sources in the real $\Lambda^{\circ}\pi^{\circ}$ and $\Sigma^{\circ}\pi^{\circ}$ events was proportionally the same. This assumption is correct to better than $10^{\circ}/o$, which is small compared with the statistical error on the background estimate. There is no such background in the $\Lambda^{\circ}\pi^{\circ}$ channel.

There was also a background of events in the $\Lambda^{\circ}\pi^{\circ}$ channel which were really $\Sigma^{\circ}\pi^{\circ}$ and in the $\Sigma^{\circ}\pi^{\circ}$ channel which were really $\Lambda^{\circ}\pi^{\circ}\pi^{\circ}$. These events had a successful fit in the simpler channel which did not use one of the correct γ's and by the fit selection procedure, this fit was chosen unless there was a fit in the correct channel which was give or more times more probable. This background arose both when the γ rejected to make the incorrect fit was detected and when it was not. The background when the rejected γ was detected was given simply by the number of Monte Carlo events with accepted fits rejecting one of the correct γ's. The background when the rejected γ was not detected was obtained by suppressing the correct fit, if it was successful, for each Monte Carlo event and observing how many fits were then accepted which rejected one of the correct γ's. To account for the probability of not detecting the rejected γ, each such accepted fit was then weighted by a factor $n(\frac{1-P}{P})$, where P is the average γ detection efficiency for the channel and n is the number of ambiguous fits for that event which

rejected one of the correct γ's. The backgrounds in $\Lambda^{o}\pi^{o}$ from $\Sigma^{o}\pi^{o}$ and in $\Sigma^{o}\pi^{o}$ from $\Lambda^{o}\pi^{o}\pi^{o}$ were then calculated by adding the background fits with the rejected γ detected and not detected, and were first expressed as a fraction of the number of correct $\Sigma^{o}\pi^{o}$ and $\Lambda^{o}\pi^{o}\pi^{o}$ fits respectively. To obtain the background in $\Lambda^{o}\pi^{o}$ from $\Sigma^{o}\pi^{o}$ as a fraction of the number of correct $\Lambda^{o}\pi^{o}$ fits, for example, this was then multiplied by the ratio of the number of real $\Sigma^{o}\pi^{o}$ events to the number of real $\Lambda^{o}\pi^{o}$ events finally accepted in the given $\cos\theta^{*}$ range in run 2, and similarly for the background in $\Sigma^{o}\pi^{o}$ from $\Lambda^{o}\pi^{o}\pi^{o}$. The assumption was again made that the backgrounds in the real events were proportionally the same in each channel.

All the above backgrounds were estimated in the same intervals of $\cos\theta^{*}$ as the fit efficiency, and were added together to give the total hydrogen-fit background due to incorrect fit selection in the $\Lambda^{o}\pi^{o}$ and $\Sigma^{o}\pi^{o}$ channels expressed as a fraction of the number of correct hydrogen fits in the same channel.

As the Monte Carlo events were generated with gaussian measurement errors, the fit efficiency described above does not take account of the loss of some events because of non-gaussian measurement errors resulting from such causes as undetected scatters in the heavy liquid, and measurement blunders. This loss was estimated for the $\Lambda^{o}\pi^{o}$ and $\Sigma^{o}\pi^{o}$ channels by remeasuring real events

with accepted fits in these channels in run 2 and calculating the efficiency for getting the same fit on remeasurement. This efficiency was compared with the efficiency for successfully fitting a Monte Carlo event with gaussian errors in the correct channel. The difference between these two efficiencies, the first being lower than the second, was due to the additional loss of real events during the measurement process, and the probability was then calculated that an event would not be lost because of these measurement problems. We shall call this probability the measurement efficiency. Because of the relatively small number of real events, the uncertainty in the measurement efficiency was larger than for the results obtained from the Monte Carlo analysis. The dependence of the measurement efficiency on $\cos\theta^*$ was investigated but no significant variation was observed.

Table 3 gives average values of the measurement efficiency, the fit efficiency, and the hydrogen-fit background for the $\Lambda^\circ\pi^\circ$ and $\Sigma^\circ\pi^\circ$ channels in run 2.

Channel	Measurement Efficiency	Fit Efficiency	Hydrogen-fit Background
$\Lambda^\circ\pi^\circ$	$0.97 \,^{+\,0.03}_{-\,0.05}$	0.894 ± 0.014	0.047 ± 0.008
$\Sigma^\circ\pi^\circ$	0.90 ± 0.08	0.867 ± 0.021	0.083 ± 0.015

TABLE 3

Average values of the measurement efficiency, fit efficiency and hydrogen-fit background for the $\Lambda^\circ\pi^\circ$ and $\Sigma^\circ\pi^\circ$ channels in run 2.

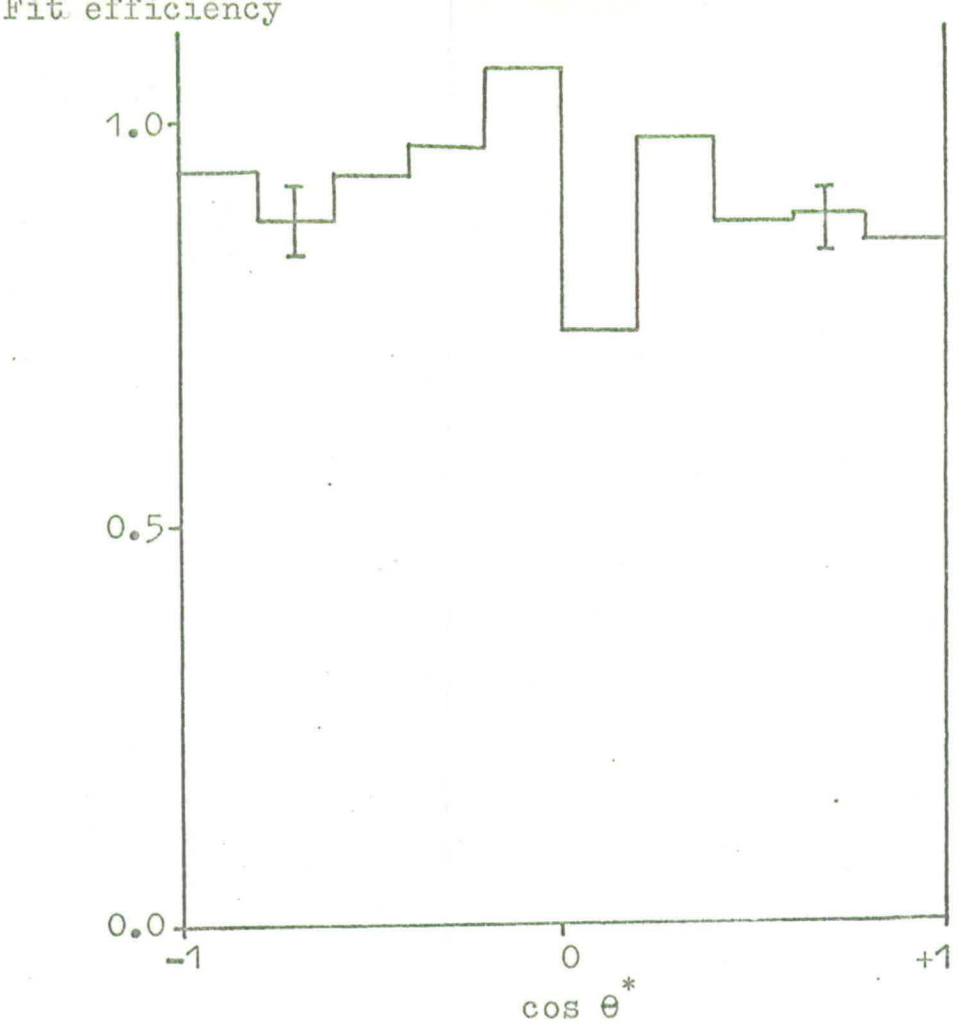

Fig. 3a. Fit efficiency for the $\Lambda^0\pi^0$ channel.

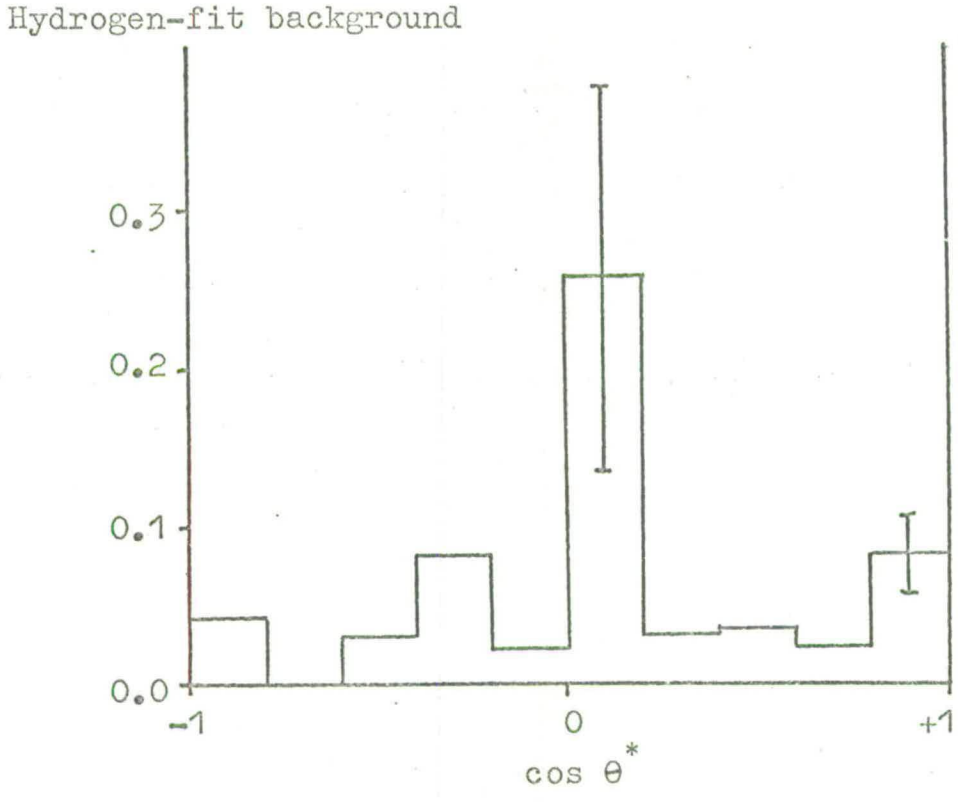

Fig. 3b. Hydrogen-fit background for the $\Lambda^0\pi^0$ channel.

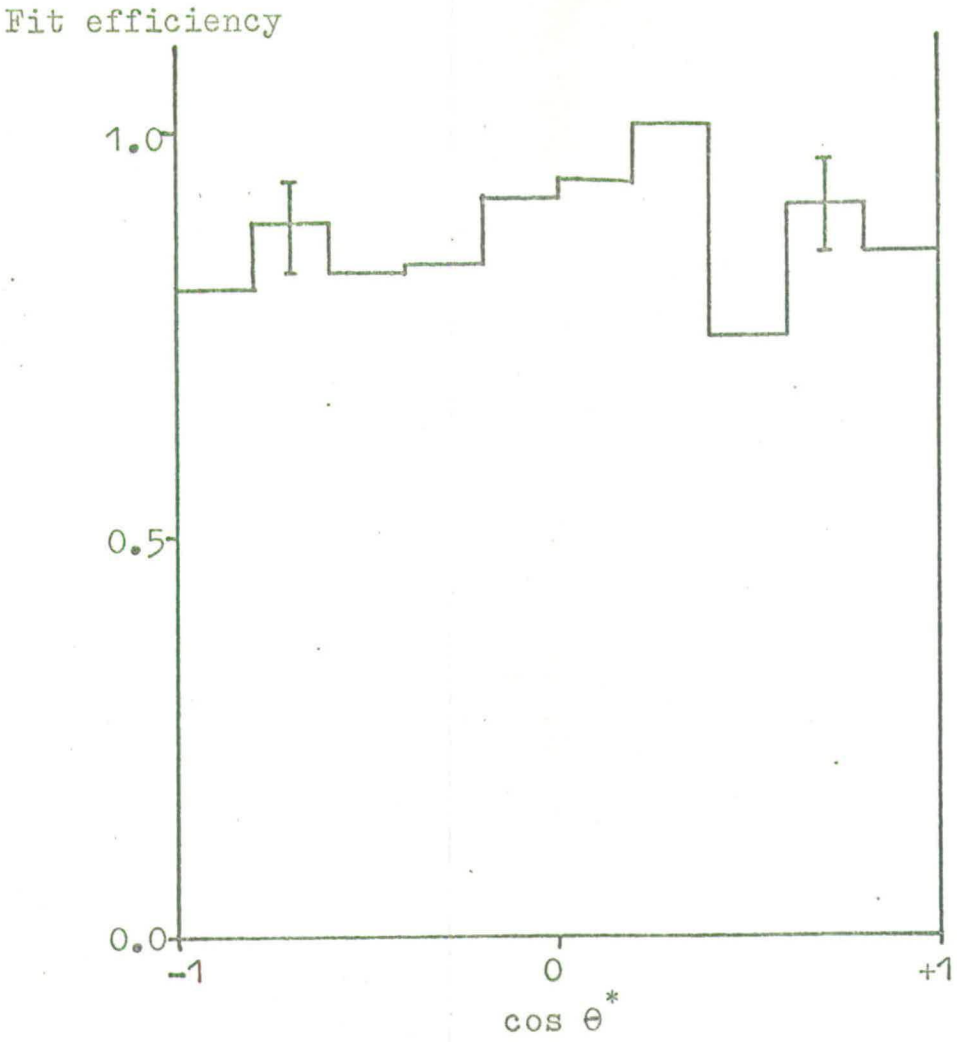

Fig. 4a. Fit efficiency for the $\Sigma^0\pi^0$ channel.

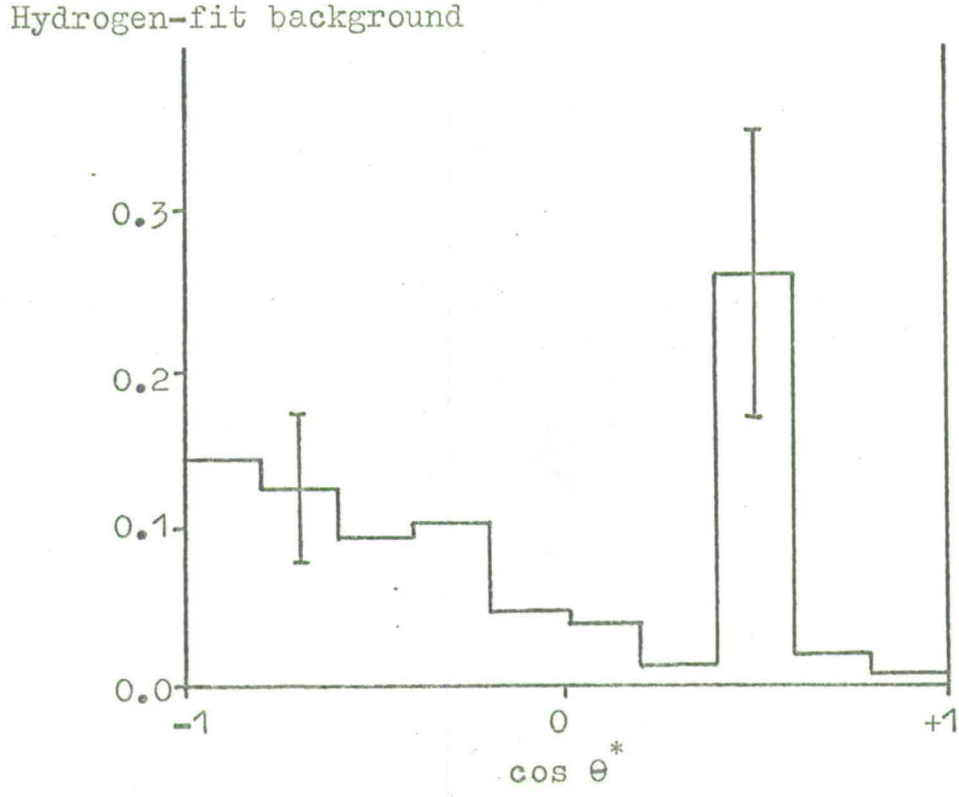

Fig. 4b. Hydrogen-fit background for the $\Sigma^0\pi^0$ channel.

The variation with $\cos\theta^*$ of the fit efficiency and the hydrogen-fit background is shown in Figures 3a and 3b for the $\Lambda^\circ\pi^\circ$ channel and in Figures 4a and 4b for the $\Sigma^\circ\pi^\circ$ channel. The only significant effect is the increase in the background towards $\cos\theta^* = -1$ in the $\Sigma^\circ\pi^\circ$ channel.

The results of the Monte Carlo analysis were recalculated for runs 1 and 3 to take into account the variation in the number of spurious γ's per event and the different ratios of the numbers of real fitted events in each channel. The measurement efficiency for these runs was estimated in the same way as for run 2.

Finally, a check was made on the accuracy with which the Monte Carlo events simulated the real events by comparing the relative number of events with ambiguous fits in different channels in the two cases. The numbers of these ambiguities were found to agree between the Monte Carlo and real events within 1.5 standard deviations in all channels, thereby confirming the results of the Monte Carlo analysis.

II.9 Remeasurement of Fitted Events

To investigate the measurement and fit efficiencies for the $\Lambda^\circ\pi^\circ\pi^\circ$, $\Sigma^\circ\pi^\circ\pi^\circ$, $\Lambda^\circ\pi^\circ\pi^\circ\pi^\circ$ and $\Lambda^\circ\eta^\circ$ channels, events with accepted fits in these channels were remeasured and refitted and the probability calculated for successfully measuring and fitting an event in each channel.

These results have a large statistical error because of the small number of events in each of these channels. They also include the effects of hydrogen-fit background as there is no way of distinguishing between correct and background fits in these channels as we were able to do with the Monte Carlo $\Lambda^\circ\pi^\circ$ and $\Sigma^\circ\pi^\circ$ events.

Table 4 gives the measurement and fit efficiencies for the $\Lambda^\circ\pi^\circ\pi^\circ$, $\Sigma^\circ\pi^\circ\pi^\circ$, $\Lambda^\circ\pi^\circ\pi^\circ\pi^\circ$ and $\Lambda^\circ\eta^\circ$ channels derived from these remeasurements.

Channel	Measurement and fit efficiency
$\Lambda^\circ\pi^\circ\pi^\circ$	0.86 ± 0.10
$\Sigma^\circ\pi^\circ\pi^\circ$	0.80 ± 0.10
$\Lambda^\circ\pi^\circ\pi^\circ\pi^\circ$	0.76 ± 0.15
$\Lambda^\circ\eta^\circ$	0.83 ± 0.10

TABLE 4

Measurement and fit efficiency for the $\Lambda^\circ\pi^\circ\pi^\circ$, $\Sigma^\circ\pi^\circ\pi^\circ$, $\Lambda^\circ\pi^\circ\pi^\circ\pi^\circ$ and $\Lambda^\circ\eta^\circ$ channels.

It was in the light of the results from the Monte Carlo analysis described in the previous section and the remeasurement of fitted events, that the fit confidence level cuts were set at 0.01 for the $\Lambda^\circ\pi^\circ$ channel and 0.001 for the other channels as mentioned in Section II.3. Because of the problems with non-gaussian measurement

errors, the fit confidence level distributions for each channel have peaks at 0 even for good fits. Thus any cut applied at low confidence levels is bound to remove proportionally more good fits than if the errors for all events were gaussian. For this reason, such a cut must be low enough not to remove too many good fits while still making an effective reduction in the hydrogen-fit and nuclear backgrounds which consist predominantly of fits with low confidence levels. The values quoted above were found to be optimum in view of these conflicting considerations. The loss of good events by these cuts is taken into account in the fit efficiencies calculated in the Monte Carlo and remeasurement analyses. The confidence level distributions for the accepted fits in each channel are shown in Section II.12. As a check that the accepted fits with confidence levels below 0.05 were not biased in a kinematical way, the distribution of these fits as a function of ω^* and $\cos\theta^*$ was examined for the $\Lambda^0\pi^0$ and $\Sigma^0\pi^0$ channels. It was found that, as expected, they were distributed in exactly the same way as the fits with confidence levels above 0.05 and no bias existed.

II.10 Nuclear Background

One of the main problems encountered in doing experiments in heavy liquid is the background of events on protons in carbon, fluorine and bromine nuclei which are indistinguishable in many cases from events on free protons. With the propane-freon mixture used in our experiment, $\sim 12^{\circ}/o$ of all K^- interactions were expected to occur on free protons and $\sim 44^{\circ}/o$ on bound nuclear protons. Of this $44^{\circ}/o$, about three-quarters should have given visible slow proton tracks which would cause the event to be rejected during scanning as described in Section II.1. Thus about $11^{\circ}/o$ of all K^- interactions would look exactly like free proton interactions but would in fact be nuclear, giving a signal to noise ratio of about 1 : 1. It was hoped that kinematical fitting, in which the target proton was constrained to be at rest, would improve this to between 10 : 1 and 20 : 1. Subsequent analysis has shown these hopes to be fulfilled.

The nuclear background remaining after fitting was due to events on protons loosely bound in the outer shells of nuclei with low Fermi momenta which fitted because of the relatively large measurement errors on charged tracks in the heavy liquid. From a kinematical point of view, these events are quite satisfactory as the protons are essentially free, but correct normalization demands that

we consider only hydrogen events.

Full details of the method used to estimate the nuclear background in the $\Lambda^{\circ}\pi^{\circ}$ and $\Sigma^{\circ}\pi^{\circ}$ channels remaining after fitting and subsequent fit selection are described elsewhere[8]. Briefly, it involved scanning for, and measuring, a sample of $K^{-}n \rightarrow \Lambda^{\circ}\pi^{-}$ and $\Sigma^{\circ}\pi^{-}$ events and then making these necessarily nuclear events simulate nuclear $K^{-}p \rightarrow \Lambda^{\circ}\pi^{\circ}$ and $\Sigma^{\circ}\pi^{\circ}$ events in GRIND to find how many fits to these free proton hypotheses we would expect to get on nuclear protons in a known sample of film. Comparison with the total number of free proton fits actually obtained by analysing the same sample of film normally allowed an estimate to be made of the magnitude of the nuclear background. For both channels this was done for different values of $\cos\theta^{*}$, where θ^{*} is the centre of mass scattering angle, but the results were consistent with an isotropic distribution of the background and an average value was therefore calculated for each channel. Because of the small number of $K^{-}n$ events which would be available to simulate the $\Lambda^{\circ}\pi^{\circ}\pi^{\circ}$, $\Sigma^{\circ}\pi^{\circ}\pi^{\circ}$, and $\Lambda^{\circ}\pi^{\circ}\pi^{\circ}\pi^{\circ}$ channels in the same way, an independent estimate of the nuclear background in these channels was obtained from a Monte Carlo analysis of $K^{-}p \rightarrow \Lambda^{\circ}\pi^{+}\pi^{-}$ and $\Sigma^{\circ}\pi^{+}\pi^{-}$ events which were scanned for on a portion of the film[9]. An average value for the background was calculated for all these three channels taken together. The nuclear background in the $\Lambda^{\circ}\eta^{\circ}$ channel was assumed to be the same as in the $\Lambda^{\circ}\pi^{\circ}$ channel. The average

values of the nuclear background in each channel expressed as a fraction of the total number of free proton fits accepted in the channel are tabulated in Table 5.

Channel	Nuclear Background
$\Lambda^\circ\pi^\circ$	0.07 ± 0.03
$\Sigma^\circ\pi^\circ$	0.09 ± 0.05
$\Lambda^\circ\pi^\circ\pi^\circ$	0.08 ± 0.05
$\Sigma^\circ\pi^\circ\pi^\circ$	0.08 ± 0.06
$\Lambda^\circ\pi^\circ\pi^\circ\pi^\circ$	0.08 ± 0.06
$\Lambda^\circ\eta^\circ$	0.07 ± 0.04

TABLE 5

Nuclear background in each channel expressed as a fraction of the number of free proton fits accepted in the channel.

II.11 Total Event Weight

Each accepted event was given a total weight which included corrections for all the losses and backgrounds described previously. Evidence that there are no important effects not being taken into account is given in the next section where various distributions for the accepted events are shown to be satisfactory.

The total weight for $\Lambda^\circ\pi^\circ$ and $\Sigma^\circ\pi^\circ$ events was obtained by multiplying the following factors for each event:

(a) the total Λ° weight,

(b) the product of all the γ weights,

(c) the weights for the Σ° and/or π° to correct for low momentum Λ° and γ cuts,

(d) the inverse of the measurement efficiency from the Monte Carlo analysis,

(e) the inverse of the fit efficiency from the Monte Carlo analysis,

(f) $\frac{1}{(1+B)}$, where B is the hydrogen-fit background from the Monte Carlo analysis expressed as a fraction of the number of correct hydrogen fits,

(g) (1-N), where N is the nuclear background expressed as a fraction of the total number of free proton fits,

(h) $\frac{1}{(1-L)}$, where L is the fractional throughput loss of events during the analysis as a result of such things as tape parity errors. This loss varied slightly between channels but averaged about 4°/o and was not biased in any kinematical way.

The total event weight for the other channels was made up in the same way except that factors (d), (e) and (f) were replaced by one factor, namely the inverse of the measurement and fit efficiency for the appropriate channel

from the remeasurement analysis.

Table 6 gives the average total event weight for each of the channels being studied.

Channel	Average event weight
$\Lambda^\circ\pi^\circ$	5.26
$\Sigma^\circ\pi^\circ$	7.78
$\Lambda^\circ\pi^\circ\pi^\circ$	12.78
$\Sigma^\circ\pi^\circ\pi^\circ$	24.01
$\Lambda^\circ\pi^\circ\pi^\circ\pi^\circ$	41.21
$\Lambda^\circ\eta^\circ$	4.49

TABLE 6

Average total event weight for each channel.

II.12 Distributions after Weighting

As a check that we were to a good approximation making the correct fit selection and weighting the events accurately, several distributions for the particles produced were plotted for all accepted events and compared with theoretical predictions. The agreement with theory was good. This sample comprised approximately three-quarters of all the data eventually to be available in the experiment.

In doing this, use was made of what we shall call Q-distributions. Suppose some parameter x has a known probability distribution $P(x)$ and has an observable range bounded by x_{min} and x_{max}. The normalized probability distribution of x is given by

$$P_n(x) = \frac{P(x)}{\int_{x_{min}}^{x_{max}} P(x)dx} .$$

We define the Q-distribution of x by

$$Q(x) = \int_{x_{min}}^{x} P_n(x')dx' .$$

It can be seen immediately that for any given probability distribution $P(x)$, $Q(x)$ is uniformly distributed between 0 and 1. This fact allows us to compare very easily any distribution of the real events with the corresponding theoretical distribution. If the real events do in fact behave as theory predicts, the corresponding Q-distribution should be flat.

First, the length distributions for the Λ^o's and γ's were examined. For these, $P(x)$ is the normal law of exponential attenuation with distance from the K^- interaction using the appropriate attenuation length with, in the case of the γ's, an additional factor for the scanning efficiency which varied with distance. The limits

x_{min} and x_{max} are the minimum and maximum length cuts for each particular particle. Figure 5 shows the Q-distribution of length for the Λ°'s in fitted events, while Figures 6a and 6b show the same separately for those fitted γ's which were scanned as pairs and Comptons. In these last two distributions the appropriate values of x_{min} and x_{max} were used depending on whether the γ was a pair or a Compton. These distributions are all reasonably flat, indicating that there are no unknown length-dependent losses of Λ°'s or γ's. It was from the Q-distribution of length for fitted Comptons that the 30 cm length cut for Comptons was found necessary to remove a pronounced peak towards $Q = 1$. As an indication of the success with which our fit selection procedure chooses the fit with the correct γ's for each event, we show in Figures 7a and 7b the Q-distributions of length corresponding to Figures 6a and 6b for those spurious γ's recorded by the scanners as associated with events with an accepted fit but rejected by the chosen fit as not coming from the K^- interaction. These spurious γ's are approximately isotropically distributed in the chamber, which explains the rising distribution with increasing Q.

Next, the angular distributions of the decays of particles produced in the K^- interaction were studied. As mentioned earlier in Section II.5, the distribution of $\cos\theta$, where θ is the angle between the directions of

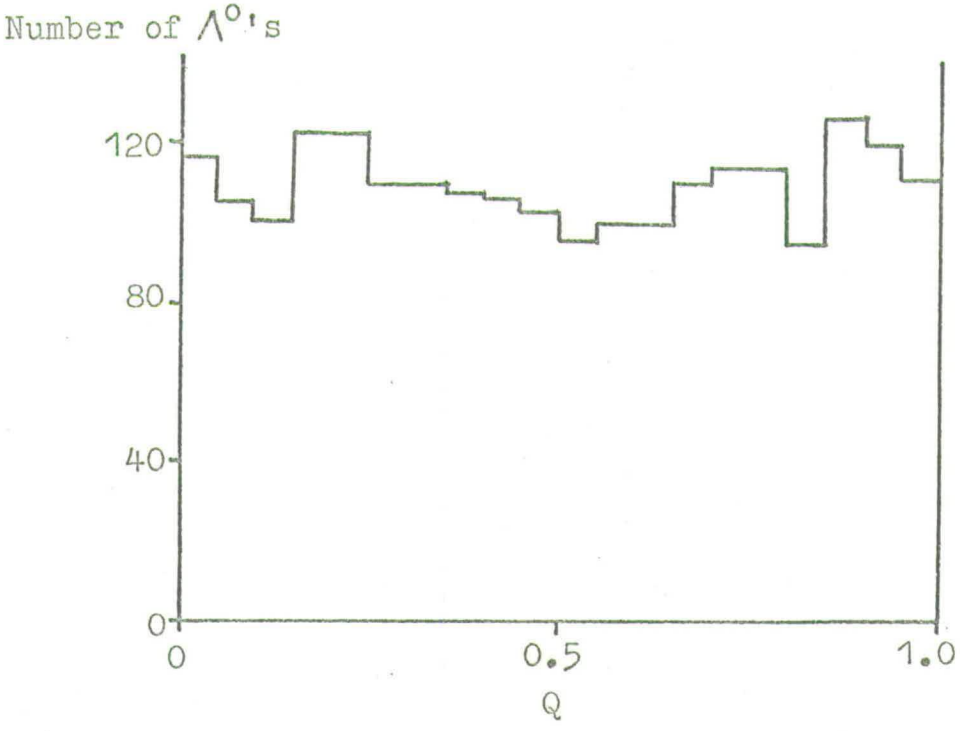

Fig. 5. Q-distribution of length for Λ°'s.

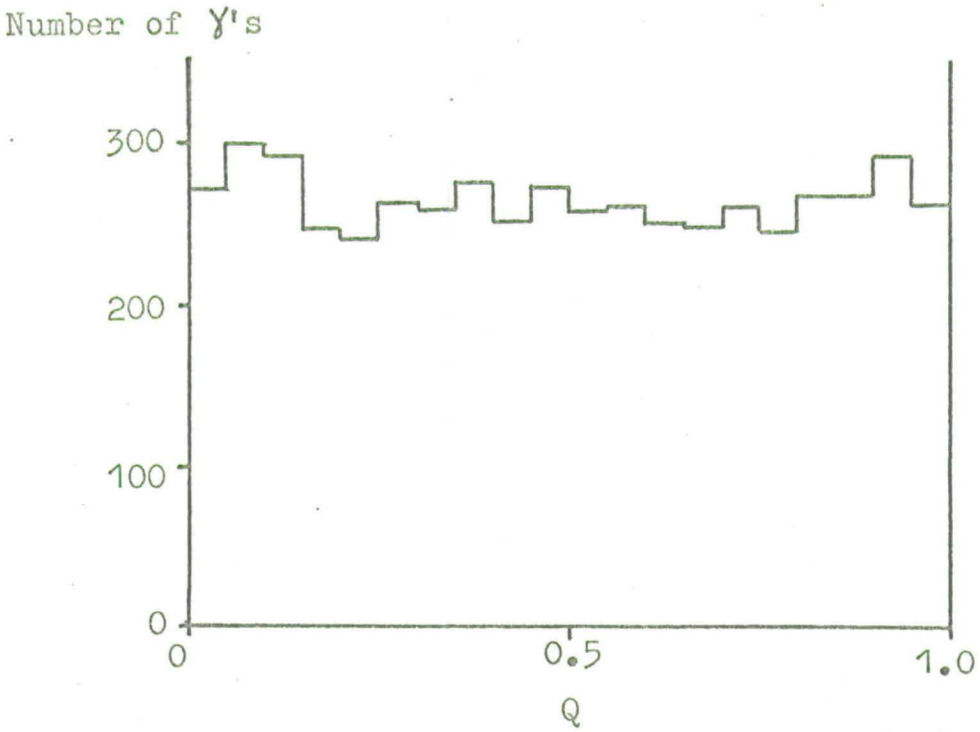

Fig. 6a. Q-distribution of length for fitted pairs.

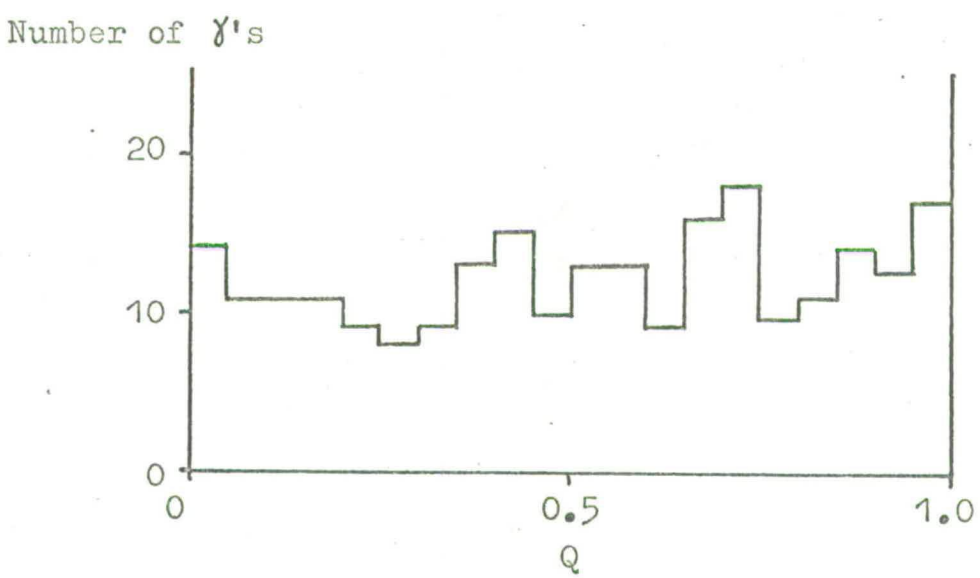

Fig. 6b. Q-distribution of length for fitted Comptons.

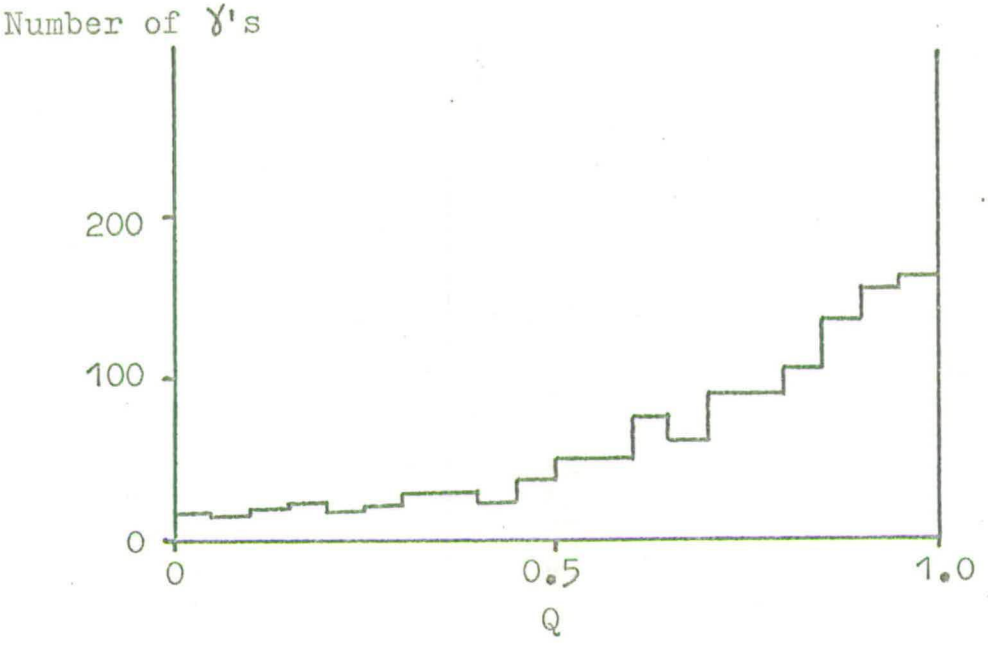

Fig. 7a. Q-distribution of length for spurious pairs.

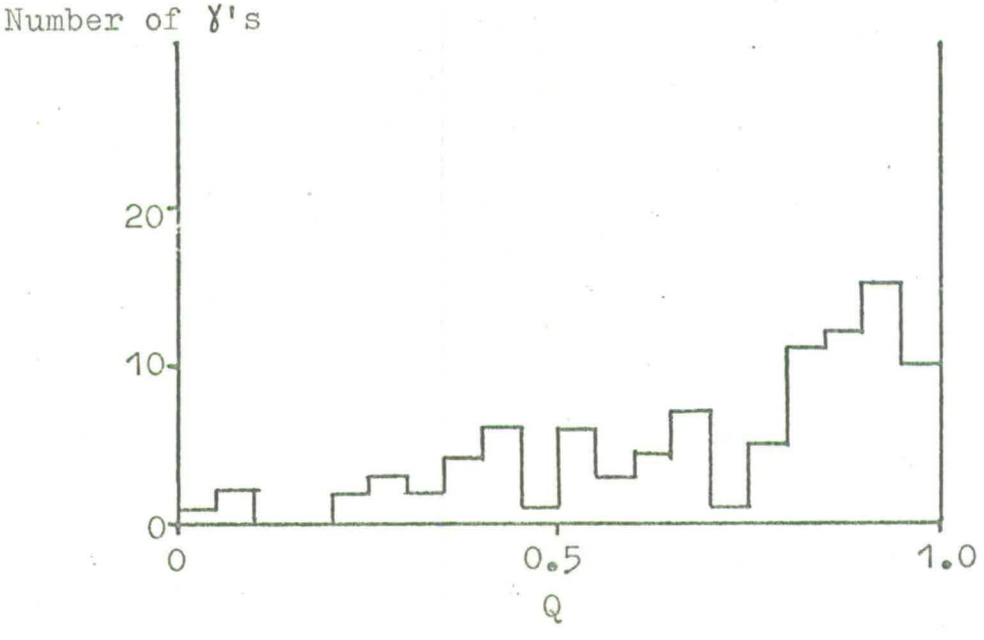

Fig. 7b. Q-distribution of length for spurious Comptons.

the Λ° and of the proton in the Λ° rest frame, should be isotropic. However, account must be taken of the minimum proton and pion momentum cuts and of the opening angle cut which remove a portion of the cos θ distribution for each Λ° decay. This was done by plotting a Q-distribution of cos θ for the Λ° decays in fitted events assuming an isotropic theoretical probability distribution with limits given by the values of cos θ corresponding to these cuts for each Λ°. This Q-distribution is shown in Figure 8 and is flat, verifying that we are correctly accounting for all Λ° decay losses.

The same decay distribution for the Σ° should also be isotropic by virtue of parity conservation in its electromagnetic decay and the Q-distribution of cos θ, where θ is the angle between the directions of the Σ° and of the Λ° in the Σ° rest frame, is shown in Figure 9 for the Σ° decays in fitted events. The limits of cos θ for each Σ° decay are given by the 190 MeV/c Λ° momentum cut and the 30 MeV/c γ momentum cut. Again this distribution is approximately flat.

Similarly Figure 10 shows the Q-distribution of cos θ for the π° decays in fitted events where θ is the angle in the π° rest frame between the directions of the π° and of one of the γ's and has limits imposed for each decay by the 30 MeV/c γ momentum cut. This distribution should be isotropic by parity conservation,

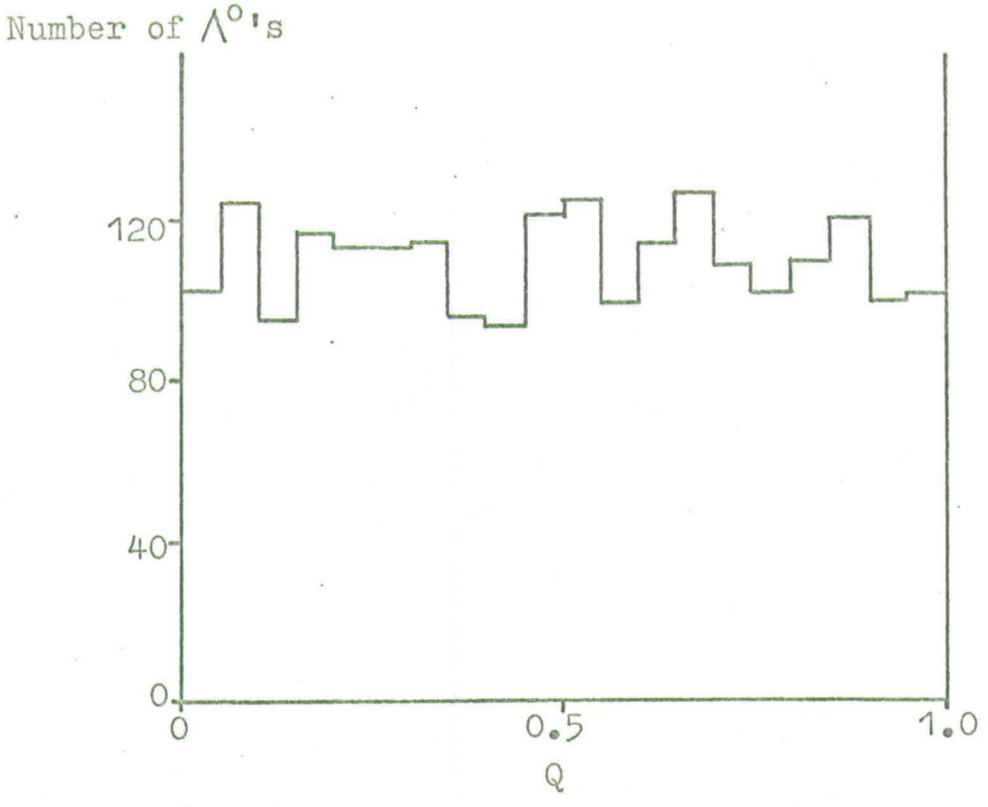

Fig. 8. Q-distribution of cos θ for Λ^0's.

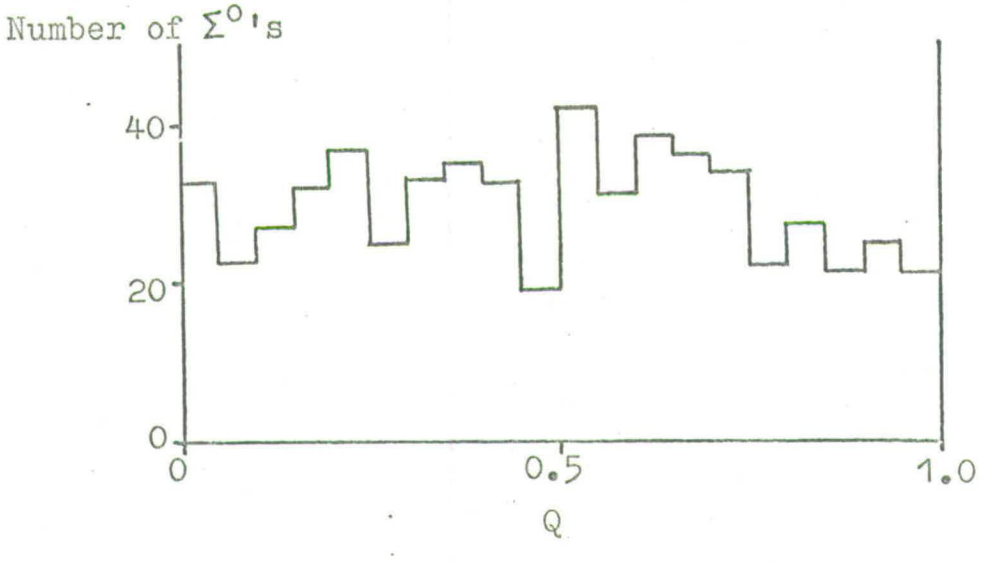

Fig. 9. Q-distribution of cos θ for Σ^0's.

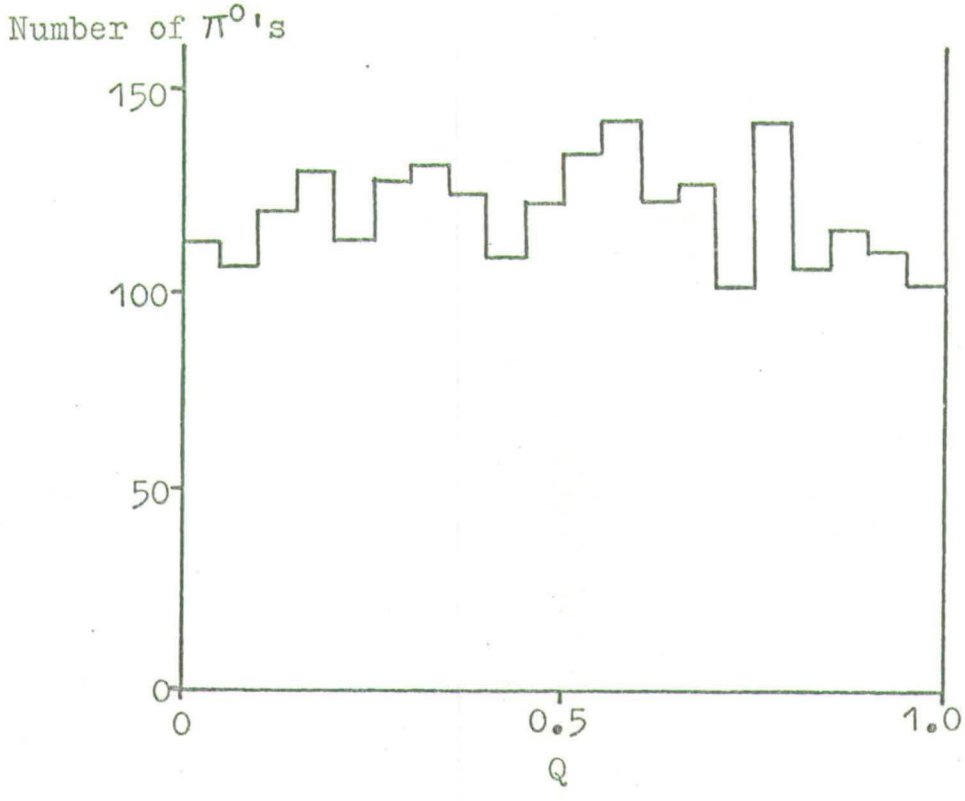

Fig. 10. Q-distribution of cos θ for π^0's.

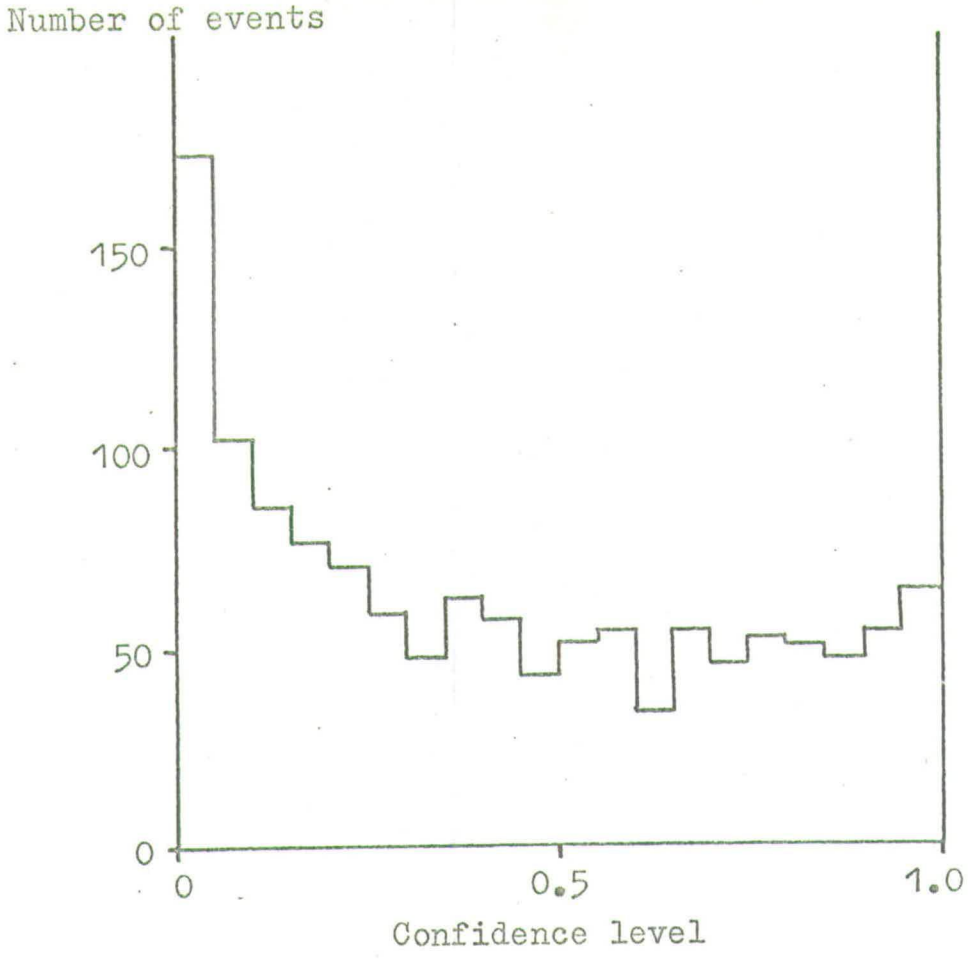

Fig. 11a. Fit confidence levels for the $\Lambda^{o}\pi^{o}$ channel.

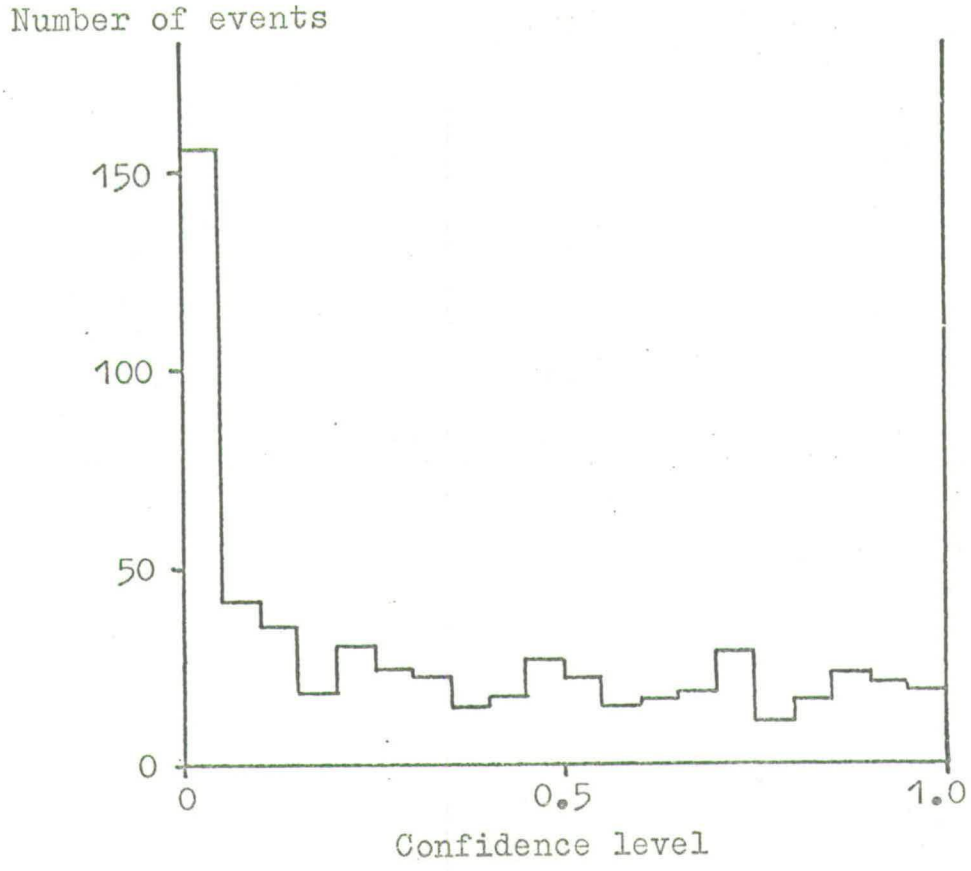

Fig. 11b. Fit confidence levels for the $\Sigma^{o}\pi^{o}$ channel.

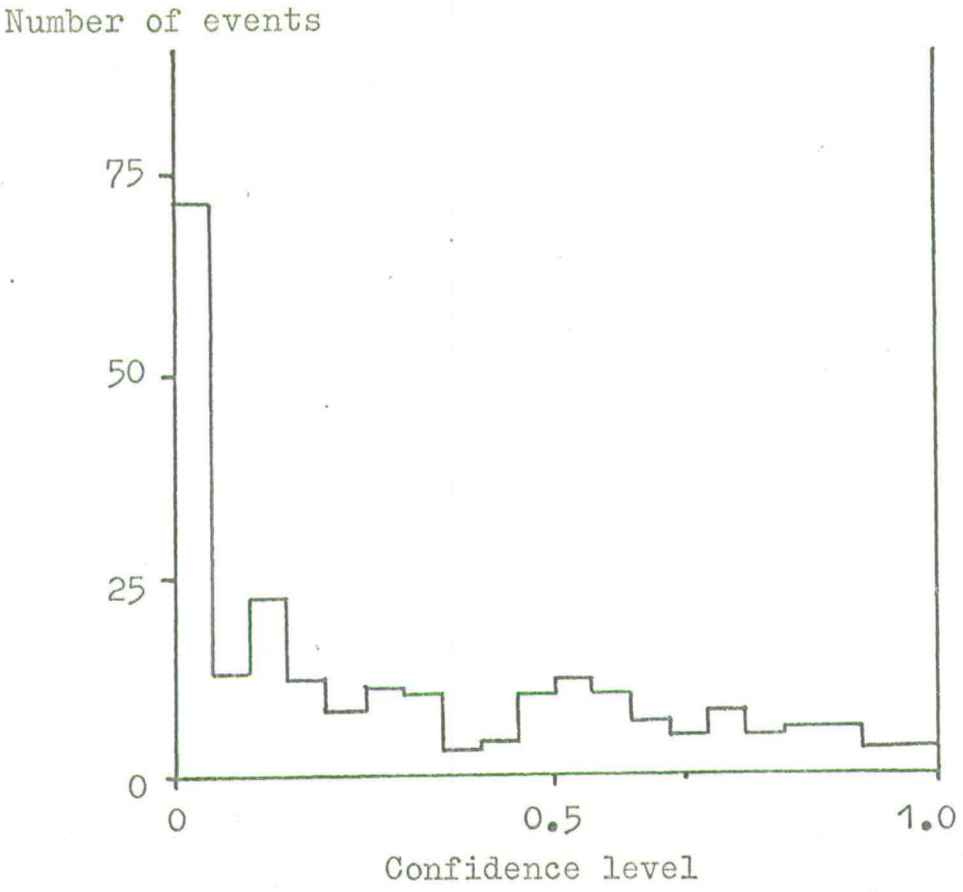

Fig. 11c. Fit confidence levels for the $\Lambda^{o}\pi^{o}\pi^{o}$ channel.

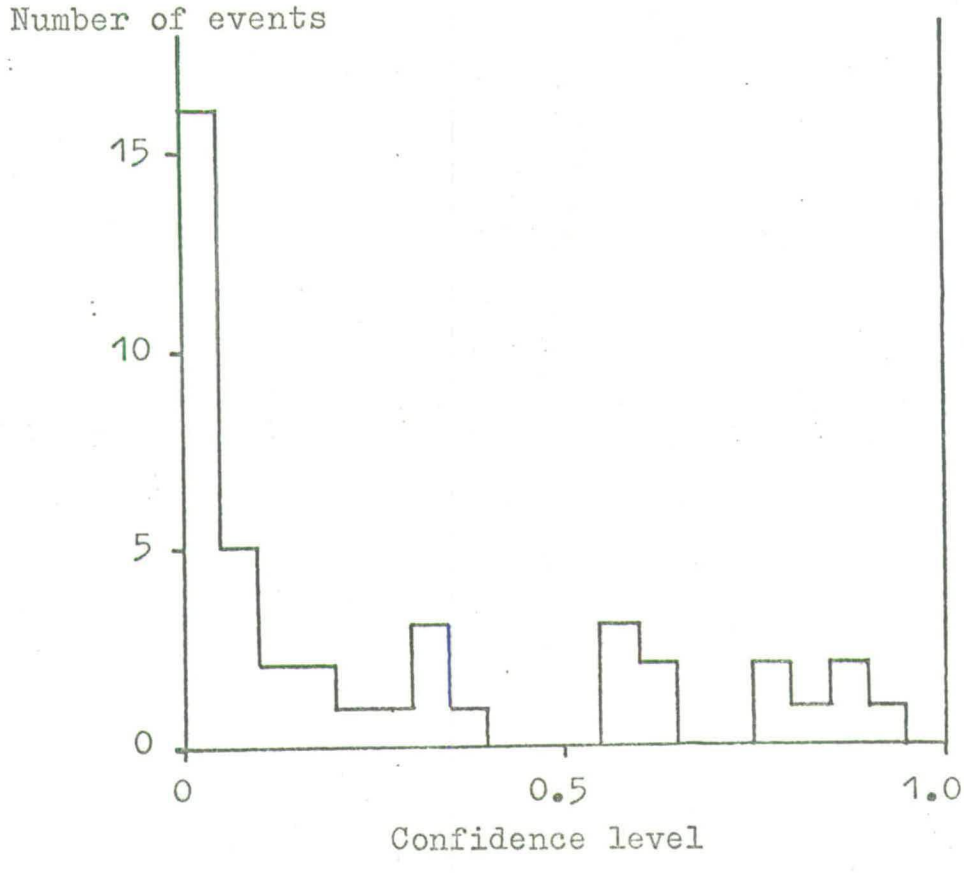

Fig. 11d. Fit confidence levels for the $\Sigma^{o}\pi^{o}\pi^{o}$ channel.

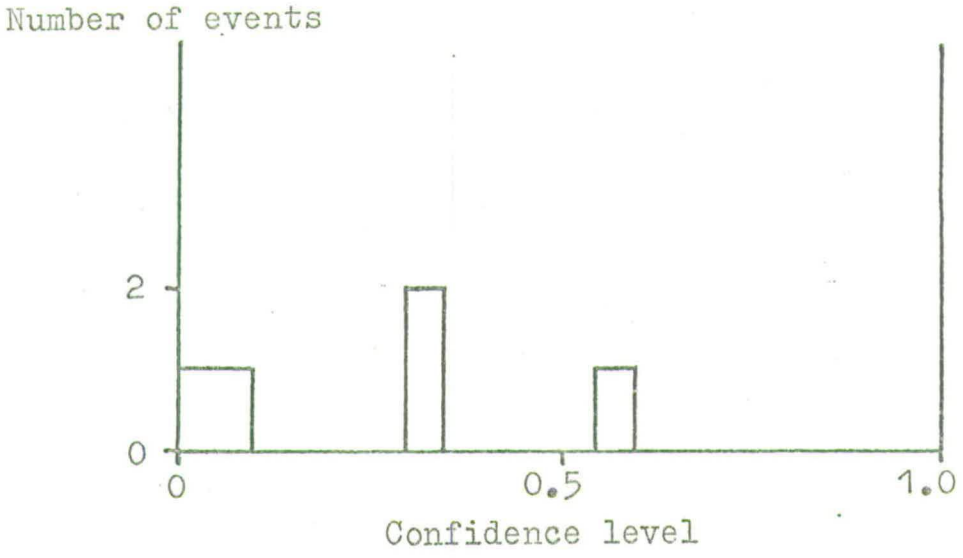

Fig. 11e. Fit confidence levels for the $\Lambda^{o}\pi^{o}\pi^{o}\pi^{o}$ channel.

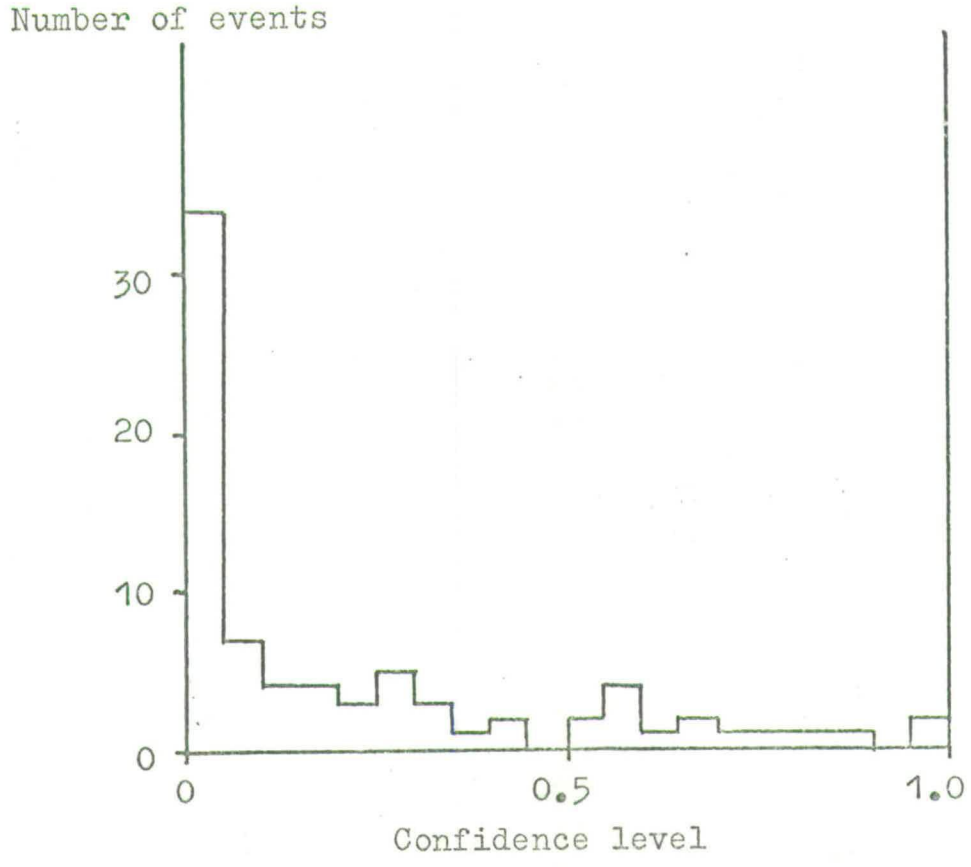

Fig. 11f. Fit confidence levels for the $\Lambda^{o}\eta^{o}$ channel.

as indeed it is.

The agreement of all of these distributions with theoretical expectations is evidence that we have made a correct selection of fitted events and that we understand how to weight these events to account for the losses in the data.

Finally Figures 11a to 11f show the fit confidence level distributions for the accepted events in each channel. These all have a peak at low confidence levels due to the non-gaussian tails in the measurement error distributions and to the remaining hydrogen and nuclear background events as mentioned in Section II.9.

II.13 Measurement of the Λ° Lifetime

A further check on the purity of the data was afforded by a measurement of the half-life of the Λ° for the decay $\Lambda^\circ \rightarrow p + \pi^-$. 1800 Λ°'s from accepted events in runs 1 and 2 were used to obtain a maximum likelihood estimate for the Λ° half-life by taking the normalized probability, P(t), of each Λ° decaying after a time t, between the limits t_{min} and t_{max}, as

$$P(t) = \frac{e^{-\frac{t}{\tau_t}}}{\tau_t \left[e^{-\frac{t_{min}}{\tau_t}} - e^{-\frac{t_{max}}{\tau_t}} \right]}$$

where

$$\frac{1}{\tau_t} = \frac{1}{\tau_d} + \frac{1}{\tau_i} \quad .$$

These times are related to the lengths defined for each Λ° in Section II.5 by the relations

$$\tau_t = a\lambda_t$$

$$\tau_i = a\lambda_i$$

$$t_{min} = a\ell_{min}$$

$$t_{max} = a\ell_{max}$$

$$t = a\ell$$

where ℓ is the distance travelled by the Λ° in the chamber before it decayed and

$$a = \frac{m_\Lambda}{P_\Lambda c} \quad .$$

m_Λ is the Λ° mass, P_Λ is the fitted Λ° momentum, and c is the velocity of light. The only independent parameter was τ_d, the half-life of the Λ° for the decay $\Lambda^\circ \rightarrow p + \pi^-$.

The results of this analysis, which was carried out for all the Λ°'s together and for the Λ°'s in three momentum ranges separately, are presented in Table 7 together with the present world average[1]. Also shown is the result of an analysis in which the interactions of the Λ°'s in the liquid were ignored by setting $\tau_t = \tau_d$ for all Λ°'s. This gave a result over one standard

deviation below the world average whereas the Λ° lifetime obtained by including the correction for interactions was in excellent agreement, thereby justifying a posteriori the assumptions made in correcting for the interactions of Λ°'s in the heavy liquid.

Sample of Λ°'s Used	Measured Λ° Lifetime
1817 Λ°, $P_\Lambda \geq 0.190$ GeV/c	$(2.522 \pm 0.068) \times 10^{-10}$ sec
598 Λ°, $0.190 \leq P_\Lambda \leq 0.475$ GeV/c	$(2.54 \pm 0.12) \times 10^{-10}$ sec
613 Λ°, $0.475 < P_\Lambda \leq 0.770$ GeV/c	$(2.50 \pm 0.12) \times 10^{-10}$ sec
606 Λ°, $P_\Lambda > 0.770$ GeV/c	$(2.53 \pm 0.12) \times 10^{-10}$ sec
1817 Λ°, ignoring Λ° interactions	$(2.438 \pm 0.064) \times 10^{-10}$ sec
World average[1]	$(2.521 \pm 0.021) \times 10^{-10}$ sec

TABLE 7

Measurements of the Λ° lifetime.

II.14 Normalization

To calculate the cross-section for any reaction it is necessary to divide the weighted number of events by a normalization factor which takes into account the available beam track density and the target density in the chamber. We shall now describe how this normalization or "flux" factor was obtained in our experiment.

The customary technique of normalizing to the number of tau decays was difficult to apply in our case because of the background in the chamber of 3-prong interactions, so a method based on a direct beam count was used. First we needed to know the density of acceptable K^- beam tracks at a given position in the chamber. This was obtained by measuring the total incoming beam flux at the entry window of the chamber and calculating the various attenuations of the beam which occurred subsequently. All photographs having between 1 and 12 acceptable incoming beam tracks were scanned for events and the number of acceptable beam tracks was counted on every photograph on which an event was found. The total acceptable incoming beam flux was then found by multiplying N_T, the total number of photographs scanned, by $\langle n \rangle$, the average number of acceptable beam tracks per photograph scanned. The method used to calculate $\langle n \rangle$ from the beam track count on photographs with an event is described in the Appendix. By counting the beam tracks during normal scanning we ensured that the same criteria were used to define

an acceptable beam track in the search for events and in the normalization procedure. As a check, however, the number of acceptable beam tracks on every 20th photograph on 37 rolls of film were subsequently counted and an independent calculation of $\langle n \rangle$ made. The results of the two methods were in very good agreement and a typical value of $\langle n \rangle$ in run 2 was

$$\langle n \rangle = 7.42 \pm 0.06 .$$

We then had to reduce this total incoming flux because of the contamination of the beam by π^- and μ^-. To estimate the percentages of π^- and μ^- in the beam, about 20°/o of the film was rescanned for δ-rays of energy greater than 6 MeV occurring on acceptable beam tracks. As the maximum δ-ray energy produceable by K^- in our momentum range was 4 MeV, the tracks with δ-rays were necessarily π^- or μ^-. Each beam track was coded as either interacting or leaving which allowed us to differentiate between K^- and π^-, which could interact, and μ^-, which did not. A detailed description of the way in which this data was fitted to the theoretical distributions of these quantities is described elsewhere[8]. Another parameter measured in this analysis was the attenuation length of the K^- in the chamber due to loss by interactions or decays. Because of the energy loss of the K^- in heavy liquid, the total cross-section and hence the attenuation length of the beam varied across

the chamber but at a given beam momentum setting, this variation was less than 1.5°/o and was neglected. Results for run 2 were

$$\text{Fraction of } K^-,\ f_K = 84.1 \pm 1.0\ °/o$$

$$\text{Fraction of } \pi^-,\ f_\pi = 4.5 \pm 1.0\ °/o$$

$$\text{Fraction of } \mu^-,\ f_\mu = 11.4 \pm 1.4\ °/o$$

$$K^- \text{ attenuation length, } \lambda_K = 82.5 \pm 1.2 \text{ cm.}$$

The attenuation of the K^- beam by interactions and decays was then accounted for by a factor

$$e^{-\frac{L}{\lambda_K}}$$

which gives the fraction of the beam remaining after a distance L in the chamber.

The final loss of K^- was as a result of the cuts on beam tracks during the analysis as described in Section II.4. The fraction, $f(L)$, of K^- surviving these cuts was parameterised as a function of the beam length L in the chamber.

Thus the number of good K^- beam tracks passing cuts at a distance L along the beam from the entry window was

$$N(L) = N_T \cdot \langle n \rangle \cdot f_K \cdot e^{-\frac{L}{\lambda_K}} \cdot f(L) \ .$$

We would, however, like the flux factor for each event to be a function of ω^*, the centre of mass energy of the K^-p interaction, rather than L, the length of the beam

track from the entry window, as ω^* is a more meaningful parameter when discussing cross-sections. In the approximation that the beam has a unique momentum at the entry window, the conversion from L to ω^* is trivial, but in our experiment this was not strictly true for two reasons. The beam had a spread in momentum of 1°/o about the central value, and this central value varied over the entrance window. These effects had to be taken into account in calculating $N(\omega^*)$, the number of good beam tracks available to give a centre of mass energy of ω^* in a K^-p interaction. For a given value of ω^*, each beam momentum P at the entry window corresponded to a beam length L in the chamber, so that

$$N(L) \equiv N(P, \omega^*)$$

where $N(P,\omega^*)$ is the number of good beam tracks as a function of the beam momentum at the entry window for a given centre of mass energy. The spread in beam momentum could be described by an experimental beam density function $D(P, y, z)$ which gave the distribution of available beam tracks as a function of the beam momentum, P, and the chamber coordinates, y and z, of the entry position of the beam track in the window. $N(\omega^*)$ was then given by

$$N(\omega^*) = \frac{\iiint N(P,\omega^*)D(P,y,z)\,dP\,dy\,dz}{\iiint D(P,y,z)\,dP\,dy\,dz}$$

where the integrals were over the whole available beam

momentum range and over the spatial limits of the entry window. The limits of the fiducial volume for accepting interactions during scanning were imposed by setting $N(P,\omega^*) = 0$ where the corresponding value of L put the interaction point outside this fiducial volume.

The flux factor, $F(\omega^*)$, for each event in units of events mb^{-1} MeV^{-1} was then given by

$$F(\omega^*) = N(\omega^*)\rho \frac{dL}{d\omega^*}$$

where ρ is the density of free protons in the liquid, $\sim(2.2 \pm 0.06) \times 10^{-5}$ mb^{-1} cm^{-1}, and $\frac{dL}{d\omega^*}$ is evaluated at the centre of mass energy of the event. The error in $F(\omega^*)$ was approximately 5%.

The average cross-section, $\bar{\sigma}$, in millibarns, over a centre of mass energy range from ω_1^* to ω_2^* could then be calculated by adding the contributions from each event thus

$$\bar{\sigma} = \sum_{i=1}^{n} \frac{W_i}{(\omega_2^* - \omega_1^*)F(\omega_i^*)}$$

where ω_i^* and W_i are the centre of mass energy and weight respectively of the i-th event and n is the number of events in the energy range.

The flux factor gives a good indication of the power of the experiment as it indicates how many events to expect

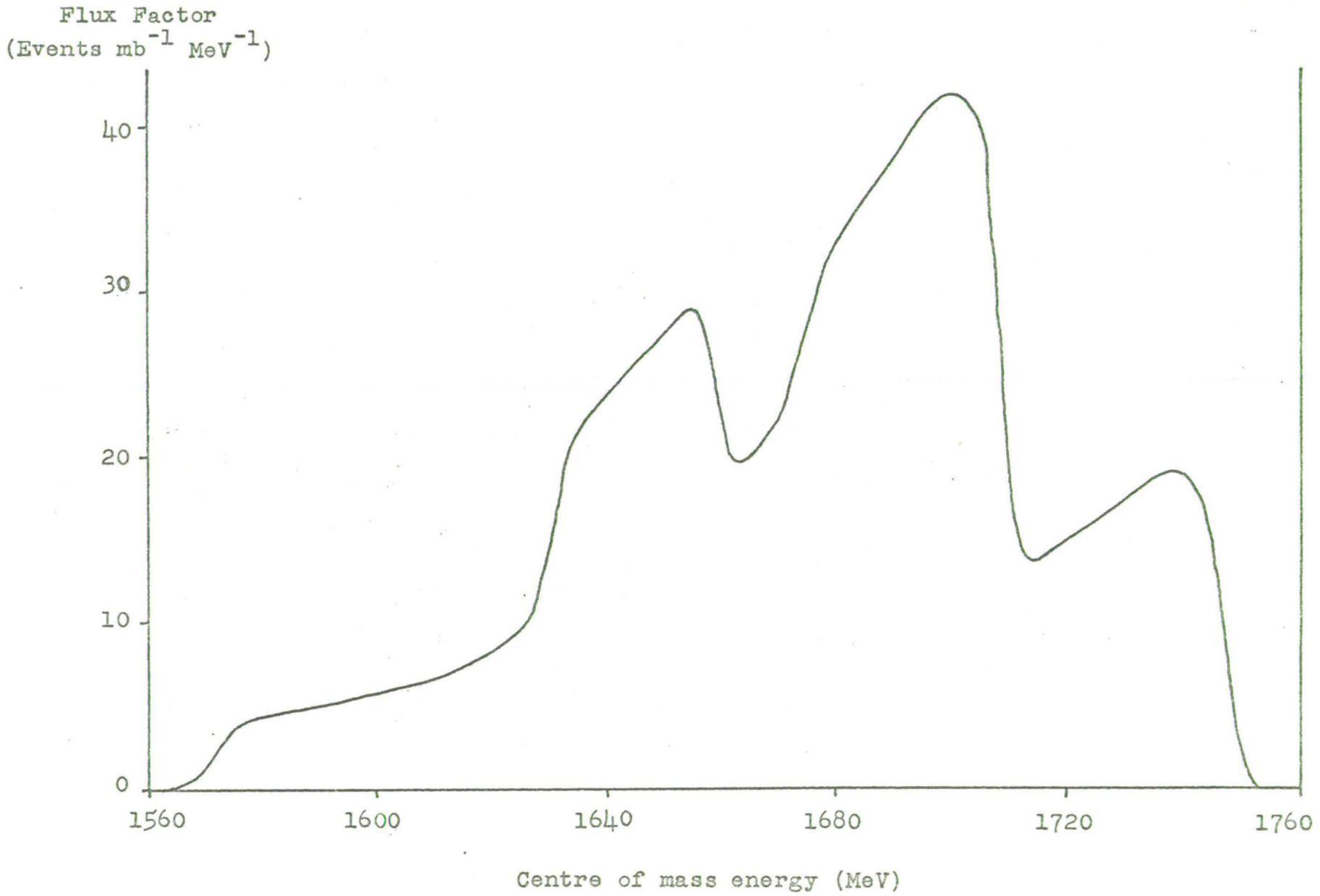

Fig. 12. Flux factor for all of run 2 and half of runs 1 and 3.

for a given cross-section. The more events obtained, the better the statistical accuracy of the experiment. In Figure 12 we show the flux factor as a function of the centre of mass energy for all the film analysed so far. This comprises all of run 2 and half of runs 1 and 3. The gradual fall-off at each end is due to the momentum spread of the beam described above. Figure 12 also illustrates the continuous distribution in energy of the events in this experiment which contrasts with the spectrum obtained in hydrogen experiments.

II.15 Total and Differential Cross-sections

Having evaluated the weight and normalization factors for each accepted event, the total cross-sections for the channels being studied were calculated by summing the contributions for each event as explained in the last section. In this section we present the results of these cross-section calculations based on the data currently available.

The centre of mass energy range covered by runs 1, 2 and 3 was divided into six regions containing approximately equal statistics:

I	1570 - 1630 MeV
II	1630 - 1650 MeV
III	1650 - 1670 MeV
IV	1670 - 1690 MeV
V	1690 - 1710 MeV
VI	1710 - 1750 MeV

and an average total cross-section for the $\Lambda^\circ\pi^\circ$, $\Sigma^\circ\pi^\circ$, $\Lambda^\circ\pi^\circ\pi^\circ$, $\Sigma^\circ\pi^\circ\pi^\circ$ and $\Lambda^\circ\eta^\circ$ channels calculated for each region. The lower limit of region III for the $\Lambda^\circ\eta^\circ$ channel was taken as threshold, 1664 MeV. The calculated $\Lambda^\circ\eta^\circ$ cross-section included all the neutral decay modes of the η° by weighting each $\Lambda^\circ\eta^\circ$ event to account for the $\frac{\eta^\circ \to 2\gamma}{\eta^\circ \to \text{neutrals}}$ branching ratio of 0.534 ± 0.013[1]. Only 5 events in the $\Lambda^\circ\pi^\circ\pi^\circ\pi^\circ$ channel were accepted, all above the $\Lambda^\circ\eta^\circ$ threshold, and in every case the $\pi^\circ\pi^\circ\pi^\circ$ invariant mass was compatible with the η° mass, suggesting that these events had all been produced through $\Lambda^\circ\eta^\circ$. This was supported by the fact that the weighted number of $\Lambda^\circ\pi^\circ\pi^\circ\pi^\circ$ events was compatible with the $\frac{\eta^\circ \to \pi^\circ\pi^\circ\pi^\circ}{\eta^\circ \to \text{neutrals}}$ branching ratio of 0.422 ± 0.015[1]. No cross-section is therefore quoted for the $\Lambda^\circ\pi^\circ\pi^\circ\pi^\circ$ channel as this is included among the neutral η° decays in the $\Lambda^\circ\eta^\circ$ channel. This agreement between our results for the $\Lambda^\circ\eta^\circ$ and $\Lambda^\circ\pi^\circ\pi^\circ\pi^\circ$ channels is evidence for the correctness of our analysis as these are the simplest and most complex channels respectively being studied by this experiment.

One problem remaining, however, concerned the loss of events in which the Λ° or Σ° had a laboratory momentum less than 190 MeV/c. These were removed by a cut described in Section II.5. This cut does not affect the $\Lambda^\circ \eta^\circ$ channel but removes events from the $\Lambda^\circ \pi^\circ$ and $\Sigma^\circ \pi^\circ$ channels with $\cos \theta^*$ greater than about +0.9, where θ^* is the angle between the incident K^- and outgoing π° directions in the reaction centre of mass frame. To correct for this loss, the observable part of the differential cross-section for the $\Lambda^\circ\pi^\circ$ and $\Sigma^\circ\pi^\circ$ channels in each energy region was fitted by a least squares method to a Legendre polynomial expansion of the form

$$\frac{d\sigma}{d\Omega} = \lambda\!\!\!^{-2} \sum_{n=0}^{L} A_n P_n(\cos \theta^*)$$

where $\lambda\!\!\!^{-}$ was the average incident centre of mass wavelength for the energy region divided by 2π, the coefficients A_n were constants and L was 5 for $\Lambda^\circ\pi^\circ$ and 4 for $\Sigma^\circ\pi^\circ$. Higher order terms were compatible with zero. In these fits the integral over the observable part of each fitted differential cross-section was constrained to be equal to its measured value. The fitted angular distributions were then extrapolated to $\cos \theta^* = +1$ and integrated from $\cos \theta^* = -1$ to $\cos \theta^* = +1$ to give the final total cross-sections for these channels. For the $\Lambda^\circ\pi^\circ\pi^\circ$ channel, the loss due to this cut was about 1°/o and in the $\Sigma^\circ\pi^\circ\pi^\circ$ channel it was even smaller

so no correction was applied in view of the magnitude of the statistical error.

Table 8 gives the number of accepted events before weighting for each channel and each energy region together with, in parenthises for the $\Lambda^{o}\pi^{o}$ and $\Sigma^{o}\pi^{o}$ channels, the largest observable value of $\cos\theta^{*}$ in each case. Table 9 gives the final total cross-sections in millibarns calculated on the basis of these events and also the total cross-section for reactions of the form $K^{-}p \rightarrow \Lambda^{o}$ + neutrals, which is the sum of all the cross-sections measured in this experiment. In Figures 13 and 14 we show the differential cross-sections for the $\Lambda^{o}\pi^{o}$ and $\Sigma^{o}\pi^{o}$ channels in the six energy regions of Table 9 together with curves showing in each case the fitted Legendre expansion used to obtain the total cross-section.

The errors indicated in Table 9 and Figures 13 and 14 are purely statistical and include the error on the extrapolation to $\cos\theta^{*} = +1$ in the $\Lambda^{o}\pi^{o}$ and $\Sigma^{o}\pi^{o}$ total cross-sections. There is an additional uncorrelated systematic error of about 10%, which is not shown, due to uncertainties in the cut corrections, in the measurement and fit losses, in the backgrounds and in the normalization.

Channel	Centre of mass energy range (MeV)					
	I 1570-1630	II 1630-1650	III 1650-1670	IV 1670-1690	V 1690-1710	VI 1710-1750
$\Lambda^\circ\pi^\circ$	128 (0.870)	167 (0.906)	190 (0.915)	256 (0.923)	287 (0.930)	251 (0.936)
$\Sigma^\circ\pi^\circ$	81 (0.879)	91 (0.930)	89 (0.942)	100 (0.951)	119 (0.959)	72 (0.966)
$\Lambda^\circ\pi^\circ\pi^\circ$	16	27	36	44	56	50
$\Sigma^\circ\pi^\circ\pi^\circ$	3	2	3	10	11	13
$\Lambda^\circ\pi^\circ\pi^\circ\pi^\circ$	0	0	1	0	2	2
$\Lambda^\circ\eta^\circ$ ($\eta^\circ \to 2\gamma$)	0	0	6	36	29	7

TABLE 8

Number of accepted events before weighting for each channel and each energy region together with, in parenthesis for the $\Lambda^\circ\pi^\circ$ and $\Sigma^\circ\pi^\circ$ channels, the largest observable value of $\cos\theta^*$ in each case.

Channel	Centre of mass energy range (MeV)					
	I 1570-1630	II 1630-1650	III 1650-1670	IV 1670-1690	V 1690-1710	VI 1710-1750
$\Lambda^\circ\pi^\circ$	2.28 ± 0.33	2.69 ± 0.23	2.85 ± 0.25	2.83 ± 0.23	3.01 ± 0.21	2.82 ± 0.19
$\Sigma^\circ\pi^\circ$	2.04 ± 0.31	1.91 ± 0.23	1.73 ± 0.20	1.41 ± 0.15	1.41 ± 0.14	0.85 ± 0.11
$\Lambda^\circ\pi^\circ\pi^\circ$	0.58 ± 0.17	0.81 ± 0.16	1.01 ± 0.17	0.90 ± 0.14	1.06 ± 0.16	1.20 ± 0.18
$\Sigma^\circ\pi^\circ\pi^\circ$	0.20 ± 0.13	0.10 ± 0.07	0.16 ± 0.09	0.49 ± 0.18	0.47 ± 0.16	0.60 ± 0.21
$\Lambda^\circ\ \eta^\circ$ ($\eta^\circ \rightarrow$ neutrals)	0	0	0.71 ± 0.30	0.81 ± 0.14	0.51 ± 0.10	0.13 ± 0.05
Λ°+neutrals	5.10 ± 0.50	5.51 ± 0.37	6.46 ± 0.48	6.44 ± 0.38	6.46 ± 0.35	5.60 ± 0.36

TABLE 9

Total cross-sections in millibarns for each channel and each energy region.

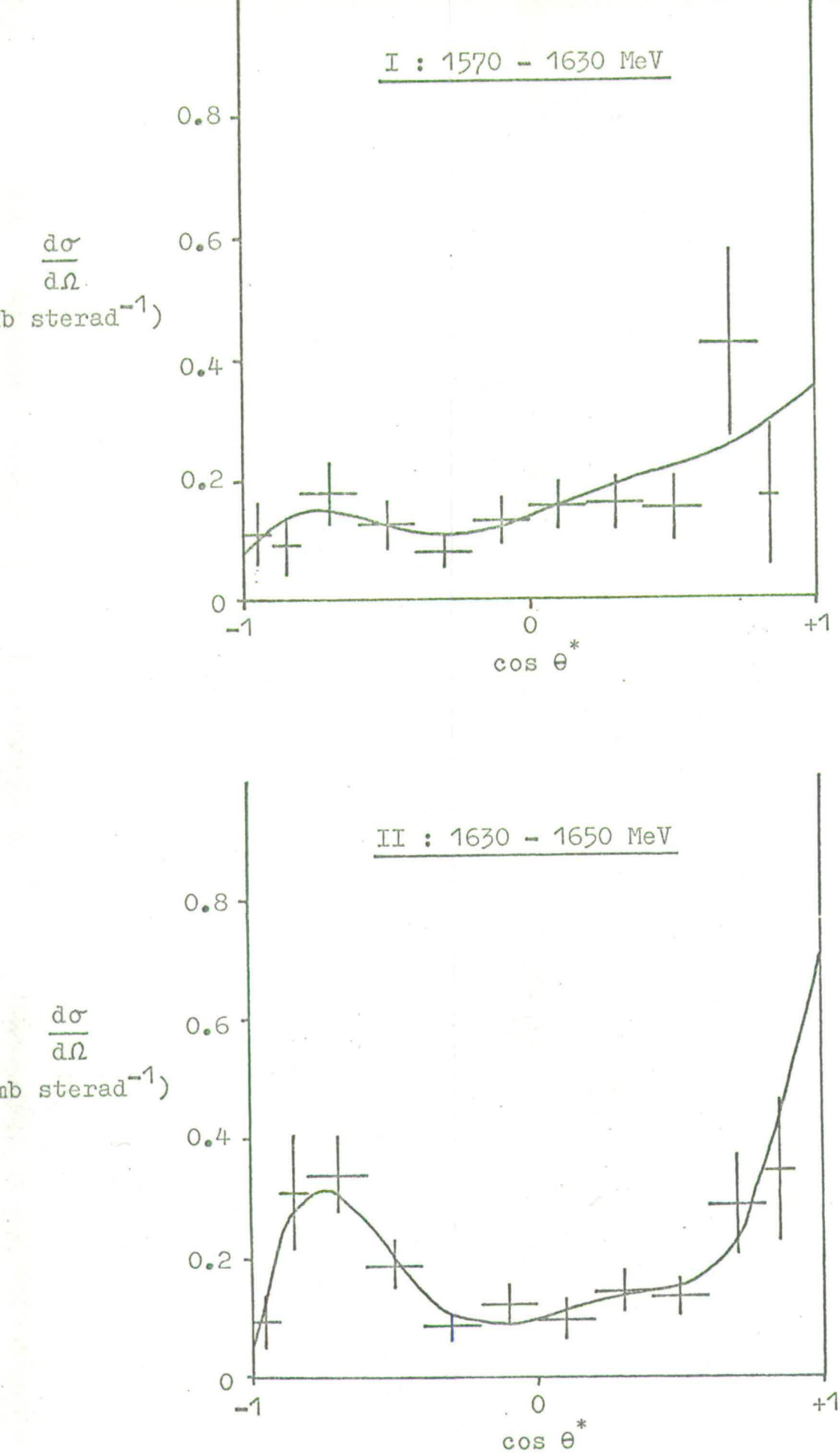

Fig. 13. Differential cross-sections for the $\Lambda^0\pi^0$ channel.

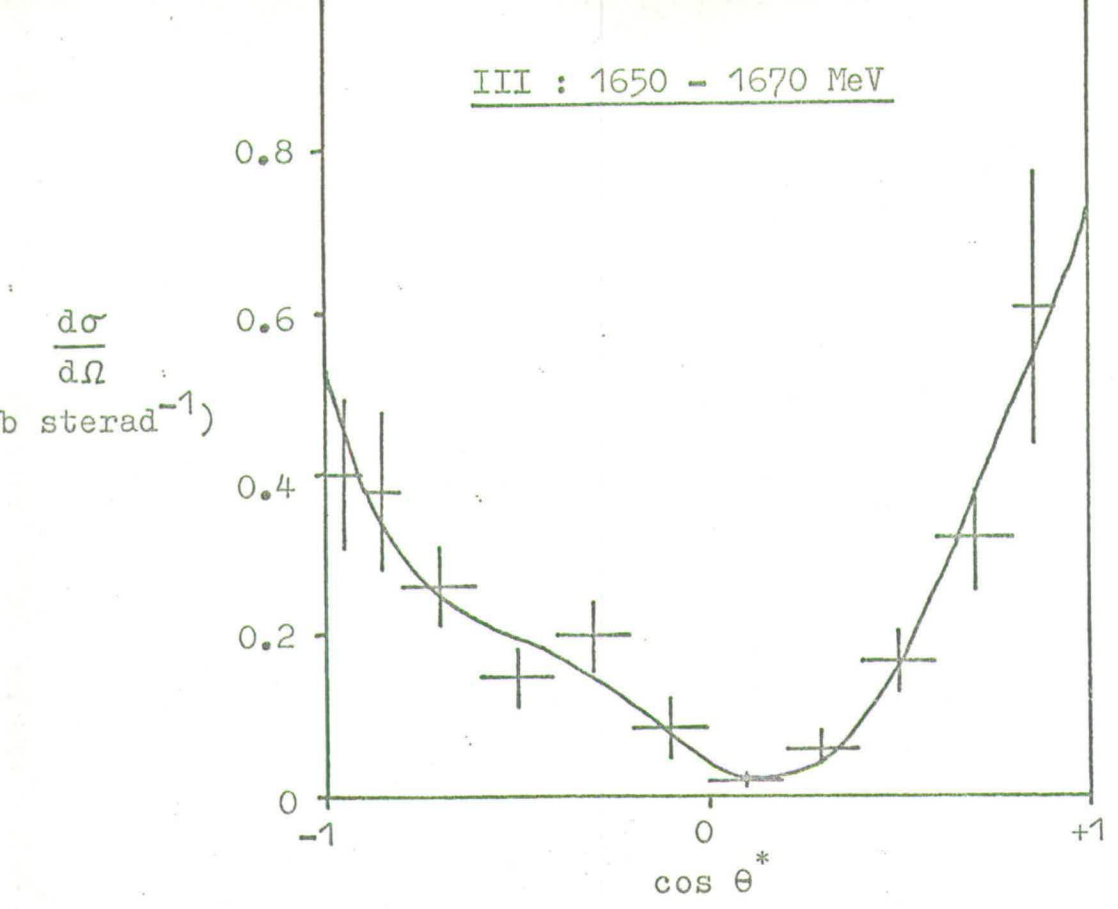

$\frac{d\sigma}{d\Omega}$ (b sterad^{-1})

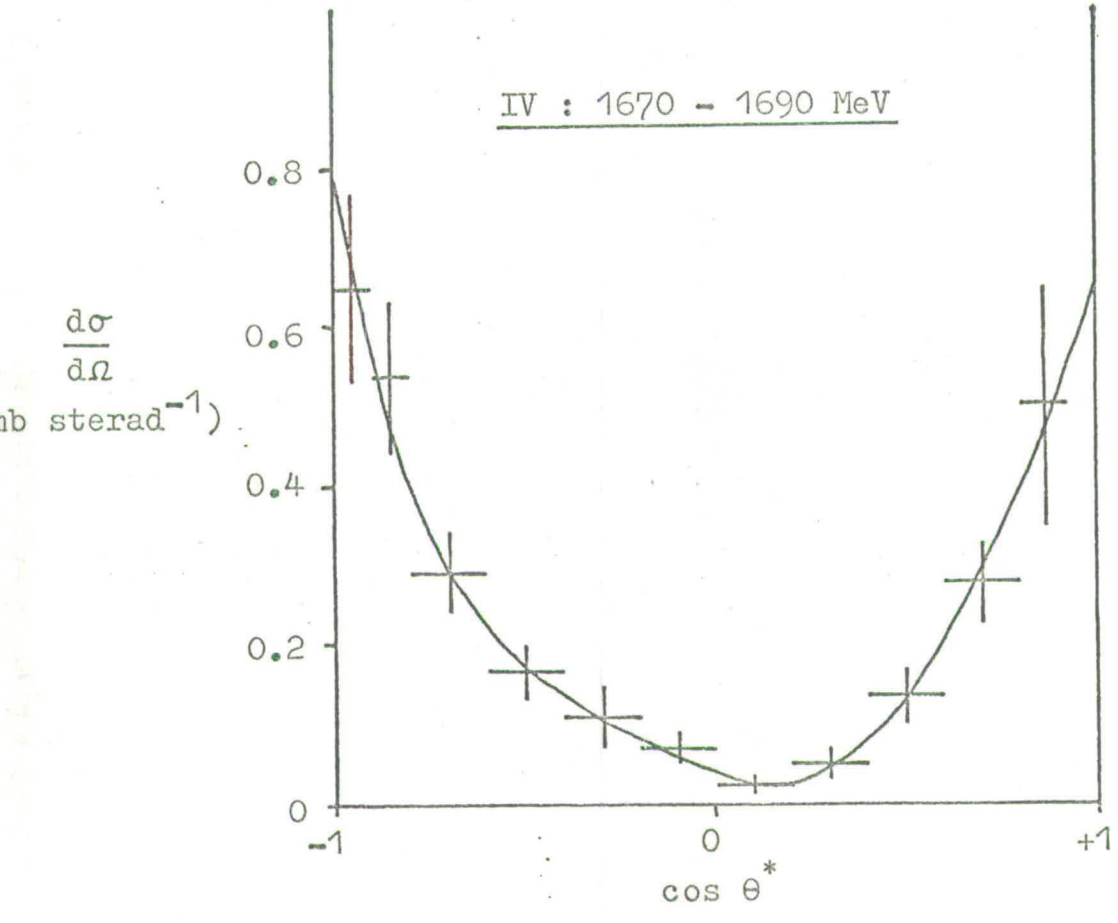

$\frac{d\sigma}{d\Omega}$ (mb sterad^{-1})

Fig. 13. Differential cross-sections for the $\Lambda^{o}\pi^{o}$ channel.

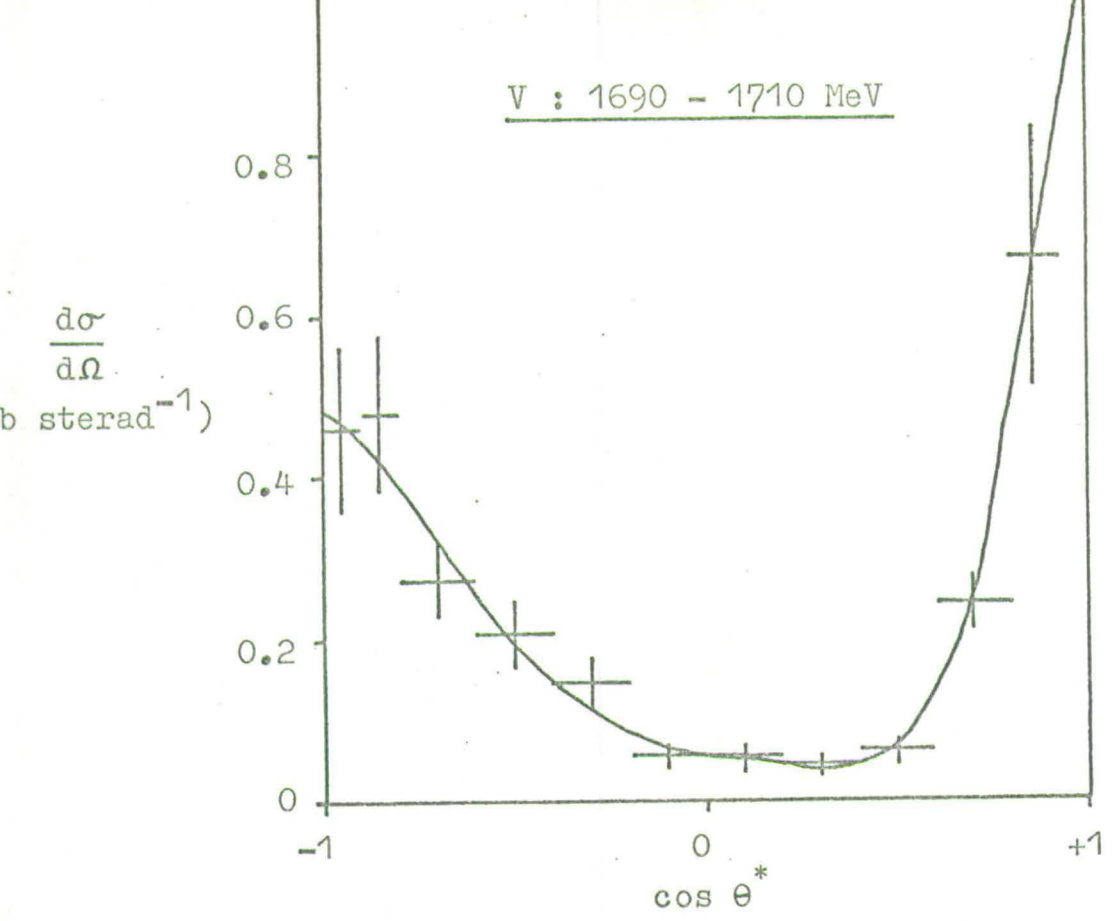

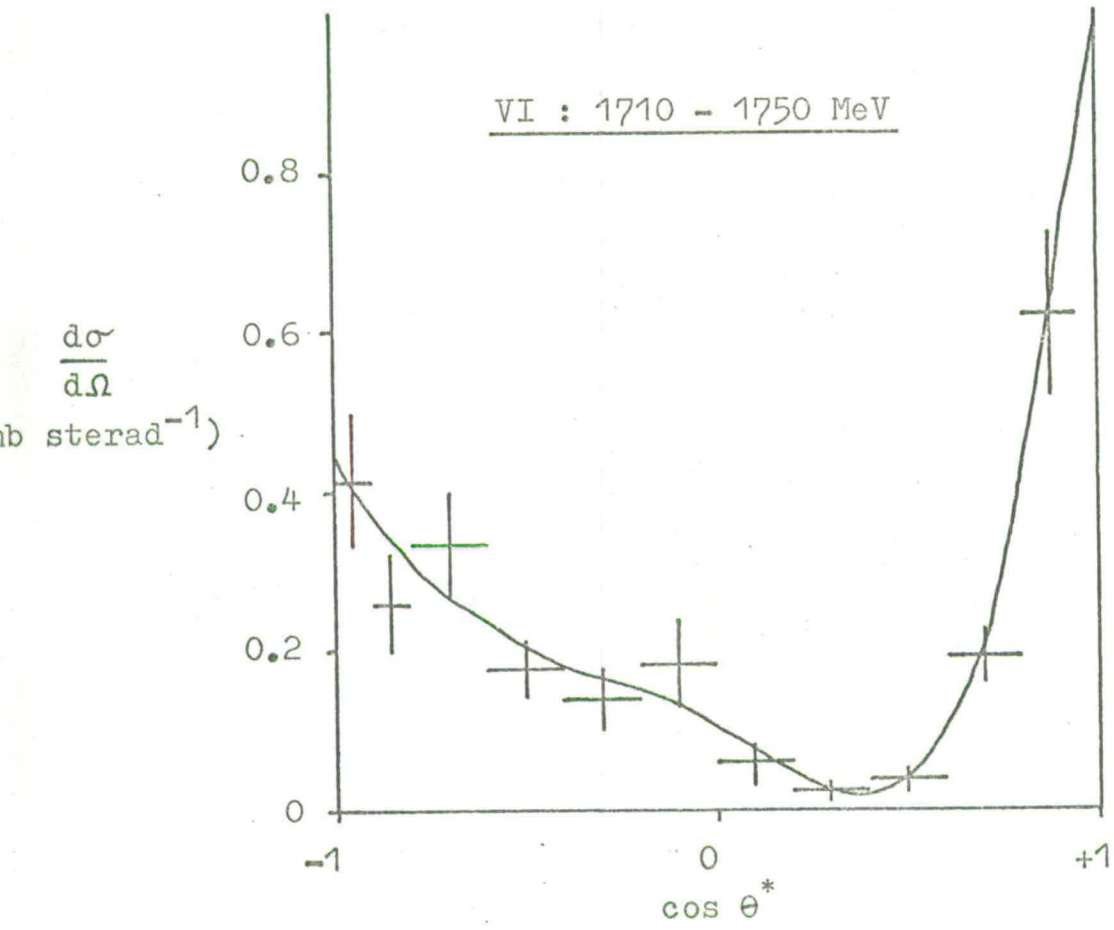

Fig. 13. Differential cross-sections for the $\Lambda^{o}\pi^{o}$ channel.

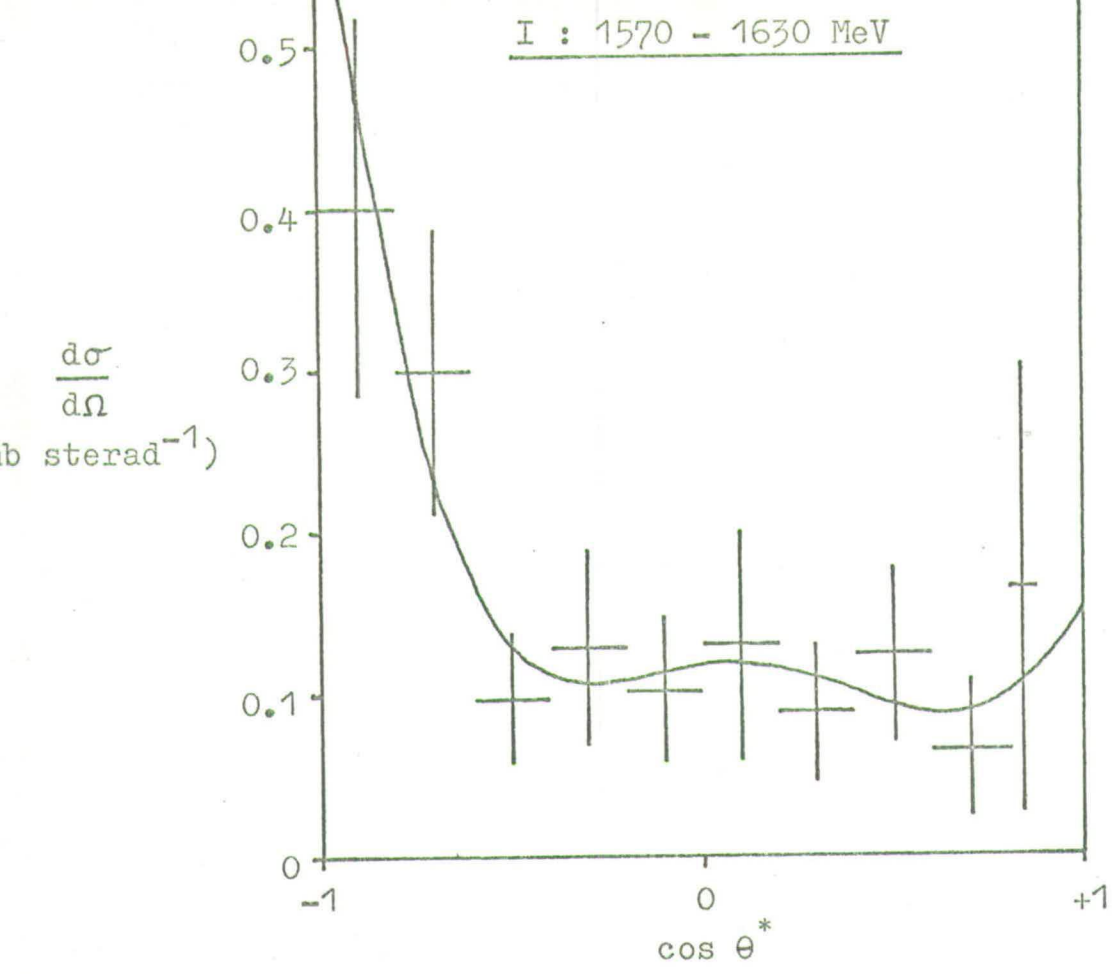

$\frac{d\sigma}{d\Omega}$ (mb sterad^{-1})

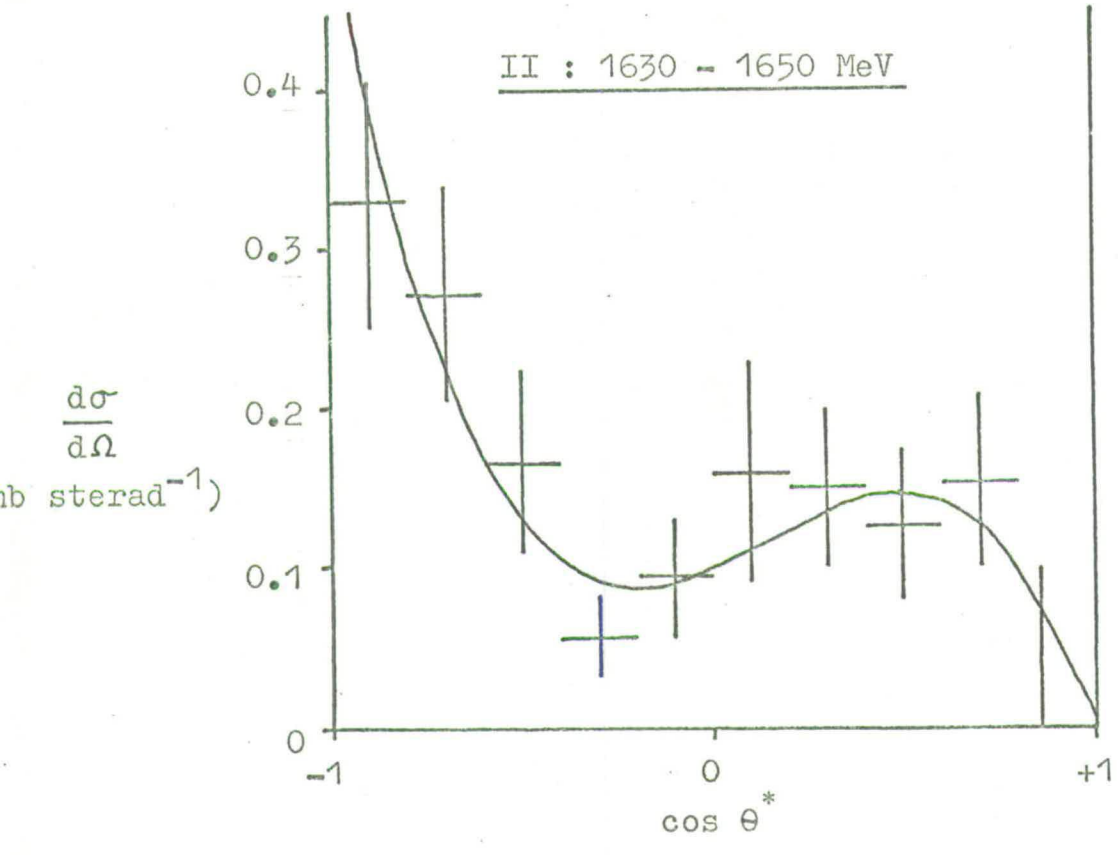

$\frac{d\sigma}{d\Omega}$ (mb sterad^{-1})

Fig. 14. Differential cross-sections for the $\Sigma^{o}\pi^{o}$ channel.

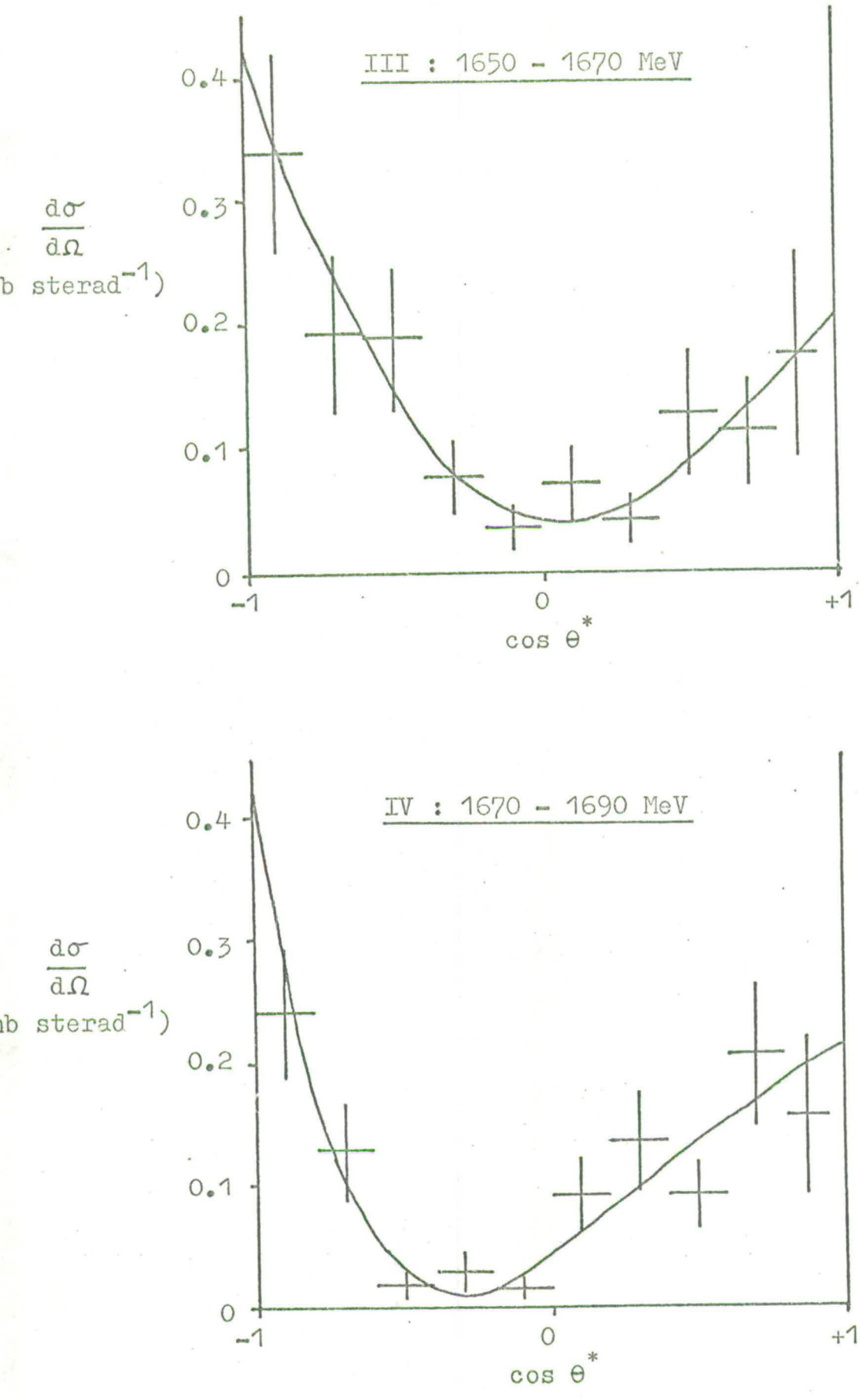

Fig. 14. Differential cross-sections for the $\Sigma^{o}\pi^{o}$ channel.

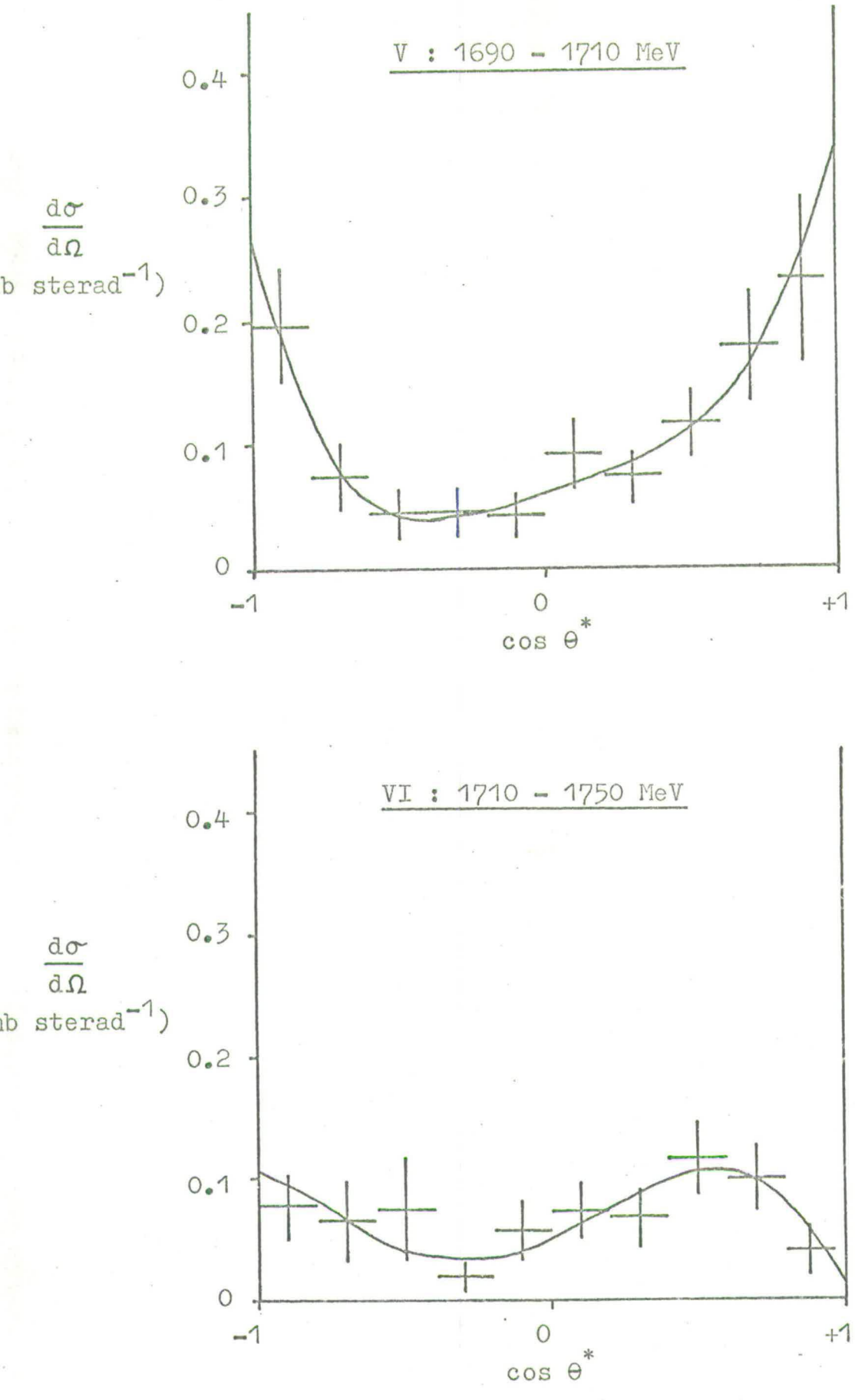

Fig. 14. Differential cross-sections for the $\Sigma^{o}\pi^{o}$ channel.

II.16 Comparison with Previous Experiments

In order to make a comparison at this stage with the published results of previous experiments in our energy range, both in hydrogen[2,3,4,10] and in heavy liquid[11], we show in Figures 15, 16 and 17 all the currently available measurements of total cross-sections for $K^-p \rightarrow \Lambda^\circ$ + neutrals, $K^-p \rightarrow \Lambda^\circ\pi^\circ$ and $K^-p \rightarrow \Sigma^\circ\pi^\circ$ respectively together with our results. It can be seen that in the Λ° + neutrals and $\Lambda^\circ\pi^\circ$ channels, where hydrogen analyses need make no assumptions, good agreement exists confirming our results in these cases. However for $\Sigma^\circ\pi^\circ$, where hydrogen experiments must make important assumptions about the nature of the distribution of the missing mass to the Λ° in order to extract the total cross-section, we find a significant difference, especially between our results and those of the CERN-Heidelberg-Saclay (CHS) collaboration[2]. In particular, we do not see the large bump in the $\Sigma^\circ\pi^\circ$ total cross-section centred at about 1670 MeV. The agreement of Figures 15 and 16 indicates that this cannot be ascribed to normalization problems. Some indication of the reason for this disagreement can be seen in Figure 18 where we show the combined total cross-sections for $K^-p \rightarrow \Lambda^\circ\pi^\circ\pi^\circ$ and $K^-p \rightarrow \Sigma^\circ\pi^\circ\pi^\circ$ including our results which are the first accurate direct measurement for these channels. The assumptions made in hydrogen experiments about the production mechanism in these channels in order to analyse the missing-mass distributions were that these distributions were

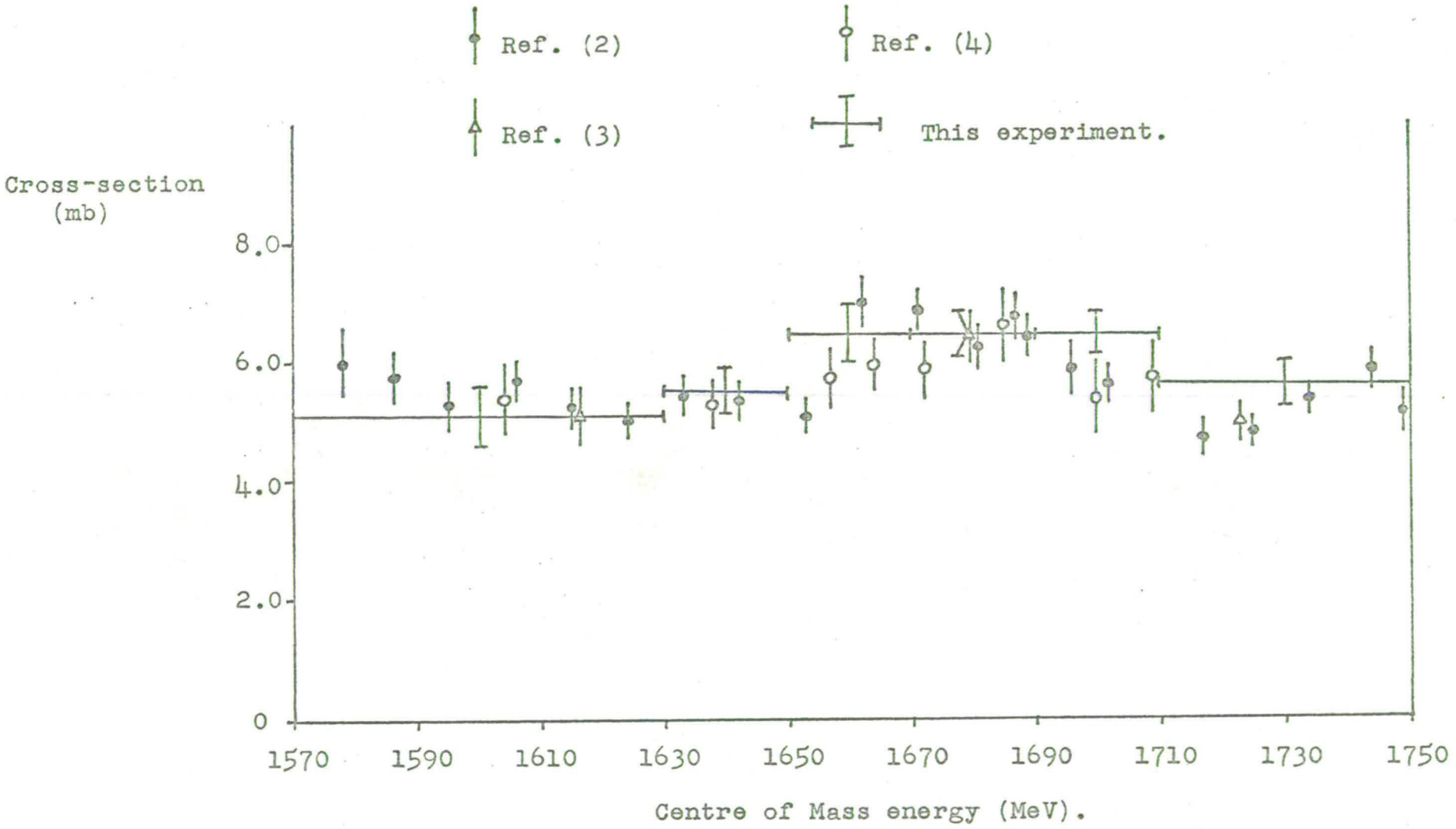

Fig. 15. Total cross-section measurements for $K^- p \rightarrow \Lambda^\circ$ + neutrals.

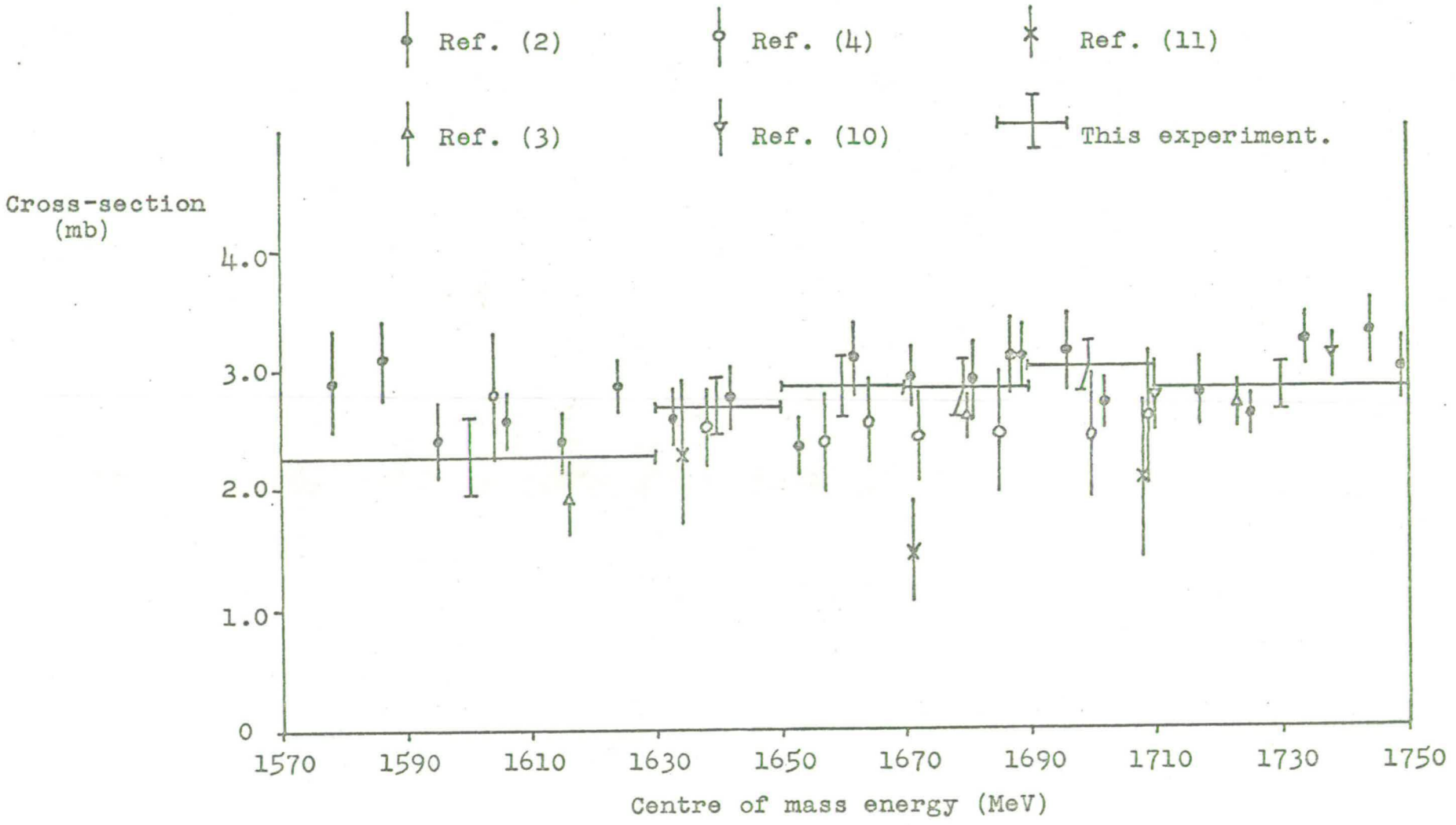

Fig. 16. Total cross-section measurements for $K^- p \rightarrow \Lambda^0 \pi^0$.

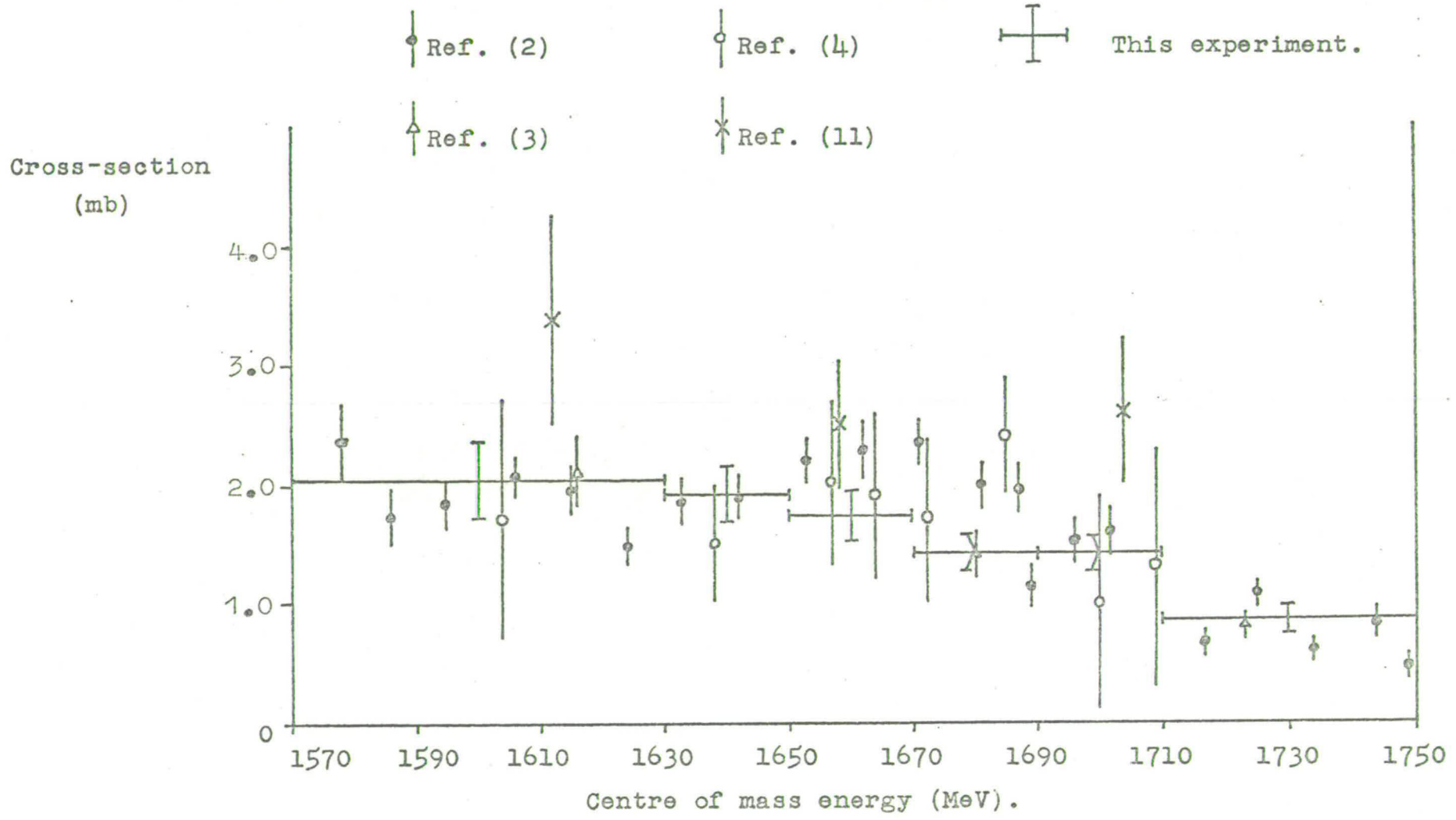

Fig. 17. Total cross-section measurements for $K^- p \rightarrow \Sigma^0 \pi^0$.

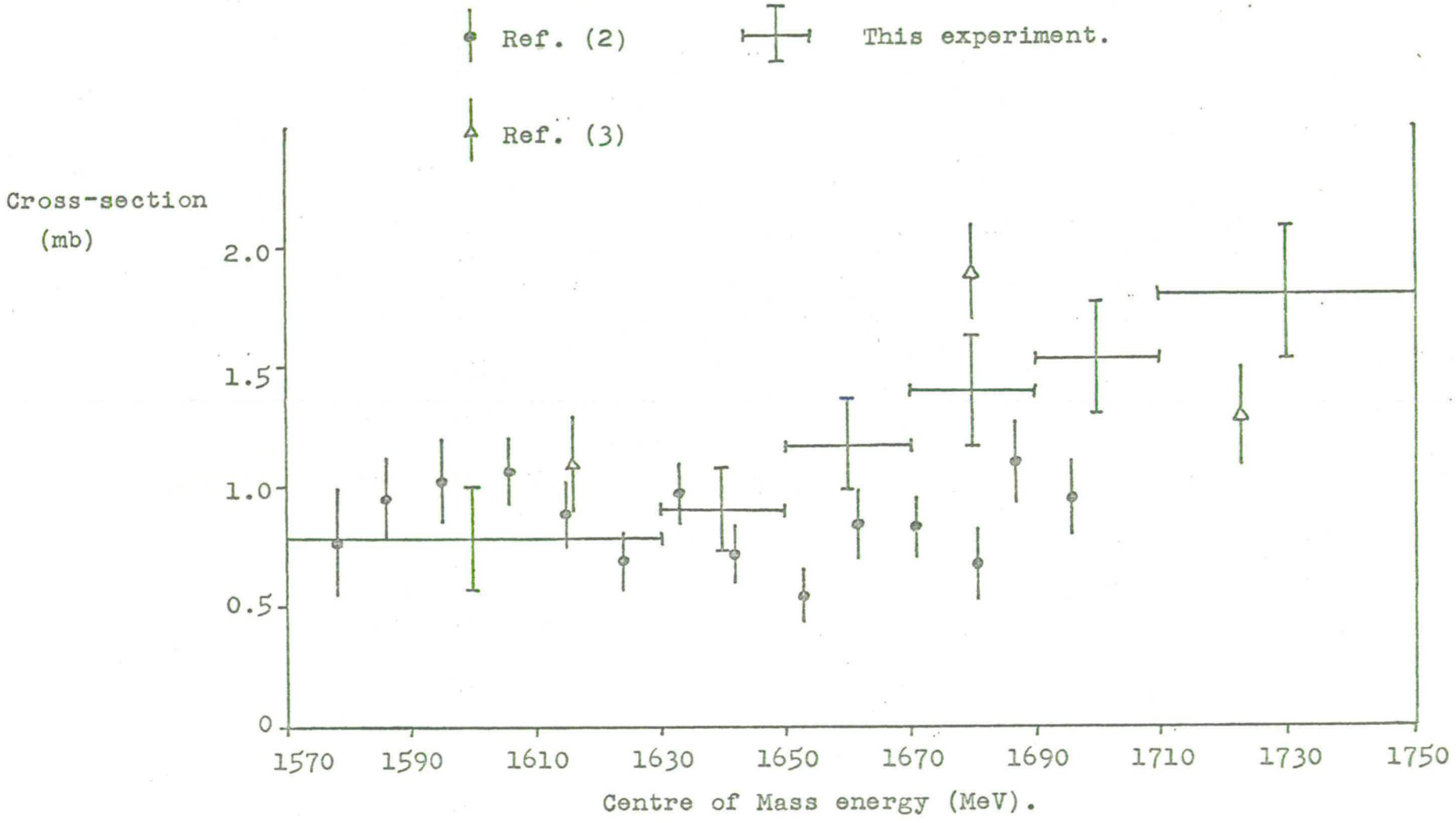

Fig. 18. Total cross-section measurements for $K^- p \rightarrow \Lambda^0 \pi^0 \pi^0 + K^- p \rightarrow \Sigma^0 \pi^0 \pi^0$.

determined solely by phase space. Indications are however that $\Lambda^\circ\pi^\circ\pi^\circ$ is produced largely via $\Sigma^\circ(1385)\pi^\circ$ and $\Sigma^\circ\pi^\circ\pi^\circ$ through $\Lambda^\circ(1405)\pi^\circ$ [11,12]. It can be seen from Figure 18 that hydrogen analyses therefore tend to underestimate the total cross-sections for the three-body final states and as the Λ° + neutrals cross-section is in agreement it seems reasonable to suppose that this is the source of the extra $\Sigma^\circ\pi^\circ$ events. If this argument is correct, it throws doubt on the amount of $\Lambda(1670)$ formation contributing to the $\Sigma^\circ\pi^\circ$ channel as measured in partial wave analyses of hydrogen experiments[13,14], since this S-wave resonance is supposed to be the reason for the bump in the $\Sigma^\circ\pi^\circ$ total cross-section at 1670 MeV. Further evidence for this point of view was obtained by analysing our three-body events in the same way as was done in hydrogen missing-mass analyses when we found that the three-body contamination thus introduced into $\Sigma^\circ\pi^\circ$ would very likely be S-wave contributing uniformly at all production angle cosines. The validity or otherwise of these suppositions will be investigated in the following chapter where we describe a partial wave analysis of our data for the $\Lambda^\circ\pi^\circ$ and $\Sigma^\circ\pi^\circ$ channels. The quality of the data from the only previous heavy liquid experiment[11] is not sufficiently good to resolve any of the above problems.

CHAPTER III

A PARTIAL WAVE ANALYSIS OF THE $\Lambda^{\circ}\pi^{\circ}$ AND $\Sigma^{\circ}\pi^{\circ}$ CHANNELS

III.1 Maximum Likelihood Approach

A fundamental difference between this experiment and hydrogen bubble chamber experiments is in the distribution of events as a function of ω, the centre of mass energy of the $K^{-}p$ interaction. (We shall henceforth drop the asterisk on centre of mass variables.) Whereas in hydrogen experiments events only occur at certain energies determined by the beam momenta, we have events fairly evenly distributed throughout our energy range. This makes it an inefficient process to bin our events in ω in order to carry out a least squares fit of the data in the $\Lambda^{\circ}\pi^{\circ}$ and $\Sigma^{\circ}\pi^{\circ}$ channels to some energy-dependent model as is usually done in hydrogen experiments. For this reason, a maximum likelihood fitting procedure has been adopted as making the best use of the data at our disposal.

In order to use a maximum likelihood technique, the experimental quantities governing the distribution of observed $\Lambda^{\circ}\pi^{\circ}$ and $\Sigma^{\circ}\pi^{\circ}$ events, namely the normalization factor and the probability of detecting and accepting an event, must be determined as continuous functions of the relevant kinematical variables. The flux factor has already been established as described in Section II.14 as a function of ω but so far the detection efficiency has

only been measured for each event and applied in the form of a weight for calculating cross-sections. To determine the detection efficiency function everywhere, a Monte Carlo simulation was constructed which reproduced in every detail the detection and analysis process applied to the real $\Lambda^{\circ}\pi^{\circ}$ and $\Sigma^{\circ}\pi^{\circ}$ events.

Sufficient Monte Carlo $\Lambda^{\circ}\pi^{\circ}$ and $\Sigma^{\circ}\pi^{\circ}$ events were generated every 3 MeV throughout the energy range of the experiment to give 1000 events of each type detected in the chamber at each energy. These events were uniformly distributed in $\cos\theta$ between $\cos\theta = -1$ and $\cos\theta = +1$ where θ is the centre of mass angle between the incident K^{-} and outgoing π° directions. The statistical error on the detection efficiency function calculated at each energy and angle by passing these events through the Monte Carlo detection process was thus reduced well below the level of the systematic error in the detection efficiency. In this way the experimental detection efficiency for the $\Lambda^{\circ}\pi^{\circ}$ and $\Sigma^{\circ}\pi^{\circ}$ channels was derived as a function of ω and $\cos\theta$.

The accuracy of this simulation was tested by using the Monte Carlo to reproduce many observed distributions for such variables as the momentum, direction and position in the chamber of the various particles produced in these interactions. In all cases, these were in good agreement within statistical errors with the corresponding distributions for the real events confirming our belief that the Monte Carlo accurately reproduced the conditions of the real

experiment.

The work of setting up and running this Monte Carlo simulation was carried out by Diego Gamba and Dr. Al Goshaw at CERN.

III.2 The Likelihood Function

Given the normalization factor, $f(\omega)$, and the detection efficiency, $\eta(\omega, \cos\theta)$, for each channel, a likelihood function must be constructed for the observed distribution of events. Suppose the cross-section distribution for actually producing the events is $D(\omega, \cos\theta)$, then the observed distribution will be

$$N(\omega, \cos\theta) = D(\omega, \cos\theta) f(\omega)\, \eta(\omega, \cos\theta) \quad .$$

The total number of events observed is

$$N_e = \iint N(\omega, \cos\theta)\, d\omega\, d\cos\theta$$

where the ω integration is over the energy range of the experiment and the $\cos\theta$ integration is between -1 and $+1$. If N_b is the total number of acceptable beam tracks in the experiment, the probability that an acceptable beam track produces an observed event at energy ω_i and angle θ_i is

$$P(\omega_i, \cos\theta_i) = \frac{N(\omega_i, \cos\theta_i)}{N_b} \quad .$$

The likelihood, L, that we see the N_e observed events

and that the remaining $(N_b - N_e)$ beam tracks do not produce an observed event is then

$$L = \prod_{i=1}^{N_e} P(\omega_i, \cos\theta_i) \times \left(1 - \iint P(\omega, \cos\theta)\, d\omega\, d\cos\theta\right)^{(N_b - N_e)}$$

and taking the natural logarithm of both sides we get

$$\ell n\, L = \sum_{i=1}^{N_e} \ell n\, P(\omega_i, \cos\theta_i) + (N_b - N_e)\, \ell n \left(1 - \iint P(\omega, \cos\theta)\, d\omega\, d\cos\theta\right).$$

Now $N_e \ll N_b$ and so $\iint P(\omega, \cos\theta)\, d\omega\, d\cos\theta \ll 1$

and the expression for $\ell n\, L$ reduces to

$$\ell n\, L = \sum_{i=1}^{N_e} \ell n\, P(\omega_i, \cos\theta_i) - N_b \iint P(\omega, \cos\theta)\, d\omega\, d\cos\theta \quad .$$

Since we are interested in the production mechanism we need only retain factors involving $D(\omega, \cos\theta)$ giving

$$\ell n\, L = \sum_{i=1}^{N_e} \ell n\, D(\omega_i, \cos\theta_i) - \iint D(\omega, \cos\theta) f(\omega)\, \eta(\omega, \cos\theta)\, d\omega\, d\cos\theta. \qquad (2.1)$$

In order to use this to investigate the distribution of observed events in the $\Lambda^\circ\pi^\circ$ and $\Sigma^\circ\pi^\circ$ channels, we must express $D(\omega, \cos\theta)$ in terms of the production distributions to which we have access in this experiment, namely the differential cross-section $\frac{d\sigma}{d\Omega}(\omega, \cos\theta)$ and the polarization angular distribution $P\frac{d\sigma}{d\Omega}(\omega, \cos\theta)$

where P is the magnitude of the polarization of the Λ^o in the $\Lambda^o\pi^o$ channel and of the Σ^o in the $\Sigma^o\pi^o$ channel. We can use the parity-violating weak decay of the Λ^o to measure $P\frac{d\sigma}{d\Omega}$ since the angular distribution of the proton from the Λ^o decay in the Λ^o rest frame is:

$$\frac{1}{4\pi}(1 + \alpha_\Lambda \vec{P}_\Lambda \cdot \hat{p})$$

where α_Λ is the asymmetry parameter for the Λ^o decay, $\vec{P}_\Lambda$ is the polarization vector of the Λ^o and $\hat{p}$ is a unit vector in the direction of the decay proton. We can therefore write

$$D(\omega, \cos\theta) = \frac{1}{4\pi}\frac{d\sigma}{d\Omega}(\omega, \cos\theta)(1 + \alpha_\Lambda \vec{P}_\Lambda \cdot \hat{p})$$

for the $\Lambda^o\pi^o$ channel with an additional factor $\frac{1}{4\pi}$ for the isotropic Σ^o decay in the $\Sigma^o\pi^o$ channel.

In the $\Lambda^o\pi^o$ channel, $\vec{P}_\Lambda = P_\Lambda \hat{n}$ where P_Λ is the magnitude of the Λ^o polarization and $\hat{n}$ is a unit vector in the direction of the production normal defined by

$$\hat{n} = \frac{\hat{K} \times \hat{\pi}}{|\hat{K} \times \hat{\pi}|}$$

with $\hat{K}$ and $\hat{\pi}$ unit vectors in the reaction rest frame in the directions of the incident K^- and outgoing π^o. Thus we get

$$D_\Lambda(\omega,\cos\theta) = \frac{1}{4\pi}\left[\frac{d\sigma}{d\Omega}(\omega,\cos\theta) + \alpha_\Lambda P_\Lambda \frac{d\sigma}{d\Omega}(\omega,\cos\theta)(\hat{n}\cdot\hat{p})\right] \tag{2.2}$$

In the $\Sigma^o\pi^o$ channel, $\vec{P}_\Lambda = -(\vec{P}_\Sigma \cdot \hat{\ell})\hat{\ell}$ where

$\vec{P}_\Sigma = P_\Sigma \hat{n}$ is the polarization vector of the Σ° with P_Σ the magnitude of the Σ° polarization and $\hat{\ell}$ is a unit vector in the direction of the outgoing Λ° in the Σ° rest frame[15]. We therefore get

$$D_\Sigma(\omega,\cos\theta) = \left(\frac{1}{4\pi}\right)^2 \left[\frac{d\sigma}{d\Omega}(\omega,\cos\theta) - \alpha_\Lambda P_\Sigma \frac{d\sigma}{d\Omega}(\omega,\cos\theta)(\hat{n}\cdot\hat{\ell})(\hat{\ell}\cdot\hat{p}) \right] \quad (2.3)$$

Inserting (2.2) or (2.3) into equation (2.1) then gives $\ell n\, L$ for the $\Lambda^\circ\pi^\circ$ or $\Sigma^\circ\pi^\circ$ channel. The resulting expressions for $\ell n\, L$ can be simplified slightly by considering the second term in (2.1). In addition to the integration over ω and $\cos\theta$ there is also an implied integration over the Λ° decay angle $(\hat{n}\cdot\hat{p})$ in the $\Lambda^\circ\pi^\circ$ channel and over the Σ° decay angle $(\hat{n}\cdot\hat{\ell})$ and the Λ° decay angle $(\hat{\ell}\cdot\hat{p})$ in the $\Sigma^\circ\pi^\circ$ channel.

Considering $\Lambda^\circ\pi^\circ$ first, Figure 19 shows the Λ° decay viewed in the Λ° rest frame with $(\hat{n}\cdot\hat{p}) = \sin\psi\cos\phi$. The detection efficiency function for the $\Lambda^\circ\pi^\circ$ channel, $\eta_\Lambda(\omega, \cos\theta)$, has an implicit dependence on the angle ψ as this determines the momenta of the proton and pion in the decay, but is independent of the angle ϕ. Thus the ϕ integration is simply

$$\int_0^{2\pi} \left(\frac{d\sigma}{d\Omega} + \alpha_\Lambda P_\Lambda \frac{d\sigma}{d\Omega} \sin\psi\cos\phi\right) d\phi$$

and the term involving $P_\Lambda \frac{d\sigma}{d\Omega}$ vanishes. After the ψ integration, we finally get the following expression for

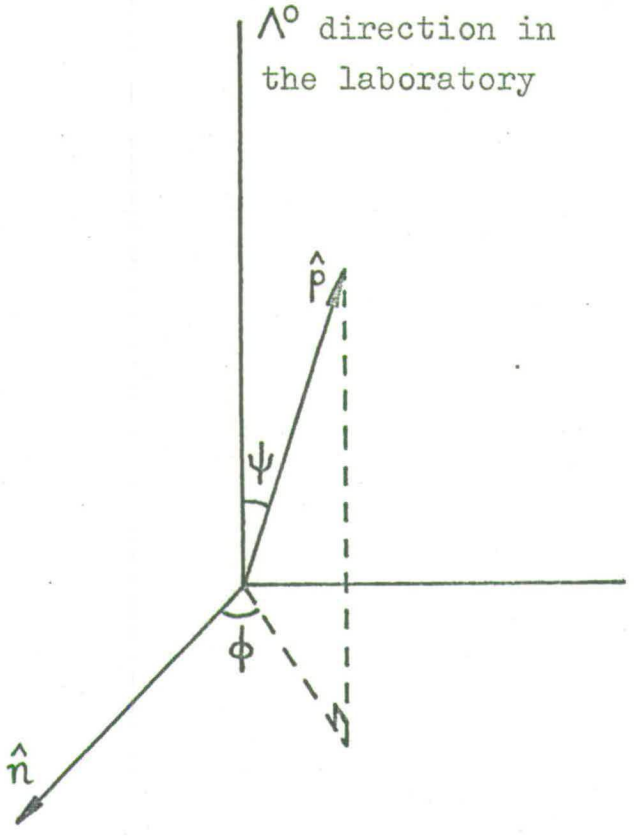

Fig. 19. Λ^0 decay viewed in the Λ^0 rest frame.

$\ell n\ L$ in the $\Lambda^{o}\pi^{o}$ channel

$$\ell n\ L = \sum_{i=1}^{N_\theta} \ln\left[\frac{d\sigma}{d\Omega}(\omega_i,\cos\theta_i) + \alpha_\Lambda P_\Lambda \frac{d\sigma}{d\Omega}(\omega_i,\cos\theta_i)(\hat{n}.\hat{p})_i\right]$$

$$- \iint \frac{d\sigma}{d\Omega}(\omega,\cos\theta) f(\omega)\eta_\Lambda\ (\omega,\cos\theta)d\omega\ d\cos\theta. \quad (2.4)$$

A similar situation arises in the $\Sigma^{o}\pi^{o}$ channel and Figure 20 shows the Σ^{o} decay viewed in the Σ^{o} rest frame with $(\hat{n}.\hat{\ell}) = \sin\psi\cos\phi$. Again there is an implicit dependence of the $\Sigma^{o}\pi^{o}$ detection efficiency function, $\eta_\Sigma\ (\omega, \cos\theta)$, on ψ as this determines the Λ^{o} and γ momenta, but no dependence on ϕ with the result that the ϕ integration cancels the $P_\Sigma \frac{d\sigma}{d\Omega}$ term under the ω and $\cos\theta$ integration. After all other implicit integrations have been performed, we get for the $\Sigma^{o}\pi^{o}$ channel

$$\ell n\ L = \sum_{i=1}^{N_\theta} \ln\left[\frac{d\sigma}{d\Omega}(\omega_i,\cos\theta_i) - \alpha_\Lambda P_\Sigma \frac{d\sigma}{d\Omega}(\omega_i,\cos\theta_i)(\hat{n}.\hat{\ell})_i(\hat{\ell}.\hat{p})_i\right]$$

$$- \iint \frac{d\sigma}{d\Omega}(\omega,\cos\theta) f(\omega)\eta_\Sigma\ (\omega,\cos\theta)d\omega\ d\cos\theta\ . \quad (2.5)$$

Thus for each $\Lambda^{o}\pi^{o}$ event we need to know ω, $\cos\theta$ and $(\hat{n}.\hat{p})$ and for each $\Sigma^{o}\pi^{o}$ event ω, $\cos\theta$, $(\hat{n}.\hat{\ell})$ and $(\hat{\ell}.\hat{p})$. This information, together with $f(\omega)$, $\eta_\Lambda\ (\omega,\cos\theta)$ and $\eta_\Sigma\ (\omega, \cos\theta)$ enables us to form a likelihood function for each channel with which we can investigate the dependence on energy and angle of $\frac{d\sigma}{d\Omega}(\omega,\cos\theta)$ and $P\frac{d\sigma}{d\Omega}(\omega,\cos\theta)$.

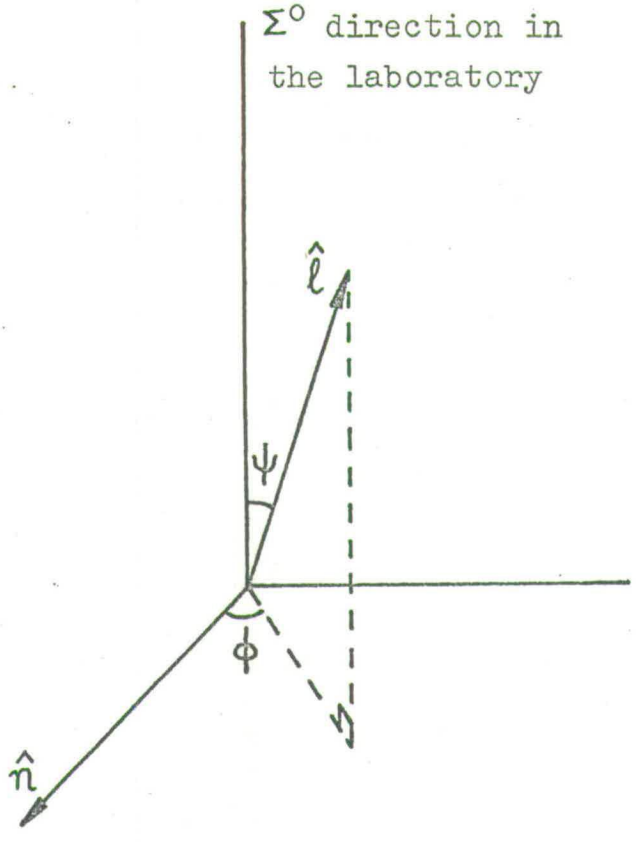

Fig. 20. Σ^0 decay viewed in the Σ^0 rest frame.

III.3 Fits to Legendre Polynomial Expansions

As a first attempt at a maximum likelihood fit, the events in both channels were divided into the energy regions described in Section II.15 and in each region $\frac{d\sigma}{d\Omega}$ and $P\frac{d\sigma}{d\Omega}$ were expanded as follows

$$\frac{d\sigma}{d\Omega}(\cos\theta) = \lambda\!\!\!^{-2} \sum_{n=0}^{L} A_n P_n(\cos\theta)$$

$$P\frac{d\sigma}{d\Omega}(\cos\theta) = \lambda\!\!\!^{-2} \sum_{n=1}^{L} B_n P_n^1(\cos\theta) .$$

$\lambda\!\!\!^{-}$ is the average incident centre of mass wavelength for the energy region divided by 2π, the coefficients A_n and B_n are constants for each region, $P_n(\cos\theta)$ and $P_n^1(\cos\theta)$ are respectively n-th order Legendre polynomials and first associated Legendre polynomials of $\cos\theta$ and L, the order of the expansion, was 5 for $\Lambda^0\pi^0$ and 4 for $\Sigma^0\pi^0$. Higher order terms in the expansions were compatible with zero. These simple parameterizations substituted in equations (2.4) and (2.5) enabled us, by maximizing $\ell n\, L$, to fit the data in each energy region in a model-independent way using relatively few parameters, namely the A and B coefficients.

The fitted A_0 coefficients were then used to calculate average total cross-sections, $\bar{\sigma}$, for each energy region since

$$\bar{\sigma} = 4\pi\, \lambda\!\!\!^{-2}\, A_0 .$$

These total cross-sections in millibarns are shown in Tables 10 and 11 for the $\Lambda^{o}\pi^{o}$ and $\Sigma^{o}\pi^{o}$ channels respectively, together with the results quoted earlier in Section II.15 derived from the event weights. It can be seen that these significantly different methods of analysing the data give very similar results, confirming that the maximum likelihood approach works. In fact all of the A coefficients were in good agreement with their previously derived counterparts. In the absence of a goodness of fit criterion such as the confidence level associated with a χ^2 fit, this agreement with independently derived results is the best indication that the fitted maximum of the likelihood function gives an acceptable solution.

The A and B coefficients from the maximum likelihood fit for the $\Lambda^{o}\pi^{o}$ and $\Sigma^{o}\pi^{o}$ channels are listed in Tables 12 and 13 and displayed in Figures 21 and 22. Also shown are the A and B coefficients derived and tabulated by the CHS group[2] who have performed the most comprehensive hydrogen experiment to date in this energy range, together with some results of a higher energy study of the $\Lambda^{o}\pi^{o}$ channel[10]. The errors quoted on our fitted coefficients are purely statistical and do not take into account a possible systematic error of about 10% inherent in all our results. The CHS errors are also only statistical. It can be seen that, although our fitted coefficients are averaged over quite wide energy ranges and therefore cannot be expected to accurately reproduce the detailed energy dependence

Method of calculation	Centre of mass energy range (MeV).					
	1570-1630	1630-1650	1650-1670	1670-1690	1690-1710	1710-1750
Event weights	2.28 ± 0.33	2.69 ± 0.23	2.85 ± 0.25	2.83 ± 0.23	3.01 ± 0.21	2.82 ± 0.19
Max. Likelihood	2.26 ± 0.27	2.67 ± 0.28	2.76 ± 0.25	2.81 ± 0.22	2.76 ± 0.19	2.91 ± 0.17

TABLE 10

Comparison of total cross-section measurements in millibarns for the $\Lambda^{o}\pi^{o}$ channel using event weights and the maximum likelihood approach.

Method of calculation	Centre of mass energy range (MeV)					
	1570-1630	1630-1650	1650-1670	1670-1690	1690-1710	1710-1750
Event weights	2.04 ± 0.31	1.91 ± 0.23	1.73 ± 0.20	1.41 ± 0.15	1.41 ± 0.14	0.85 ± 0.11
Max. Likelihood	1.93 ± 0.26	1.80 ± 0.24	1.63 ± 0.18	1.45 ± 0.16	1.48 ± 0.15	0.88 ± 0.12

TABLE 11

Comparison of total cross-section measurements in millibarns for the $\Sigma^{o}\pi^{o}$ channel using event weights and the maximum likelihood approach.

	Centre of mass energy range (MeV)					
	1570-1630	1630-1650	1650-1670	1670-1690	1690-1710	1710-1750
A_0	.054 ± .007	.081 ± .008	.092 ± .008	.103 ± .008	.110 ± .008	.131 ± .008
A_1	.030 ± .016	.040 ± .020	.022 ± .021	.006 ± .020	.019 ± .019	.057 ± .013
A_2	.018 ± .023	.096 ± .029	.138 ± .028	.191 ± .027	.206 ± .025	.274 ± .024
A_3	.013 ± .026	.064 ± .030	.051 ± .030	.038 ± .031	.092 ± .028	.175 ± .001
A_4	-.012 ± .025	.005 ± .029	.010 ± .026	.036 ± .025	.066 ± .023	.137 ± .021
A_5	.017 ± .022	.051 ± .023	-.031 ± .025	.007 ± .025	.030 ± .024	.045 ± .021
B_1	.025 ± .015	.043 ± .014	.005 ± .016	.011 ± .016	-.020 ± .015	.022 ± .020
B_2	.006 ± .013	.001 ± .014	-.029 ± .016	-.026 ± .017	-.017 ± .016	-.019 ± .018
B_3	.006 ± .011	.038 ± .013	.016 ± .014	.001 ± .016	-.007 ± .015	-.033 ± .017
B_4	-.003 ± .011	.001 ± .010	-.018 ± .011	-.010 ± .011	-.004 ± .011	-.046 ± .014
B_5	-.008 ± .010	.023 ± .010	-.001 ± .011	-.008 ± .011	-.006 ± .010	.005 ± .012

TABLE 12

A and B coefficients for the $\Lambda^\circ\pi^\circ$ channel in each energy region from the maximum likelihood fit.

	Centre of mass energy range (MeV)					
	1570-1630	1630-1650	1650-1670	1670-1690	1690-1710	1710-1750
A_0	.046 ± .006	.054 ± .007	.055 ± .006	.053 ± .006	.059 ± .006	.039 ± .005
A_1	-.024 ± .014	-.028 ± .014	-.030 ± .014	.021 ± .013	.035 ± .013	.009 ± .012
A_2	.024 ± .019	.034 ± .017	.059 ± .018	.064 ± .018	.077 ± .018	.006 ± .017
A_3	-.008 ± .020	-.033 ± .019	-.023 ± .018	-.041 ± .017	-.001 ± .017	-.036 ± .018
A_4	-.006 ± .020	-.027 ± .020	-.021 ± .021	.005 ± .019	.031 ± .018	-.018 ± .020
B_1	.045 ± .031	.062 ± .029	.057 ± .033	-.017 ± .027	-.009 ± .025	-.010 ± .029
B_2	.049 ± .035	-.030 ± .026	-.014 ± .027	-.037 ± .028	.006 ± .023	-.016 ± .024
B_3	.032 ± .029	-.014 ± .023	-.002 ± .026	-.016 ± .021	.001 ± .019	-.019 ± .022
B_4	.075 ± .026	.016 ± .019	-.017 ± .022	-.016 ± .017	.021 ± .017	-.038 ± .019

TABLE 13

A and B coefficients for the $\Sigma^0\pi^0$ channel in each energy region from the maximum likelihood fit.

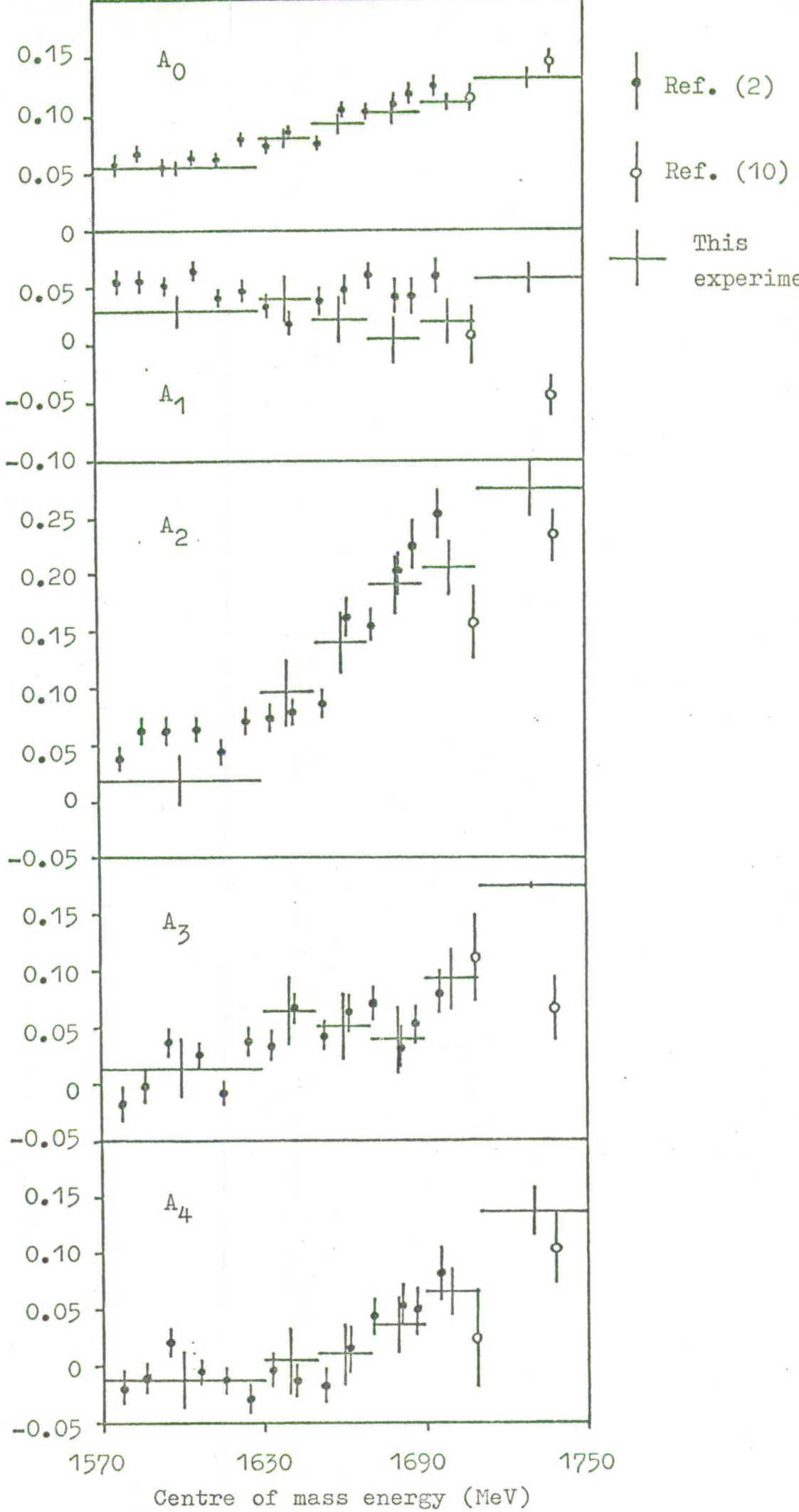

Fig. 21. A and B coefficients for the $\Lambda^{o}\pi^{o}$ channel.

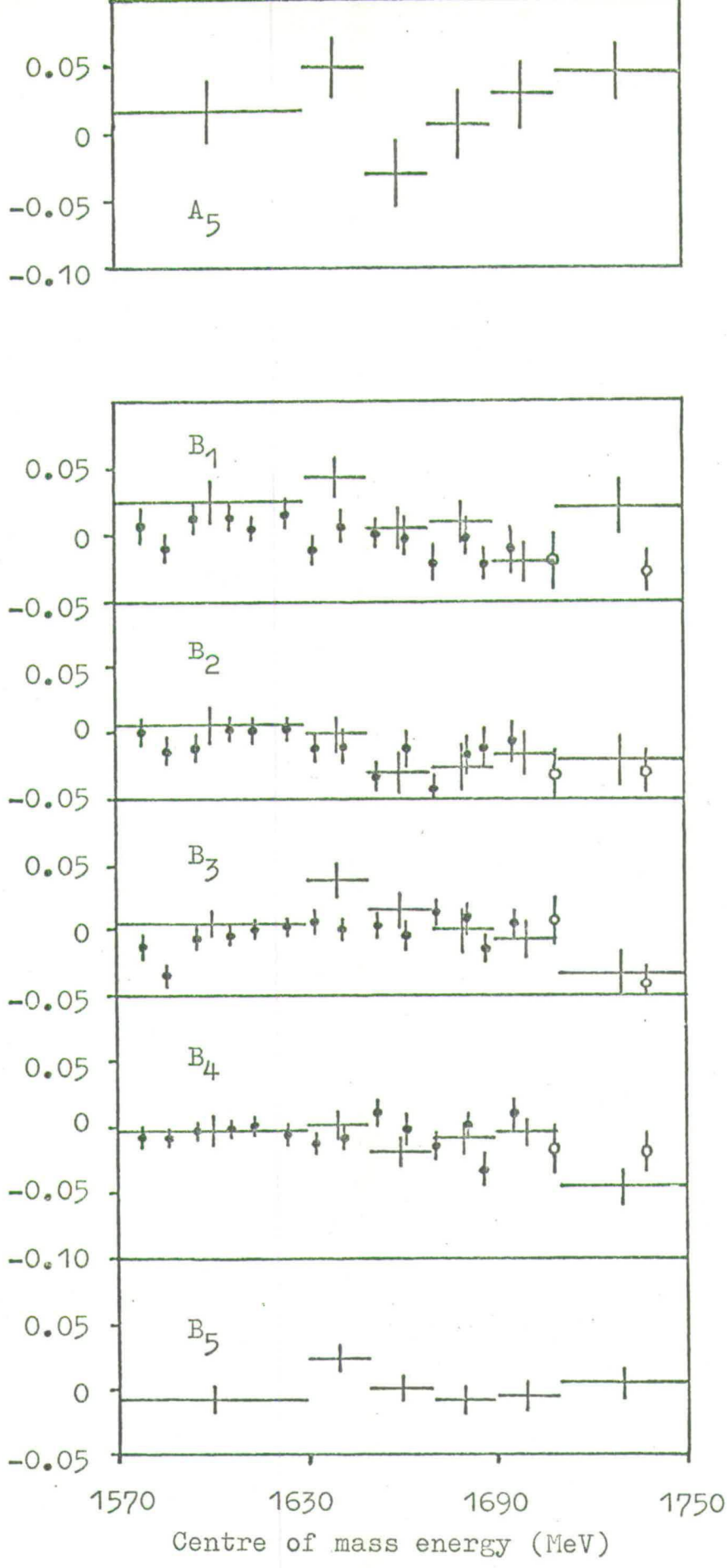

Fig. 21. A and B coefficients for the $\Lambda^{o}\pi^{o}$ channel.

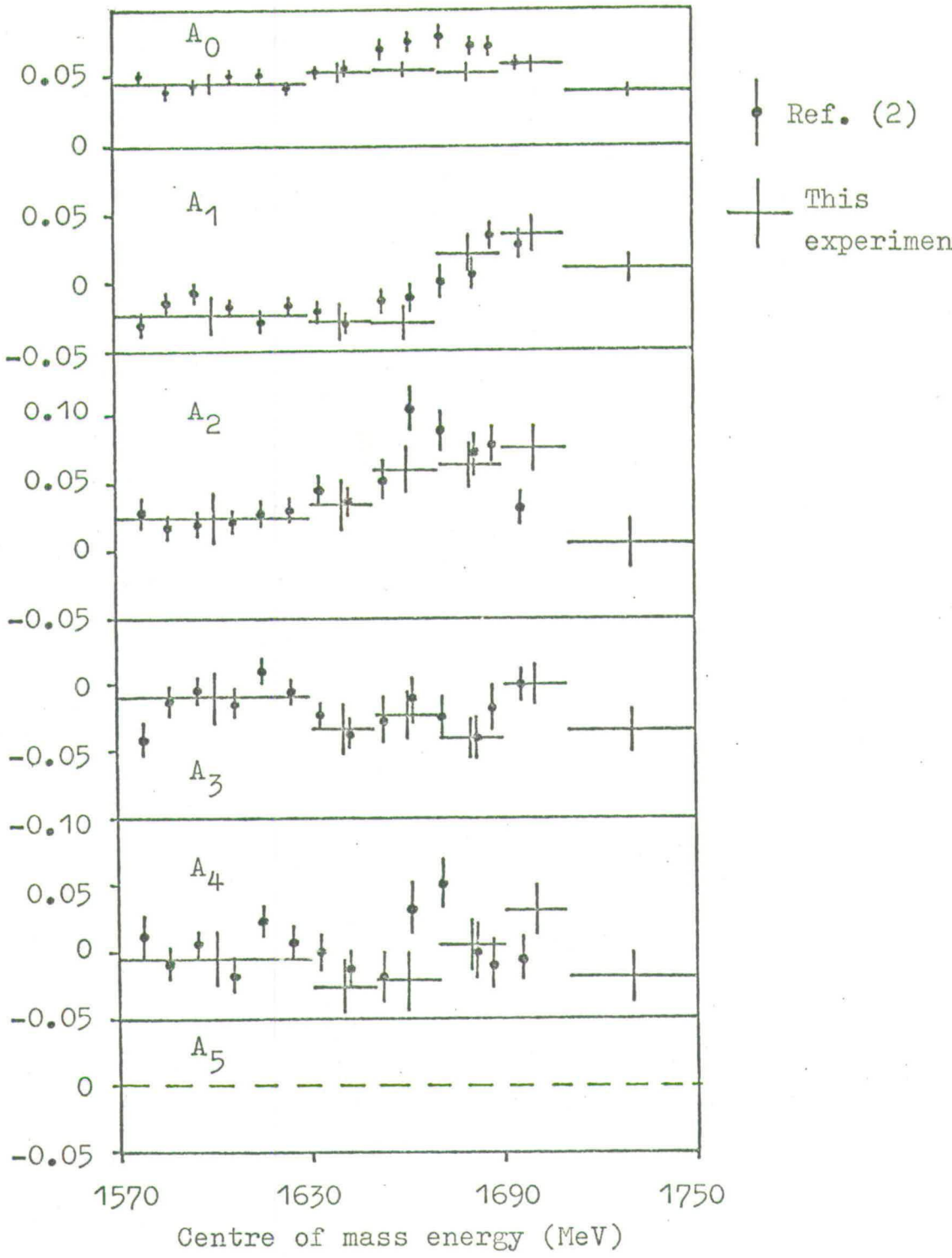

Fig. 22. A and B coefficients for the $\Sigma^{o}\pi^{o}$ channel.

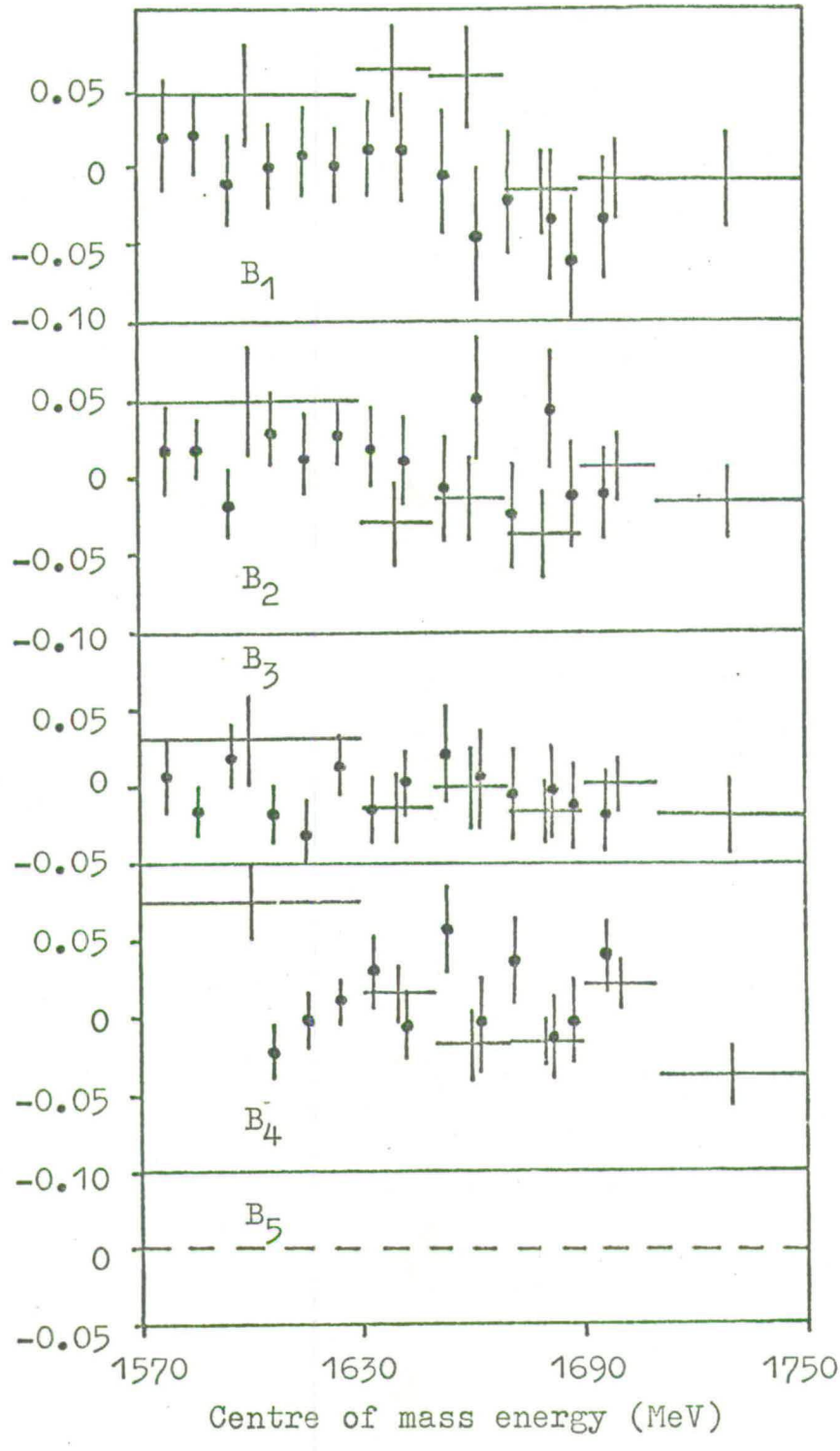

Fig. 22. A and B coefficients for the $\Sigma^0\pi^0$ channel.

of our data, they are in reasonable agreement with the coefficients obtained in hydrogen experiments in $\Lambda^0\pi^0$ as we would expect. This is not so, however, in $\Sigma^0\pi^0$, the most significant difference being in the A_0 coefficient bearing out the conclusions reached in Section II.16.

The next step was to attempt an energy-dependent parameterization of $\frac{d\sigma}{d\Omega}(\omega,\cos\theta)$ and $P\frac{d\sigma}{d\Omega}(\omega,\cos\theta)$. This involved use of the partial wave expansion.

III.4 The Partial Wave Expansion

In spin 0 - spin ½ scattering, the four helicity amplitudes involved are reduced by parity conservation in strong interactions to only two complex amplitudes, the non-spin-flip amplitude $f(\omega,\cos\theta)$ and the spin-flip amplitude $g(\omega,\cos\theta)$, so called because of the relative helicities before and after the interaction in each case. Conservation of angular momentum can then be used to expand these helicity amplitudes as summations of partial wave amplitudes which are eigenstates of the total angular momentum J and the parity P. Expressing these partial wave amplitudes as $T_L^{\pm}(\omega)$ where L is the orbital angular momentum with $J = L \pm \frac{1}{2}$ and $P = -(-1)^L$, we get the familiar expressions

$$f(\omega,\cos\theta) = \lambda \sum_{L=0}^{\infty} \left[(L+1)T_L^+(\omega) + L\, T_L^-(\omega) \right] P_L(\cos\theta)$$

$$g(\omega,\cos\theta) = i\lambda \sum_{L=1}^{\infty} \left[T_L^+(\omega) - T_L^-(\omega) \right] P_L^1(\cos\theta) \qquad (4.1)$$

As the target is unpolarized, the differential cross-section and polarization angular distribution can be represented in terms of f and g thus

$$\frac{d\sigma}{d\Omega} = |f|^2 + |g|^2$$

$$P\frac{d\sigma}{d\Omega} = 2\,\mathrm{Re}(f^* g)\,. \qquad (4.2)$$

Combining (4.1) and (4.2) and employing the orthogonality properties of Legendre polynomials, we can write

$$\frac{d\sigma}{d\Omega}(\omega,\cos\theta) = \lambda^2 \sum_{n=0}^{\infty} A_n(\omega)\, P_n(\cos\theta)$$

$$P\frac{d\sigma}{d\Omega}(\omega,\cos\theta) = \lambda^2 \sum_{n=1}^{\infty} B_n(\omega)\, P_n^1(\cos\theta) \qquad (4.3)$$

where $A_n(\omega)$ and $B_n(\omega)$ are real expressions bilinear in the partial wave amplitudes $T_L^{\pm}(\omega)$ and are documented in the literature for small values of n[16]. Since we are dealing with finite range forces, there is a cut-off in the above summations at a finite value of L depending on the energy and they are therefore useful from a practical point of view for investigating the experimental data.

We can now express the energy dependence of $\frac{d\sigma}{d\Omega}$ and $P\frac{d\sigma}{d\Omega}$ in terms of the energy dependence of a finite number

of partial wave amplitudes $T_L^{\pm}$. The significance of this rests in the fact that, as these partial wave amplitudes are eigenstates of J and P, any resonances formed in the interaction will each excite only one wave with J and P equal to those of the resonance. Our data can therefore be used to search for resonances through the behaviour of the corresponding partial wave amplitudes.

A problem arises, however, in the form of the Minami ambiguity[16]. If we interchange partial wave amplitudes between states with the same value of J but opposite parity, $\frac{d\sigma}{d\Omega}$ is unchanged but $P\frac{d\sigma}{d\Omega}$ changes sign. If we then replace each amplitude by its complex conjugate amplitude, $\frac{d\sigma}{d\Omega}$ is again unchanged and the sign of $P\frac{d\sigma}{d\Omega}$ reverts back to its original value. Thus we have an ambiguity which cannot be resolved by measuring only $\frac{d\sigma}{d\Omega}$ and $P\frac{d\sigma}{d\Omega}$. It can, however, be resolved by a polarized target experiment in which the R parameter is measured since

$$R\frac{d\sigma}{d\Omega} = 2\,\mathrm{Im}\,(f^{*}g)$$

which does not change sign under the complex conjugate transformation. In our case we can use the Wigner condition, derived from causality, to eliminate the solution involving the complex conjugate of the correct amplitudes as in this case resonant amplitudes would move in a clockwise circle in the complex T plane instead of in the permitted counter-clockwise sense. The Wigner condition is implicit in the Breit-Wigner formula described in the next section.

A further condition which we can impose on the partial wave amplitudes is that of unitarity. This constrains the inelastic partial wave amplitudes to lie within a circle in the complex T plane with $\left|T_L^{\pm}\right| \leq \frac{1}{2}$. The constraint of unitarity was not used explicitly in our analysis but we ensured that all our results were in agreement with it.

III.5 Parameterization of the Partial Wave Amplitudes

There are two approaches to the problem of parameterizing the energy dependence of the partial wave amplitudes. In the so-called energy-independent method there is no explicit parameterization and the data are used to obtain the real and imaginary parts of each amplitude at each energy. Problems arise due to the inevitable ambiguities present and criteria must be adopted to select one from the possibly large number of solutions at each energy. This method demands a considerable amount of accurate data and for $\bar{K}N$ scattering the data available at present seem inadequate for this approach to give an acceptably smooth variation with energy judging by the behaviour of the fitted amplitudes in one recent attempt[17].

The alternative approach, which we shall adopt, is known as energy-dependent as each partial wave amplitude is given an explicit energy-dependent parameterization, usually in terms of Breit-Wigner formulae for resonances together with a smoothly-varying background. Several groups have

employed this technique both in single-channel[4,13,18] and multi-channel[19,20] analyses of the $\Lambda\pi$ and $\Sigma\pi$ final states in $\bar{K}N$ interactions in our energy range. It has the disadvantage that it requires assumptions to be made about the nature of each amplitude and can therefore lead to biased results.

The parameterization used in this analysis for a resonant amplitude is the usual Breit-Wigner form

$$T_R(\omega) = \frac{e^{i\phi}\sqrt{X_e X_r}}{\varepsilon - i} \qquad \text{with} \qquad \varepsilon = \frac{2(\omega_R - \omega)}{\Gamma} \; .$$

ω_R is the resonance energy and Γ the width, X_e and X_r are the branching fractions in the elastic and reaction channels respectively and ϕ is a phase angle. The resonance width Γ is given an energy dependence[16,21,22]

$$\Gamma(\omega) = \Gamma_o \frac{\frac{q}{\omega}\frac{(qr)^{2L}}{D_L}}{\left[\frac{q}{\omega}\frac{(qr)^{2L}}{D_L}\right]_R}$$

where Γ_o is assumed to be an energy-independent width, q is the centre of mass momentum of the outgoing particles, r is the radius of interaction, taken as 1 fermi, and D_L is a power series of order $2L$ in (qr) which is tabulated in the literature[22]. The denominator is evaluated at the resonance energy so that, at resonance, $\Gamma = \Gamma_o$. The factor $\frac{q}{\omega}$ takes into account two-body phase space, while the factor $\frac{(qr)^{2L}}{D_L}$ arises from centrifugal

barrier effects in the decay. The independent parameters in $T_R(\omega)$ are therefore ω_R, Γ_o, $\sqrt{X_e X_r}$ and ϕ. Non-resonant amplitudes are parameterized with a background as follows

$$T_B(\omega) = (A + Bp_k + Cp_k^2) + i(D + Ep_k + Fp_k^2)$$

where A, B, C, D, E and F are real constants and p_k is the laboratory momentum of the K^- at the interaction. Each resonant amplitude thus has 4 free parameters and each background 6 free parameters. If a background is required in a resonant wave, the amplitudes $T_R(\omega)$ and $T_B(\omega)$ are simply added.

Every partial wave amplitude is then multiplied by a Clebsch-Gordon coefficient depending on the final state, $\frac{1}{\sqrt{2}}$ for $\Lambda^o\pi^o$ and $-\frac{1}{\sqrt{6}}$ for $\Sigma^o\pi^o$, since

$$\langle \Lambda^o\pi^o \mid T \mid K^-p \rangle = \frac{1}{\sqrt{2}} T_1$$

$$\text{and } \langle \Sigma^o\pi^o \mid T \mid K^-p \rangle = -\frac{1}{\sqrt{6}} T_o$$

where T_1 and T_o are pure isospin 1 and 0 amplitudes respectively.

III.6 Results of the Partial Wave Analyses

The energy and angle dependence of $\frac{d\sigma}{d\Omega}$ and $P\frac{d\sigma}{d\Omega}$ for the $\Lambda^0\pi^0$ and $\Sigma^0\pi^0$ channels can therefore be described in each case by a set of resonance and background parameters which we can adjust in such a way as to maximize $\ell n\, L$ in equations (2.4) and (2.5). Thus we can discover the most likely properties of those resonances which are formed in the interactions $K^-p \rightarrow \Lambda^0\pi^0$ and $K^-p \rightarrow \Sigma^0\pi^0$ between 1570 MeV and 1750 MeV. In this section we describe the results of these partial wave analyses.

It was decided not to use the data from this experiment to try to discover new resonances as there was neither enough data nor computer time available to allow an exhaustive search to be made, but rather to show that our data were of a sufficiently good quality to allow partial wave analysis and to use this to determine better the properties of established and proposed resonances formed in the $\Lambda^0\pi^0$ and $\Sigma^0\pi^0$ channels in our energy range, especially in view of the previously mentioned disagreements with hydrogen experiments in $\Sigma^0\pi^0$. It is proposed that our data will be incorporated in a multi-channel partial wave analysis of the $\bar{K}N$ system to be performed in the future at Edinburgh, and, from the results presented here, it would appear that they will make a significant contribution in such an analysis.

We were again faced with the problem of evaluating the goodness of any fits obtained and we set about this first by

choosing as the best fit for each channel that fit which had the largest maximum value of $\ell n\, L$. For the best fit in each channel, the coefficients $A_n(\omega)$ and $B_n(\omega)$ in equations (4.3) were calculated from the fitted parameters and compared with the A and B coefficients obtained in fits to discrete energy regions in Section III.3. In this way it could immediately be seen if the fitted parameters gave a reasonable description of the energy dependence of these coefficients and thus of the data. All the fitting in this experiment employed the CERN minimization program MINUIT[23], maximum likelihood values being obtained by minimizing $-\ell n\, L$.

In discussing our fitted partial wave amplitudes we shall adopt the spectroscopic notation, describing each wave by S, P, D or F representing orbital angular momentum values $L = 0, 1, 2$ or 3, followed by I, the isospin, and $2J$, where J is the total angular momentum. Thus the D03 wave has $L = 2$, $I = 0$ and $J = \frac{3}{2}$. Since the parity $P = -(-1)^L$, any resonances in this wave would have $J^P = \frac{3}{2}^-$.

We shall first describe the results for the $\Sigma^0\pi^0$ channel as this is the more interesting of the two. The consensus of opinion in previous analyses is that, up to 1750 MeV, we need only consider S01, P01, P03, D03, D05 and F05 waves and that backgrounds are required only in the first three waves. As the well-established resonances at 1830 MeV in D05 and 1819 MeV in F05 are outside our energy

range, the parameters of these have been taken as fixed in the analysis at estimated world-average values[1]. This leaves quite well-established resonances at 1670 MeV in S01 and 1690 MeV in D03 together with a proposed resonance in P01 at around 1700-1800 MeV, all of which were taken as optional and variable in the fits. Where a resonance occurred in a wave with no background, the phase angle ϕ in the resonant amplitude was fixed to be either 0 or π radians in accordance with the Levi-Setti sign convention[1] when this was defined for the resonance. In the presence of a background, however, this phase may alter but we found that, if we allowed the phase of, for example, the S01 resonance to remain a free parameter in the fit, the resulting fit was very poor with badly distorted resonance parameters. While not fully understanding the reason for this instability, it was felt better similarly to constrain the phase of resonances with backgrounds to be 0 or π radians in which case good fits were obtained. Starting values for resonance parameters were taken from the Particle Data Group Tables[1] and all background parameters were started from zero.

Table 14 shows the resonance parameters and Table 15 the background parameters for the best fit to our data in the $\Sigma^0\pi^0$ channel over the energy range 1570 MeV to 1750 MeV. Parameters marked with an asterisk were not varied in this fit. The errors quoted are purely statistical from the fit and do not include the systematic errors in the detection efficiency function, in the normalization factor and those arising from the particular parameterization

Wave	ω_R (MeV)	Γ_o (MeV)	$\sqrt{X_e X_r}$	ϕ (radians)
S01	1669 ± 3	30 ± 9	0.194 ± 0.002	π*
P01	1764 ± 1	68 ± 2	0.425 ± 0.009	0
D03	1703 ± 2	99 ± 2	0.268 ± 0.013	π*
D05	1830*	90*	0.170*	π*
F05	1819*	80*	0.260*	π*

TABLE 14

Resonance parameters for the best fit in the $\Sigma^o\pi^o$ channel.

Wave	A	B(GeV/c^{-1})	C(GeV/c^{-2})	D	E(GeV/c^{-1})	F(GeV/c^{-2})
S01	-.315 ± .008	.046 ± .009	.129 ± .015	-.392 ± .026	.293 ± .019	.167 ± .026
P01	.094 ± .010	.017 ± .009	-.127 ± .029	-.145 ± .002	-.131 ± .005	-.168 ± .005
P03	.215 ± .017	-.187 ± .010	.059 ± .021	.111 ± .005	-.019 ± .018	-.034 ± .007

TABLE 15

Background parameters for the best fit in the $\Sigma^o\pi^o$ channel.

adopted. Realistic errors would therefore probably be several times larger than the quoted values.

Figure 23 illustrates the behaviour of the partial wave amplitudes in the best fit. The position of resonance is marked for each amplitude which resonates within our energy range. In Figure 24 we show by continuous curves the coefficients $A_n(\omega)$ and $B_n(\omega)$ calculated from the best fitted parameters together with the discrete energy-averaged coefficients obtained in Section III.3. The good agreement indicates that the best $\Sigma^0\pi^0$ fit gives an adequate representation of the data. In particular, a comparison with Figure 22 shows that, while our own results are in good internal agreement, they are in consistent disagreement with the results of the CHS hydrogen experiment[2]. The culmination of this disagreement is seen in Table 14 where our earlier suppositions concerning the branching ratio of the $\Lambda(1670)$ resonance into $\Sigma\pi$ are to a large extent justified. We find this S01 resonance more weakly coupled to $\Sigma\pi$ than previous analyses of hydrogen experiments indicate with a branching ratio of 0.19 as opposed to about 0.3. This is in agreement with the unpublished results of a K^-p spark chamber experiment to study the $\Lambda^0\pi^0$ and $\Sigma^0\pi^0$ final states which were mentioned in a rapporteur's talk by Dalitz at the Amsterdam Conference[5e]. It would be interesting to see the results of a multi-channel analysis incorporating our data for the $\Sigma^0\pi^0$ channel and also the effect of a lower $\Sigma\pi$

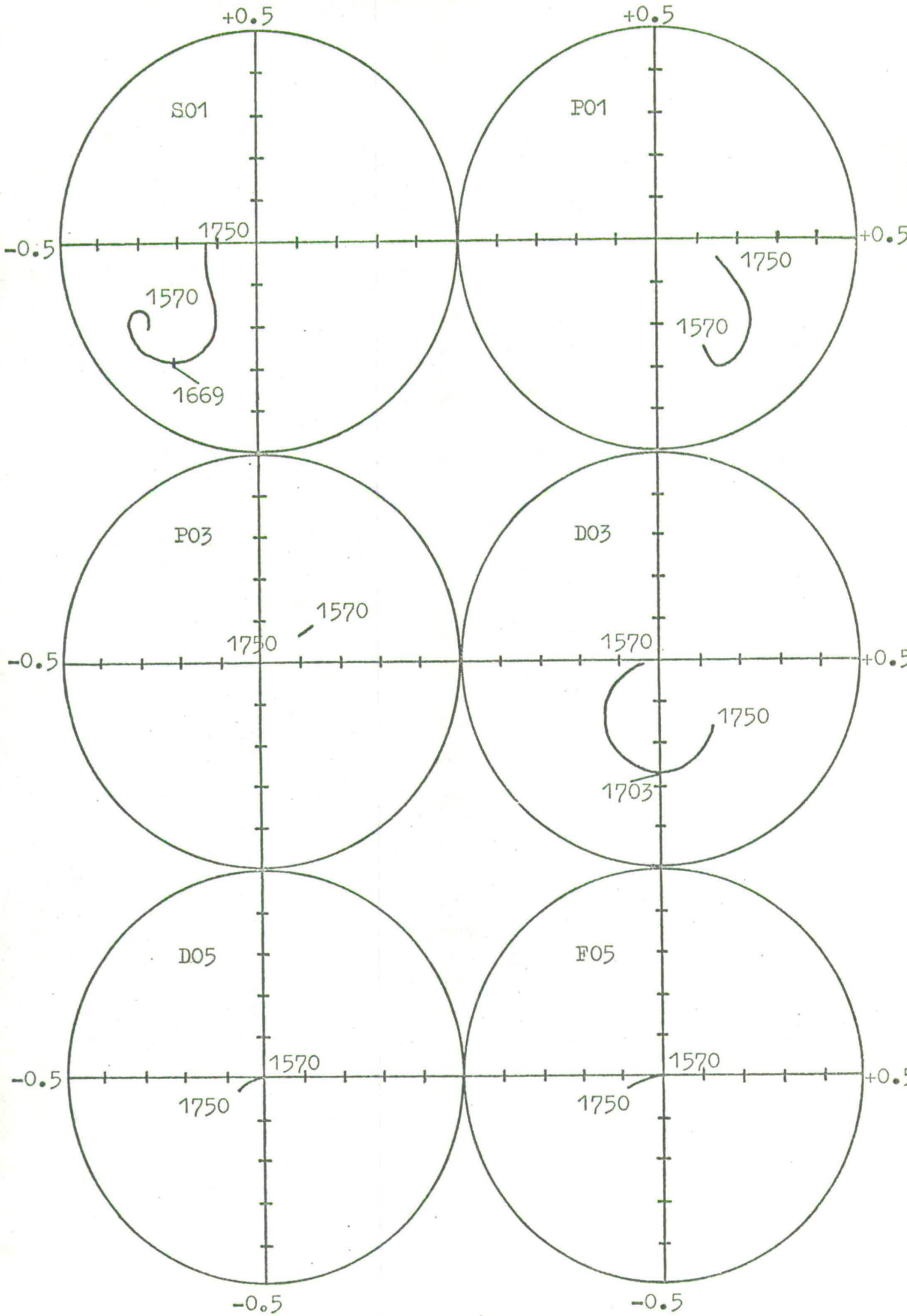

Fig. 23. Partial wave amplitudes for the $\Sigma^0\pi^0$ channel.

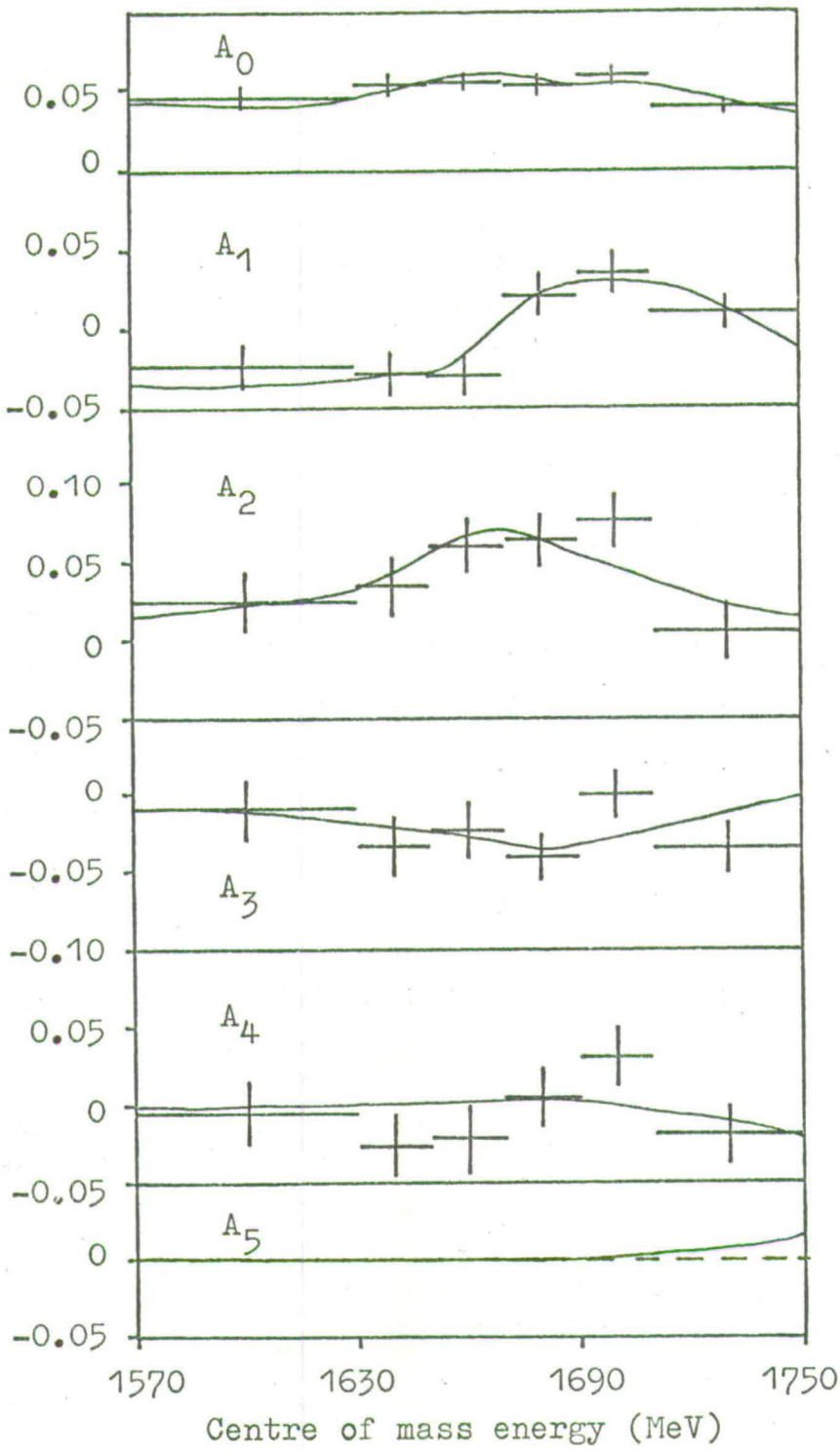

Fig. 24. A and B coefficients from the partial wave analysis of the $\Sigma^0\pi^0$ channel.

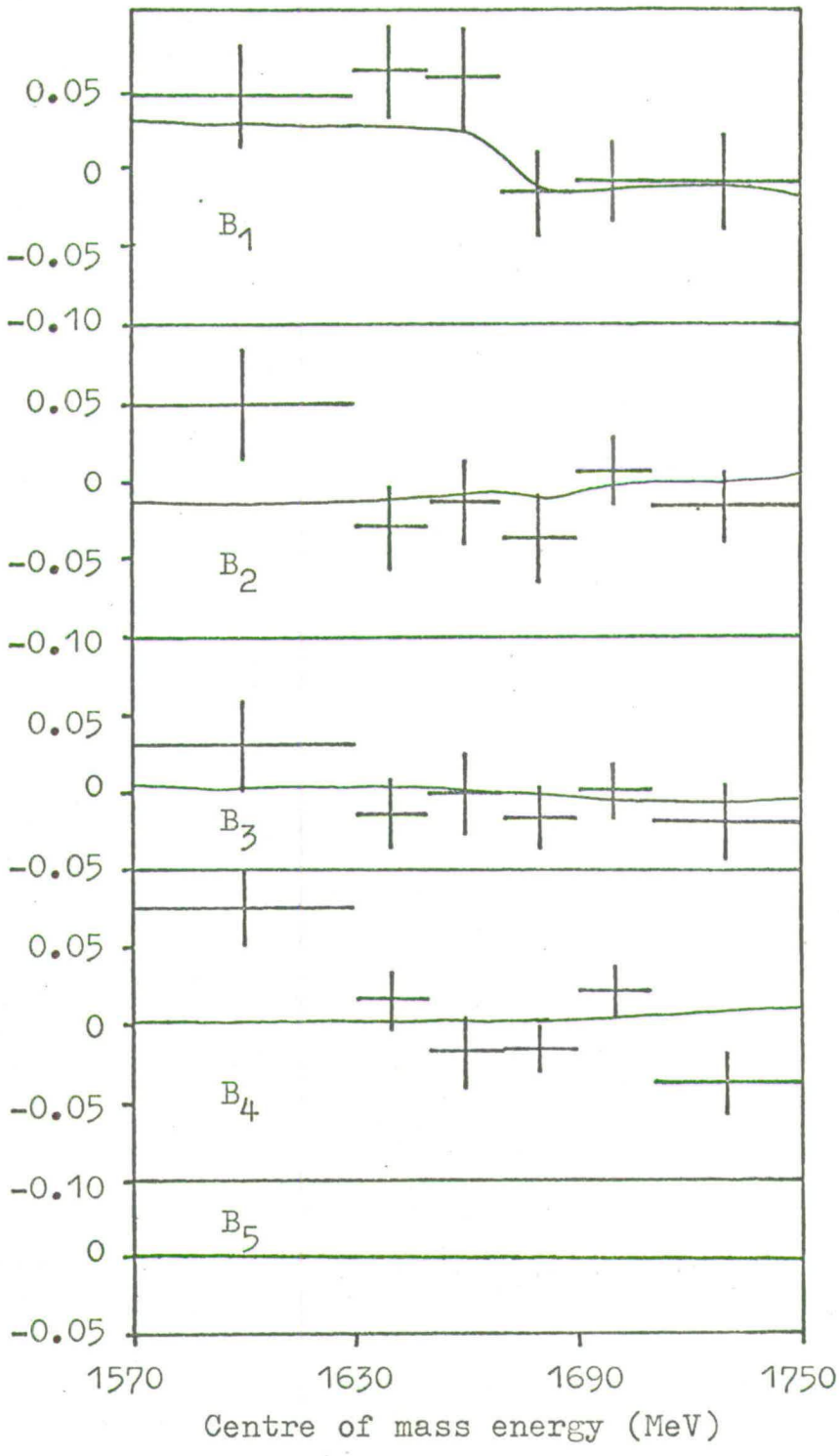

Fig. 24. A and B coefficients from the partial wave analysis of the $\Sigma^0\pi^0$ channel.

branching ratio for the $\Lambda(1670)$ on the mixing angle required to obtain satisfactory SU(3) fits to the $\frac{1}{2}^-$ nonet as the amount of mixing still seems to be uncertain[24,25]. Our parameters for the $\Lambda(1690)$ resonance in D03 are in generally good agreement with previous values although the width is larger. In spite of the fact that the error on Γ_o is very small, it became apparent in the course of the analysis that the fits were not particularly sensitive to variations in Γ_o of the order of 20 MeV although ω_R and $\sqrt{X_e X_r}$ were much better defined. This discrepancy is therefore not considered to be significant. We also require a P01 resonance at 1764 MeV with a strong coupling to $\Sigma\pi$ and a phase angle of 0 radians. Our parameters for this resonance, with the exception of the branching ratio, are similar to those of the P01 resonance found in previous analyses and confirm the presence of resonant structure in this wave.

Our results, obtained in the first single-channel partial wave analysis of the reaction $K^-p \rightarrow \Sigma^o\pi^o$, therefore largely confirm the findings of hydrogen bubble chamber experiments, while indicating that there may be inaccuracies in these experiments which have led to small errors in the determination of resonance parameters.

Next we present the results of our partial wave analysis of the $\Lambda^o\pi^o$ channel. Here again it was sufficient to consider only S11, P11, P13, D13, D15 and F15 waves with backgrounds in the first four waves. The parameters of the

well-established resonances at 1766 MeV in D15 and at 1910 MeV in F15 were fixed throughout the analysis and the resonant structure in the lower partial waves was varied along with the background. Previous partial wave analyses have indicated an established resonance at 1660 MeV in D13, a likely resonance at about 1750 MeV in S11 and possible candidates around 1620 MeV in S11 and P11. The phases of resonances were fixed in accordance with the Levi-Setti convention[1] or allowed to take only the values 0 or π radians. Starting values for resonance parameters were again taken from the Particle Data Group Tables[1] and background parameters started from zero.

The best fit obtained to our data in the $\Lambda^0\pi^0$ channel in the range 1570 MeV to 1750 MeV gave the resonance parameters in Table 16 and the background parameters in Table 17.

Wave	ω_R(MeV)	Γ_o(MeV)	$\sqrt{X_e X_r}$	ϕ (radians)
S11	1600 ± 1	14 ± 1	0.142 ± 0.001	0
S11	1694 ± 2	26 ± 4	0.167 ± 0.016	π *
P11	1685 ± 1	28 ± 1	0.101 ± 0.001	0
D13	1656 ± 3	43 ± 1	0.106 ± 0.001	0 *
D15	1766 *	112 *	0.240 *	π *
F15	1910 *	80 *	0.090 *	π *

TABLE 16

Resonance parameters for the best fit in the $\Lambda^0\pi^0$ channel.

Wave	A	B(GeV/c^{-1})	C(GeV/c^{-2})	D	E(GeV/c^{-1})	F(GeV/c^{-2})
S11	$-.281 \pm .008$	$.074 \pm .005$	$-.017 \pm .006$	$.230 \pm .006$	$-.276 \pm .007$	$-.125 \pm .013$
P11	$-.162 \pm .006$	$.037 \pm .004$	$-.010 \pm .005$	$.063 \pm .008$	$-.073 \pm .005$	$-.178 \pm .005$
P13	$-.039 \pm .005$	$.065 \pm .003$	$-.027 \pm .005$	$-.009 \pm .002$	$.190 \pm .008$	$-.077 \pm .017$
D13	$.037 \pm .002$	$-.114 \pm .005$	$.012 \pm .012$	$.052 \pm .007$	$-.159 \pm .010$	$.108 \pm .008$

TABLE 17

Background parameters for the best fit in the $\Lambda^{o}\pi^{o}$ channel.

Parameters marked with an asterisk were held constant in this fit. As before, these errors are likely to be considerably underestimated.

The partial wave amplitudes from the best $\Lambda^{o}\pi^{o}$ fit are shown in Figure 25 with the resonance positions marked if these occur within our energy range, while Figure 26 displays as continuous curves the coefficients $A_n(\omega)$ and $B_n(\omega)$ calculated from the best fitted parameters together with the energy-averaged coefficients obtained in Section III.3. The agreement here is reasonably good but with some discrepancy above about 1710 MeV. Comparing these results with Figure 21, it would appear that the energy dependence of the coefficients $A_n(\omega)$ and $B_n(\omega)$ from our partial wave analysis agrees even better with the coefficients obtained in hydrogen experiments[2,10] than it does with our own energy-averaged A and B coefficients. This is not surprising as these energy-averaged coefficients cannot be expected to follow the detailed energy dependence inherent in the data. Some coefficients presented graphically only by the CHS collaboration[26] show considerable fluctuations between 1710 MeV and 1750 MeV indicating that our energy-averaged coefficients may be unreliable in this region and perhaps explaining the discrepancy noted above. With this minor reservation, our best $\Lambda^{o}\pi^{o}$ fit appears to give an acceptable energy-dependent description of the data and good agreement with hydrogen experiments. Our fitted parameters for the D13 resonance at 1656 MeV agree well with previous

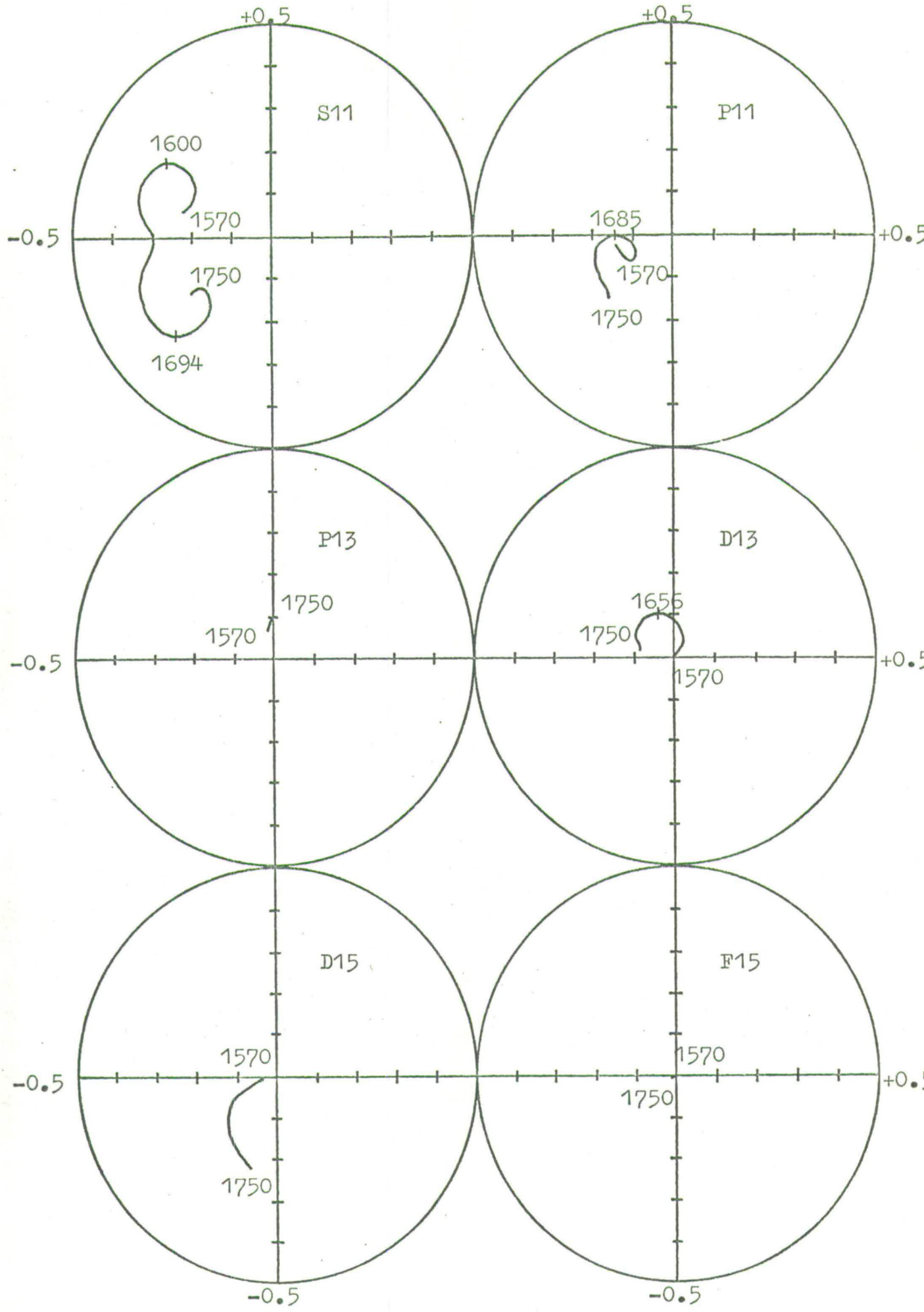

Fig. 25. Partial wave amplitudes for the $\Lambda^{o}\pi^{o}$ channel.

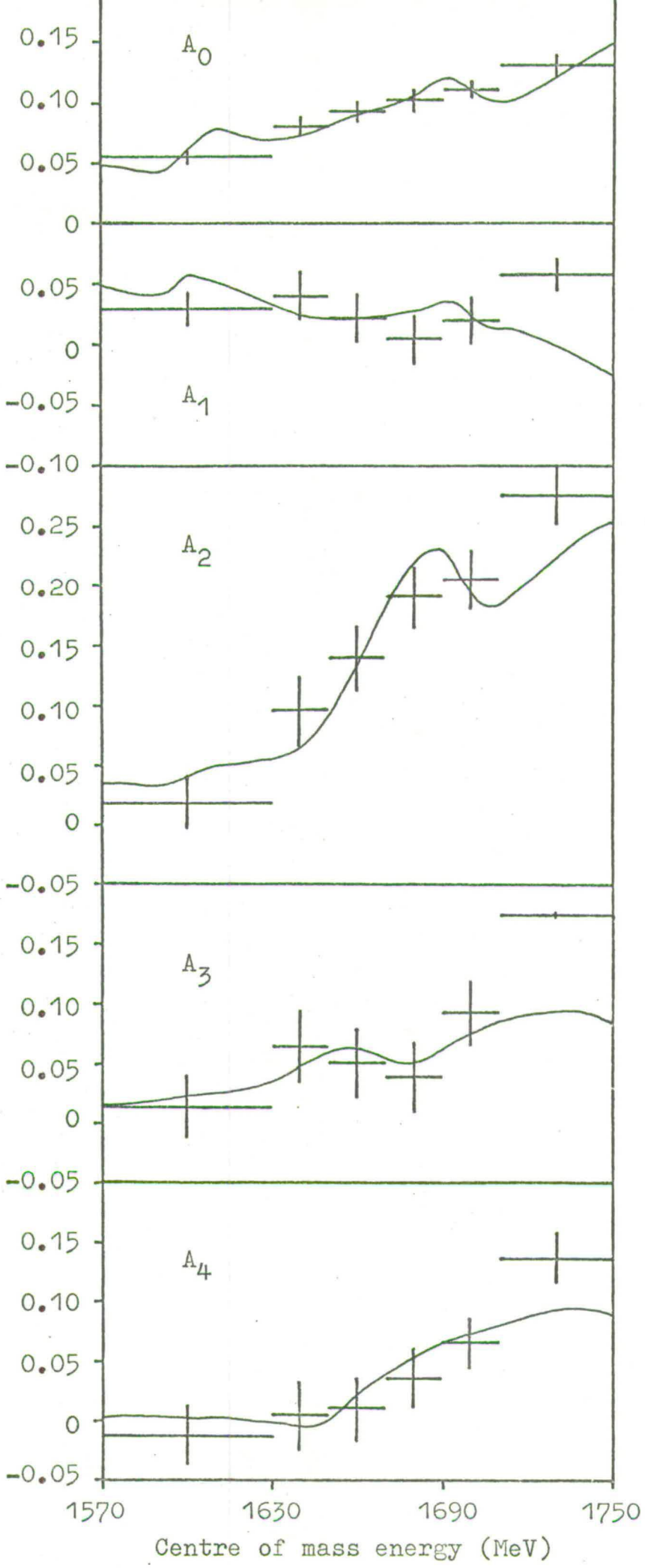

Fig. 26. A and B coefficients from the partial wave analysis of the $\Lambda^{o}\pi^{o}$ channel.

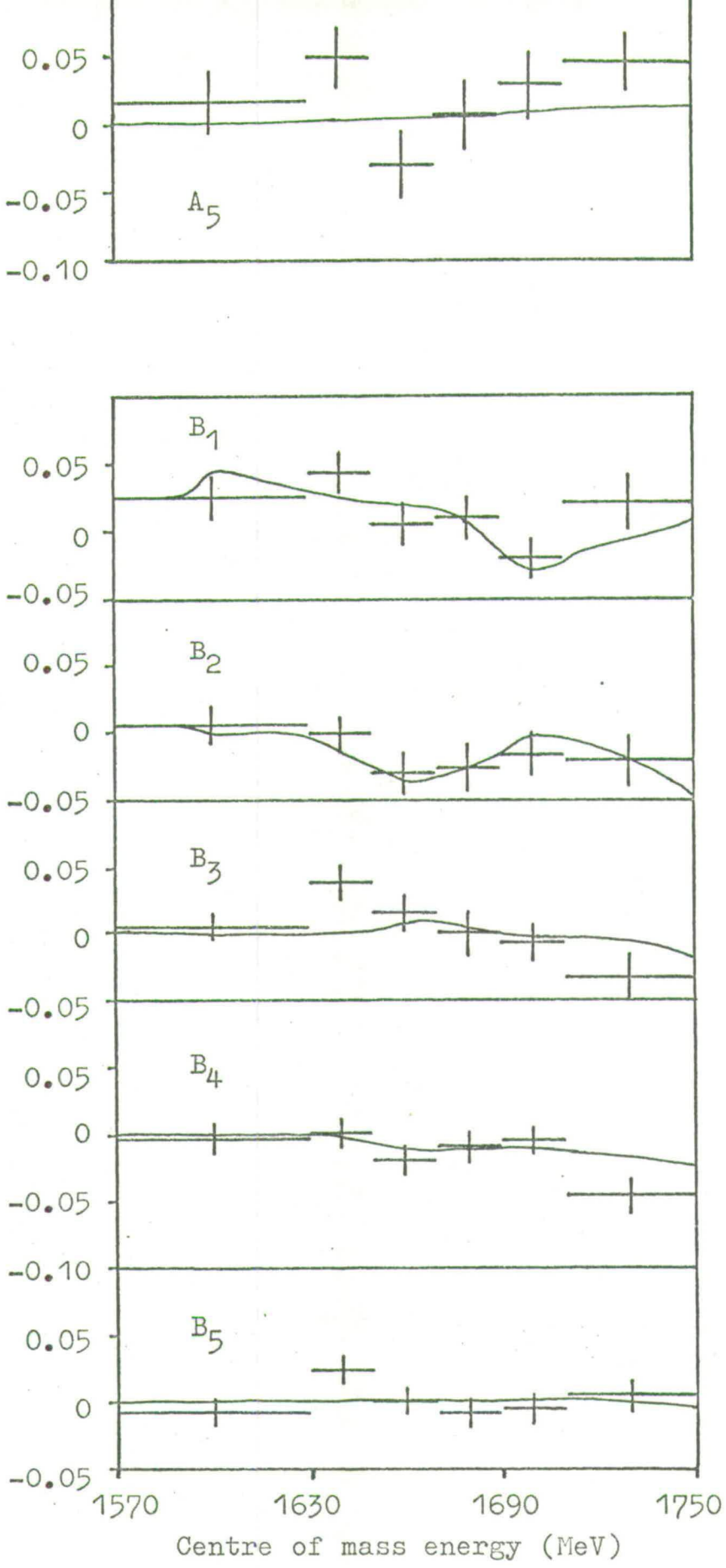

Fig. 26. A and B coefficients from the partial wave analysis of the $\Lambda^{o}\pi^{o}$ channel.

values, while we find the S11 resonance at 1694 MeV to have a lower energy and smaller width than before. There is still considerable uncertainty about this resonance and a recent analysis by Van Horn[18e] finds a similar energy of 1697 MeV. We get a significantly better fit by including additional S11 and P11 resonances which always adopt parameter values similar to those in Table 16 however they are initialized. The energies and branching ratios of these two resonances are in reasonable agreement with previous results which are themselves very uncertain, but we find considerably smaller widths. As mentioned before, however, our fits seem to be somewhat insensitive to the widths of the fitted resonances and so the values quoted should be regarded with suspicion.

Thus, while we find differences of detail, we broadly confirm the resonant structure observed in formation experiments in the $\Lambda^{o}\pi^{o}$ final state.

CHAPTER IV

CONCLUSION

The design objective of this experiment, to study the neutral final states produced in K^-p interactions between 1570 MeV and 1750 MeV and to investigate the formation of baryon resonances in the $\Lambda^0\pi^0$ and $\Sigma^0\pi^0$ channels, has been successfully met even though only three-quarters of the data are so far available. Many problems associated with heavy liquid experiments have been encountered and overcome and our results indicate that this is a viable method of studying interactions involving π^0 production. An ideal combination for such experiments would be a track-sensitive hydrogen target giving background-free interactions surrounded by heavy liquid to provide a γ-detection capability.

While we find good agreement with hydrogen bubble chamber experiments in the $\Lambda^0\pi^0$ channel, our results for $\Sigma^0\pi^0$, $\Lambda^0\pi^0\pi^0$ and $\Sigma^0\pi^0\pi^0$ indicate that previous analyses have wrongly apportioned events between these channels enhancing the $\Sigma^0\pi^0$ cross-section at the expense of the three-body final states. Although the quantity of our data is not large, the quality has been shown to be good enough to allow single-channel energy-dependent partial wave analyses of the $\Lambda^0\pi^0$ and $\Sigma^0\pi^0$ final states using a maximum likelihood fitting technique specially developed for the purpose. This is the first such analysis to study the $\Sigma^0\pi^0$ channel on its own.

We have not attempted an exhaustive search for new resonances but have tried to obtain a satisfactory description of the data in terms of resonances already established or proposed. This was done partly to determine the quality of our data and partly to compare our results with those of hydrogen bubble chamber experiments. In general we find good agreement with previous analyses for the parameters of established resonances with one significant exception together with further evidence for the existence of proposed resonances in our energy range. This exception is the $\Sigma\pi$ branching ratio of the $\Lambda(1670)$ resonance which partial wave analyses incorporating hydrogen bubble chamber results for the $\Sigma^{\circ}\pi^{\circ}$ channel have indicated is about 0.3. Our more precise measurements for this channel lead to a value of 0.19.

However we make no claims of uniqueness for the solutions obtained, only that they give acceptable fits to our data with reasonable parameter values. The full potential of our data will only be realised when they are incorporated in a complete multi-channel analysis of the $\bar{K}N$ system and there are plans to achieve this in the future at Edinburgh.

APPENDIX

Estimation of $\langle n \rangle$, the average number of acceptable beam tracks per photograph.

Suppose that $N_p(n)$ is the distribution of photographs as a function of n, the number of acceptable beam tracks in a photograph. As photographs were only scanned if they had between 1 and 12 acceptable beam tracks, $\langle n \rangle$ is given by

$$\langle n \rangle = \frac{\sum_{n=1}^{12} n\, N_p(n)}{\sum_{n=1}^{12} N_p(n)}$$

Now, if p is the probability that a beam track gives an event, $N_e(n)$, the distribution of number of events as a function of the number of acceptable beam tracks in a photograph, is given by

$$N_e(n) = p\, n\, N_p(n) .$$

Thus we can get an expression for $\langle n \rangle$ in terms of $N_e(n)$, which can be found from the beam count in photographs with one or more events, namely

$$\langle n \rangle = \frac{\sum_{n=1}^{12} N_e(n)}{\sum_{n=1}^{12} \frac{N_e(n)}{n}} .$$

The error in $\langle n \rangle$ is calculated as

$$(\Delta\langle n\rangle)^2 = \sum_{n=1}^{12}\left[\frac{\partial\langle n\rangle}{\partial N_e(n)} \cdot \Delta N_e(n)\right]^2$$

$$= \sum_{n=1}^{12}\left[\left\{\frac{1}{\sum_{n=1}^{12}\frac{N_e(n)}{n}} - \frac{\langle n\rangle}{\sum_{n=1}^{12}\frac{N_e(n)}{n}}\cdot\frac{1}{n}\right\}\sqrt{N_e(n)}\right]^2$$

$$= \left(\frac{\langle n\rangle}{\sum_{n=1}^{12} N_e(n)}\right)^2 \sum_{n=1}^{12}\left[\left(1 - \frac{\langle n\rangle}{n}\right)^2 N_e(n)\right]$$

$$\therefore \quad \frac{\Delta\langle n\rangle}{\langle n\rangle} = \frac{1}{\sum_{n=1}^{12} N_e(n)} \sqrt{\sum_{n=1}^{12}\left[\left(1 - \frac{\langle n\rangle}{n}\right)^2 N_e(n)\right]} \; .$$

REFERENCES

(1) Particle Data Group, Review of Particle Properties, Rev. Mod. Phys. 45, No. 2, Part II (1973).

(2)(a) R. Armenteros et al., Nucl. Phys. B8, 233 (1968).

(b) R. Armenteros et al., Nucl. Phys. B21, 15 (1970).

(3) P. Bastien and P. Berge, Phys. Rev. Lett. 10, 188 (1963).

(4) L. Bertanza et al., Phys. Rev. 177, 2036 (1969).

(5)(a) R.D. Tripp, Proceedings of the 14th International Conference on High Energy Physics, 173, ed. Prentki and Steinberger (Vienna, 1968).

(b) R. Levi-Setti, Proceedings of the Lund International Conference on Elementary Particles, 339, ed. von Dardel (Lund, 1969).

(c) R.D. Tripp, 3rd Topical Conference on Particle Physics, Lawrence Radiation Laboratory Report No. UCRL-19361 (1969).

(d) N.P. Samios, 15th International Conference on High Energy Physics, Brookhaven National Laboratory Report No. BNL-15284 (1970).

(e) R.H. Dalitz, Proceedings of the Amsterdam International Conference on Elementary Particles, 201, ed. Tenner and Veltman (Amsterdam, 1971).

(f) T.A. Lasinski, Proceedings of the 16th International Conference on High Energy Physics, Vol. I, 56, ed. Jackson and Roberts (Batavia, 1972).

(6) R.Y.L. Chu et al., Nucl. Phys. to be published.

(7) S. Derenzo and R. Hildebrand, Nucl. Instr. and Meth. 69, 287 (1969).

(8) T. Beggs, Ph.D. Thesis, Edinburgh (1973).

(9) A. Ferrer-Soria, Thèse 3ème Cycle, Orsay (1971).

(10) A.J. Van Horn et al., Phys. Rev. D6, 1275 (1972).

(11) T. Dombeck et al., Phys. Rev. D7, 1331 (1973).

REFERENCES (CONTD.)

(12) R.Y.L. Chu et al., Paper to be presented at the 2nd Aix-en-Provence International Conference on Elementary Particles (1973).

(13)(a) R. Armenteros et al., Nucl. Phys. B8, 223 (1968).

(b) R. Armenteros et al., Nucl. Phys. B14, 91 (1969).

(14) R. Armenteros et al., Proceedings of the Duke Conference on Hyperon Resonances, 123, ed. E. Fowler (Durham, 1970).

(15) R. Gatto, Phys. Rev. 109, 610 (1958).

(16) R.D. Tripp, Proceedings of the International School of Physics, "Enrico Fermi", Varenna, Italy, Course 33 (Academic Press, 1966).

(17) W. Langbein and F. Wagner, Nucl. Phys. B47, 477 (1972)

(18)(a) R. Armenteros et al., Nucl. Phys. B10, 459 (1969).

(b) R. Armenteros et al., Phys. Lett. 28B, 521 (1969).

(c) W.M. Smart, Phys. Rev. 169, 1330 (1968).

(d) A. Barbaro-Galtieri, Proceedings of the Duke Conference on Hyperon Resonances, 173, ed. E. Fowler (Durham, 1970).

(e) A.J. Van Horn, Ph.D. Thesis, Lawrence Berkeley Laboratory Report No. LBL-1370 (1972).

(f) D. Berley et al., Phys. Lett. 30B, 430 (1969).

(19) J.K. Kim, Phys. Rev. Lett. 27, 356 (1971).

(20) A.T. Lea et al., Nucl. Phys. B56, 77 (1973).

(21) F. von Hippel and C. Quigg, Phys. Rev. D5, 624 (1972).

(22) A. Barbaro-Galtieri, Advances in Particle Physics, Vol. II, ed. Cool and Marshak (Interscience Publishers, 1968).

(23) F. James and M. Roos, Minuit, CERN Computer Program Library, D506, D516 (1972).

(24) D.E. Plane et al., Nucl. Phys. B22, 93 (1970).

(25) A. Barbaro-Galtieri, Proceedings of the 16th International Conference on High Energy Physics, Vol. 159, ed. Jackson and Roberts (Batavia, 1972).

(26) R. Armenteros et al., Nucl. Phys. B8, 183 (1968).